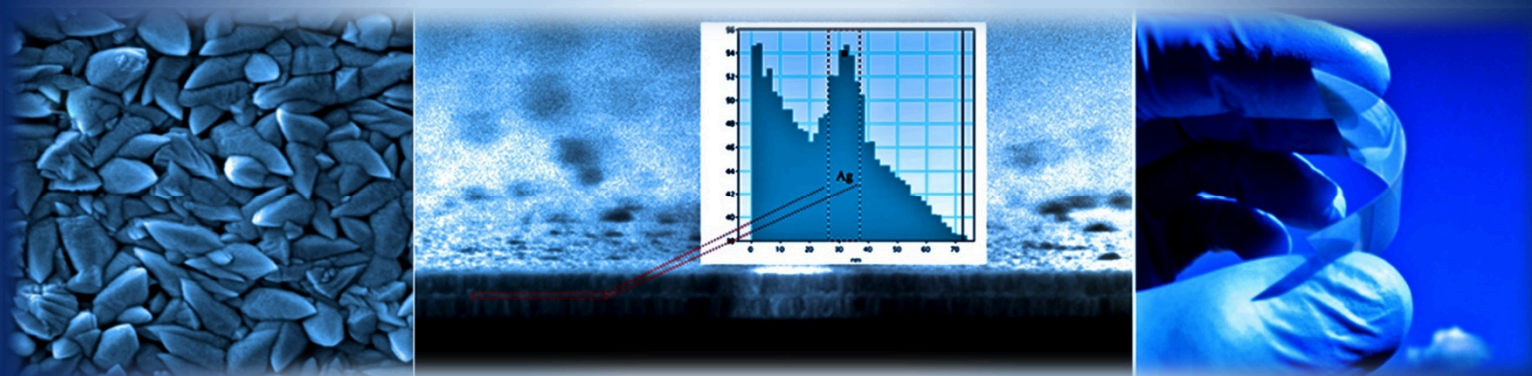


Università degli Studi di Catania

Dottorato di ricerca in scienza e tecnologia dei materiali – XXVII Ciclo

Stefano Boscarino



*Ultra-thin Transparent Electrodes for
Energy Applications*

Tutor: Prof. A. Terrasi

Supervisor: Dr. I. Crupi

Coordinatore: Prof. M. Grimaldi



UNIVERSITÀ DEGLI STUDI DI CATANIA

Dottorato di Ricerca in Scienza e Tecnologia dei Materiali - XXVII ciclo

Stefano Boscarino

Ultra-thin Transparent Electrodes for Energy Applications

Tutor: Prof. A. Terrasi

Supervisor: Dr. I. Crupi

Coordinatore: Prof.ssa M.G. Grimaldi

Tesi per il conseguimento del titolo

To my two awesome families



COVER

CENTER:

Cross section scanning electron microscopy image of an AZO/Ag/AZO multilayer 100nm thick. The inset is the output of the software used to estimate the thickness of the Ag intralayer (10nm).

LEFT:

Plane view scanning electron microscopy image of an AZO surface layer deposited by RF magnetron sputtering

RIGHT:

Picture of a flexible, transparent and conductive AZO thin-film deposited on plastic substrate.

Ultra-thin transparent electrodes for energy applications

Stefano Boscarino

Ph.D. Thesis, University of Catania

Printed in Catania, December 2014

Gli spiriti liberi vivono di un moderato scetticismo, amano la vita, non disprezzano la morte, seguono la ragione, non si lasciano ammaliare dagli idoli della razza, della nazione dell'autorità, del potere o profitto, dell'appartenenza ad una chiesa, ad un partito o ad una accademia, coltivano le virtù etiche della temperanza, della tolleranza, della lealtà e della solidarietà tra gli uomini, rispettano la natura senza idolatrarla, praticano la cultura del dare di contro a quella dell'avere, della collaborazione di contro a quella della competizione e della sopraffazione dell'altro, lottano per le cose giuste, cercano il vero, sono innamorati del bello, nutrono il sentimento di una sana speranza senza il mito del progresso lineare, continuo ed infinito

G. Boscarino

Contents

Motivation	i
Outline of the thesis.....	ii
Chapter 1	
Transparent conducting materials.....	1
1.1 Brief history of TCOs.....	2
1.2 Basic material physics of TCOs	5
1.2.1 Band structures.....	6
1.2.2 Electrical transport in n-type TCOs	8
1.2.3 Optical properties	14
1.3 Development of alternative transparent electrodes	19
1.3.1 Multilayered structures	19
1.3.2 Emerging nanomaterials.....	21
1.4 Industrial applications	27
1.4.1 Solar energy	28
1.4.2 Towards transparent electronics.....	31
References	34

Chapter 2

Al-doped ZnO	38
2.1 AZO deposited by RF magnetron sputtering.....	39
2.2 Material Characterization	44
2.2.1 Influence of RF power.....	44
2.2.2 Effect of post deposition thermal treatment.....	57
2.2.3 Influence of the substrate temperature	61
2.3 Ion Implantation	67
2.3.1 O ⁺ ion irradiation of AZO.....	68
2.3.2 Ar ⁺ ion implantation of AZO on polymer substrate.....	78
2.4 Conclusions	81
References	84

Chapter 3

TCO/Ag/TCO ultra-thin multilayers	86
3.1 Materials selection	87
3.1.1 Silver as intralayer.....	87
3.1.2 Which TCO?.....	94
3.2 High-performance AZO/Ag/AZO transparent electrode	99
3.2.1 Appropriate Ag thickness.....	100
3.2.2 Temperature effects	107

3.2.3	Thermal stability	108
3.3	TCO/Ag/TCO	111
3.3.1	ITO and AZO: a comparative investigation	112
3.4	Conclusions	119
	References	121

Chapter 4

	Laser scribing processes on AZO/Ag/AZO	124
4.1	Laser application in thin film solar cells	125
4.2	P1 on AZO/Ag/AZO	128
4.2.1	Laser-induced structural modifications	130
4.2.2	Electrical insulation	133
4.2.3	Heat transfer: model and analysis	135
4.3	Conclusions	140
	References	142

	Appendix: Synthesis and characterization details	143
--	---	------------

	Curriculum Vitae	175
--	-------------------------------	------------

	List of Publications	176
--	-----------------------------------	------------

Motivation

Due to the unique feature of being contemporarily optically transparent and electrically conducting, Transparent Conductive Oxides (TCOs) play a fundamental role in many technologies: communications, information, energy, buildings [1-3]. Up to now, the most diffused material in the TCO's family was indium tin oxide (ITO), especially for large-area applications such as flat panel displays. Recently, the increasing expansion of the display market and, even more, of photovoltaics, are endangered by the scarcity and rising price of indium. This is one of the reasons and a strong motivation for searching alternative transparent electrodes, not necessarily oxides, to replace ITO. Moreover, in order to meet the expectations for the growing demand and lower production costs for photovoltaic and electronic applications, new TCOs, or equivalent materials, must be abundant, not expensive and very thin, so to be suitable for flexible electronics [1-3].

Among new transparent electrodes candidates, Aluminium-doped zinc oxide (AZO) films and very thin multilayers of AZO/Ag/AZO have emerged as a very promising alternative [2, 3]. In particular, AZO films are Indium-free and show electro-optical properties comparable to ITO films of the same thickness (typically 700-900 nm for industrial applications), especially after thermal annealing at 250 °C. On the other hand, AZO/Ag/AZO multilayer structures, 10 times thinner than ITO or AZO single layers, show very high transparency and low resistivity even at room temperature. Replacing thick TCO layers with thin TCO/Ag/TCO multilayers would produce great benefits in terms of material consumption, cost, toxicity and flexibility (a mandatory point for the development of the electronics on plastic). In this context, it is important the study and understanding of the fundamental properties of these materials, the process conditions and post fabrication treatments to optimize their application to different fields. Transparent conductive materials are known

since about 100 years and represent one of the strategic topics for the actual industrial research, but still many fundamental properties and mechanisms need to be clarified and explained.

Outline of the thesis

Aim of this work is the fabrication, processing and characterization of ultra-thin AZO and TCO/Ag/TCO transparent electrodes. The study focused on the optimization of structural, optical and electrical properties for application in photovoltaics. The thesis is organized as follows.

Chapter 1 introduces Transparent Conductive Oxides (TCOs) and covers the conventional materials history, properties and market. In particular, it gives a detailed description of the energy band structure and doping processes. After the state of the art of standard and industrial TOCs, new materials are also discussed, highlighting limits and potentialities for application in solar energy and other technological contexts.

Chapter 2 is devoted to the processing and characterization of AZO films grown by RF magnetron sputtering. It starts with a comprehensive and detailed study about sputtered thick AZO films on glass substrates, focusing on the influence of sputtering process parameters, i.e. power, temperature substrate, and thermal treatment (during or after the deposition) on the film properties. A strong correlation between the deposition conditions and AZO film properties was observed: a particular set of parameters gives the lowest resistivity, the highest transparency and crystalline quality. Moreover, a thermal treatment after (200 °C) or during (up to 300°C) the deposition leads to a slight improvement and worsening of the electro-optical properties of AZO, respectively. After the work on thick AZO, we report the modification of optical, electrical and structural properties of very thin films (60 nm) upon ion irradiation with different ion type (O^+ or Ar^+ ions) and energy (30 and 350 keV) at different ion doses (3×10^{15} , 1×10^{16} ,

3×10^{16} ions/cm²), before and after thermal treatments up to 400°C. The experimental data highlight the structural improvement due to ion irradiation, the strong decreases of the electrical resistivity for O⁺ beams passing through or for Ar⁺ implanted within the AZO films. Only when O⁺ was implanted within the AZO, the structural improvements were accompanied by a huge increasing of the electrical resistivity, demonstrating the main role of oxygen in the activation and deactivation of the doping. Most of observed effects on the structural and electrical behaviors were very similar to those obtained after a thermal treatment up to 400 °C, without ion irradiation, so that we propose the ion beam processing as a good alternative to thermal treatments for plastic substrates.

Chapter 3 treats of very thin TCO/Ag/TCO multilayer structures grown by RF magnetron sputtering. Synthesis and properties of AZO/Ag/AZO multilayers as a function of Ag film thickness, with a fixed AZO thickness (~20 nm), are investigated. The best structure was shown to have a 9.5 nm Ag film as mid-layer, while thermal stability analysis demonstrated an excellent behavior of the AZO film as a barrier to Ag diffusion. Then, we studied multilayers with fixed Ag thickness, but different combinations of AZO and ITO as top and bottom TCO layers. The multilayered structure has shown better performances when the top and bottom TCOs are of different type, with the possibility of tuning the reflectivity in a proper range of wavelengths.

Chapter 4 describes the compatibility of the AZO/Ag/AZO multilayers with one of the most important steps for the implementation in thin film photovoltaic technology: laser scribing. A crucial aspect in the fabrication of solar panels is the patterning and electrical insulation of solar cells. Laser scribing of thick TCO films, thin amorphous Si layers and metallization layers are standard processes in the photovoltaics industry. AZO/Ag/AZO multilayers must be able to guarantee the same level of reliability under laser scribing processes. In our study, we used a single nanosecond laser pulse to irradiate ultra-thin multilayers deposited on glass. We demonstrated that given a pulse energy as low as 1.15 J/cm², the electrical

resistance in the insulated region of AZO/Ag/AZO is enhanced by 8 orders of magnitude compared to thick single AZO, currently used in thin film solar cell. In particular, the thermal behavior, simulated using a finite element approach, shows that the silver intralayer plays two key roles on the scribing process, by increasing the maximum temperature reached in the structure and fastening the cool down process.

Finally, we decided to describe all growth, processing, analysis techniques and equipment in the appendix at the end of the thesis.

References

- [1] D.S. Ginley, H. Hosono, D.C. Paine, Handbook of transparent Conductors (Springer-Verlag, 2010).
- [2] K. Ellmer, Nature Photonics **6**, 809-817 (2012).
- [3] C. Guillén, J. Herrero, Thin Solid Films **520**, 1-17 (2011).

Chapter 1

Transparent conducting materials

This chapter presents an overview of the literature on transparent conductive materials. These electrodes, exhibiting both transparency and electronic conductivity simultaneously, found wide spread use in portable devices, flat-screen displays, low-emittance windows, flexible electronics and solar cells.

This chapter begins with a brief introduction on the history and the market of transparent electrodes, followed by a description of the structural, optical and electrical properties of the most commonly transparent conductive oxides (TCO) based on binary compound, such as ZnO, In_2O_3 and SnO_2 . Then, the development of alternative transparent electrodes, ranging from multilayer structure to nanomaterials based on carbon or metal, over the last few years, will be presented. Finally, several of the conventional and emerging applications of TCO are described along with the additional features request behind the high electrical and optical transparency for their industrial applications.

1.1 Brief history of TCOs

Transparent conductive oxides (TCO) are a unique class of materials showing the coexistence of good electrical conductivity, like metallic materials, and wide optical transparency, like insulators.

These materials have a long history of development, since the beginning of the twentieth century (1907), when Bädeker, for the first time, reported CdO thin-film, yellowish in colour, which was optically transparent and electrically conducting [1]. Since then, many metal oxides have emerged as important transparent electrodes: tin oxide (SnO_2), zinc oxide (ZnO) and indium oxide (In_2O_3). After the second world war, due to the birth of the electronics industry, SnO_2 thin film were investigated for many optoelectronics applications such as antistatic windows and heated windows. The broad industrial application of TCO materials began at the end of 1960, when In_2O_3 was used in low-pressure sodium lamps in order to increase the lamp efficiency. It continued around 1970 with the advent of flat-panel display technology, when ITO (tin-doped indium oxide) became the most commercially material for transparent electrode, up to the present with the “green” technology (organic light-emitting diodes (OLED), low- ϵ saving energy window and photovoltaic applications) [2].

Historically, TCO composition is based on five set of binary compounds (see Fig.1) which, by doping on purpose, become conductive keeping high transparency in the visible wavelength range; this characteristic will be discussed into detail in the next paragraph. Although many transparent conductive oxides have been known for more than 50 years, for instance undoped and impurity-doped SnO_2 , ZnO and In_2O_3 , ITO has been the most studied and refined [3], due to the highest transparency for visible light combined with the highest electrical conductivity. Unfortunately, the persistent increasing of optoelectronic devices requiring one or more transparent conductor layers and the expanding use of ITO for the production of this layers is endangered by two key material issues about indium [1-4]:

- 1) Scarcity of indium that leads to a dramatic price increasing.
- 2) Indium toxicity and the ceramic nature of ITO that makes it an easily damaged layer.

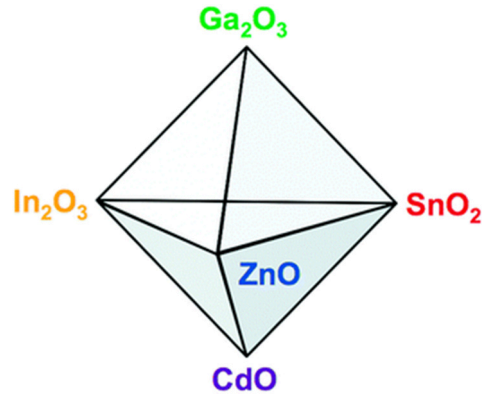


Figure 1: Composition space for conventional TCO materials

This resulted into an increasing research activity on alternative materials in order to search a good replacement to ITO for transparent electrodes. Thus, the field of transparent electrodes has exploded, including new n-type materials (amorphous TCOs), composite TCO materials, the synthesis of p-type materials as well as metal, graphene, polymer and carbon nano-composites transparent electrodes materials [4-6]. Some of them will be discussed in detail in paragraph 1.3. It is important to highlight that, although other transparent conductive oxides have been known for more than 50 years, for instance impurity doped- SnO_2 and ZnO , only the strong research efforts in the last decade allowed to gain a widespread attention. Especially, impurity doped- ZnO , after the steep increase in the use of thin film solar cells to produce “green” energy, have gained interest due to abundant, non toxic and not expensive elements.

At the present, Fig.2, the transparent electrode industry is dominated by just a few TCO materials based on binary compound, and the main markets for TCO are architectural window application and flat panel display,

closely followed by the rapidly growing photovoltaics industry [3]. While the penetration of these new transparent electrodes into applications is frozen for the next 10 years [7].

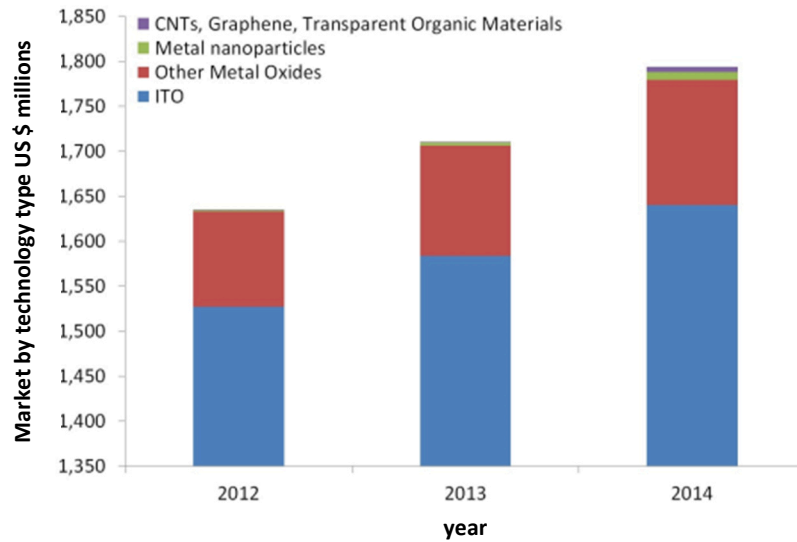


Figure 2: Market of transparent conductive materials.

Due to the advent of new technologies, such as e-paper, organic light emitting diode (OLED), organic solar cells, and the emerging areas of electrochromic windows and transparent electronics, the market is fastly being transformed. New applications and trends are also changing the required features, extending them beyond the combination of high conductivity and transparency. This is because each application presents several trade-offs between cost, conductivity, transparency, flexibility, patterning, etc. The key drivers are market tendencies towards low cost, large-sized devices, low power consumption, thinness, robustness and/or flexibility, patterning easiness and simplified value chain [7, 8].

Though it is clear that transparent conductive oxide and transparent electrodes are a developing field, it is no clear which of these new and

“rediscovered” transparent conductive oxide, and emerging materials will become the dominant player replacing ITO, also because this multiplicity of options also give rise to market uncertainty and confusion. However, it is assured that the market of transparent electrodes will continue to grow and these materials will find room in new field and niches marketplace [1-8].

1.2 Basic material physics of TCOs

As previously stated, TCOs offer the remarkable combination of high optical transparency and electrical conductivity. These two properties are usually decoupled, like in metals which have optimum electrical conductivity but totally reflect and absorb the sun light, or in insulators which are high transparent (e.g. glasses) to the sun-light but show very high electrical resistivity. For industrial applications, the electrical resistivity of a TCO should be $\sim 10^{-4} \Omega\text{cm}$ or less along with an optical band gap higher than 3.1 eV to guarantee an optical transmission of the light, in the visible range, up to 90 % [9].

Since commercially relevant TCOs are only n-type, while the research on p-type TCOs has begun in recent years, in this paragraph we provide a brief summary of the unique opto-electronic properties of n-type TCOs.

Here we present the fundamentals of physics of TCOs, centred on the structural properties and nature of doping processes by which is possible to control their electrical properties. Moreover, it will be shown how the optical properties are related to the free carrier concentration due to the doping; both the band-gap energy and the plasma wavelength change with the carrier density.

1.2.1 Band structures

TCOs are wide band gap semiconductor oxides with an optical band gap energy, E_{gap} , higher than 3 eV, so having a material transparent from near UV to near infrared. The high conductivity required for their application as transparent electrodes is due to the presence of free electrons. This can be achieved in TCO by two different ways: intrinsic defects or incorporation on purpose of extrinsic dopants. Defects and dopants produce shallow donor levels that act as a source of electrons for the conduction band. If a very large concentration of doping is achieved, the Fermi level penetrates the conduction

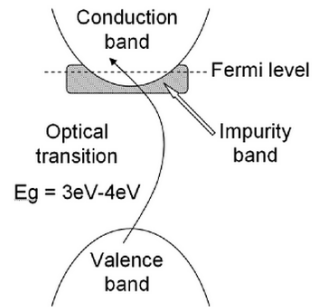


Figure 3: Schematic energy band structure of a degenerate TCO

band and the material starts to act more like a metal than as a semiconductor. In this case, the material is called degenerate semiconductors. Fig.3 shows an illustration of the band structure of an n-type TCO, which leads to the remarkable combination of high visible transparency and conductivity. Metal oxides such as ZnO, In_2O_3 , SnO_2 , with an optical band-gap higher than 3 eV are very suitable as transparent electrode. These oxides are insulators at room temperature and in the stoichiometric composition but, as said above, they can become conductive because of defects and impurities. Native point defects, like oxygen vacancies and/or interstitial metal atoms, can be formed during the deposition process, creating a non-stoichiometric material, while extrinsic doping can be achieved by introducing a metallic element, with the oxidation number +3, on substitutional lattice sites, or halogens with the oxidation number -1 on oxygen position. Doping with non-metallic elements is also common [2, 3, 9, 10], table 1.

Materials	Dopant or compound
SnO₂	Sb, F, As, Nb, Ta
In₂O₃	Sn, Ge, Mo, F, Ti, Zr, Mo, Hf, Nb, Ta, W
ZnO	Al, Ga, B, In, Y, Sc, F, V, S, Ge, Ti, Zr, Hf
CdO	In, Sn
Ga₂O₃	
ZnO-SnO₂,	Zn ₂ SnO ₄ , ZnSnO ₃
ZnO-In₂O₃	Zn ₂ In ₂ O ₅ , Zn ₃ Sn ₂ O ₆
In₂O₃-SnO₂	In ₂ Sn ₃ O ₁₂
CdO-SnO₂	Cd ₂ SnO ₄ , CdSnO ₃
CdO-In₂O₃	CdInO ₄
MgIn₂O₄	
GaInO₃, (Ga,In)₂O₃	Sn, Ge
CdSb₂O₆,	Y
Zn-In₂O₃-SnO₂	Zn ₂ In ₂ O ₅ -In ₄ Sn ₃ O ₁₂
CdO-In₂O₃-SnO₂	CdIn ₂ O ₄ - Cd ₂ SnO ₄
ZnO-CdO-In₂O₃-SnO₂,	

Table 1: TCO semiconductors for thin-film transparent electrodes

It is well known that intrinsically doped metal oxides exhibit poor electrical properties and are unstable when used at higher temperature. These issues make them not well suitable for practical transparent electrodes [3]. Therefore, for practical use, we will see that TCOs thin film are principally n-type extrinsic doped wide gap semiconductors as reported in table 2 [10]. These doped-metal oxides fall into two of the four families that historically dominates the field of transparent conductive oxides. These families can be defined by its structure type as given in table 1 [11]. The first family is n-type, related to zinc oxide, where positively-charged Zn atoms are tetrahedrally surrounded by oxygen atoms. ZnO metal oxide is the only one known to have this coordination. In the second family, the larger of TCOs, cations (Sn⁴⁺, In³⁺, etc.) are arranged in octahedral coordination; they also show an n-type behavior. Moreover, they are predominantly ionic bonded, with the exception of ZnO, a mix of ionic and covalent bond [12].

Structural feature	Carrier type	Examples
tetrahedrally-coordinated cations	n-type	ZnO
Octahedrally-coordinated cations	n-type	CdO, In ₂ O ₃ , SnO ₂ , In ₂ O ₃ , CdIn ₂ O ₄ , Cd ₂ Sn ₂ O ₄ , etc.
Linearly-coordinated cations	p-type	CuAlO ₂ , SrCu ₂ O ₂ , etc.
Cage Framework	n-type	12CaO-7Al ₂ O ₃

Table 2: Cation coordination and carrier type of TCO materials

The third family is the only one showing a p-type character (electrical conduction due to holes) which has cations linearly coordinated to oxygen. Generally TCO are n-type because of the iconicity of the metal oxide, which leads to a broadly conduction band and a strong localizations of the holes at the valence band edge. Hosono and co-workers [3] designed a strategy to introduce covalency bond and to induce the formation of an extended valence band structure. This strategy was based on selected elements synthesized into the ABO₂ delafossite structure where A can be Cu or Ag and B can be Al, Ga, Sc. Finally, in addition to the conventional TCO discussed above, another novel class of unconventional oxide based transparent electrodes, the cage-structure oxide 12CaO·7Al₂O₃ is also listed. It also shows an n-type behaviour.

1.2.2 Electrical transport in n-type TCOs

In order to understand the electrical properties of a n-type TCO, we can consider the schematic energy-band diagrams, reported in Fig.4, for In_{2-x}Sn_xO₃, where x is the tin atomic percentage, corresponding to two opposite situations, depending on the x amount [13].

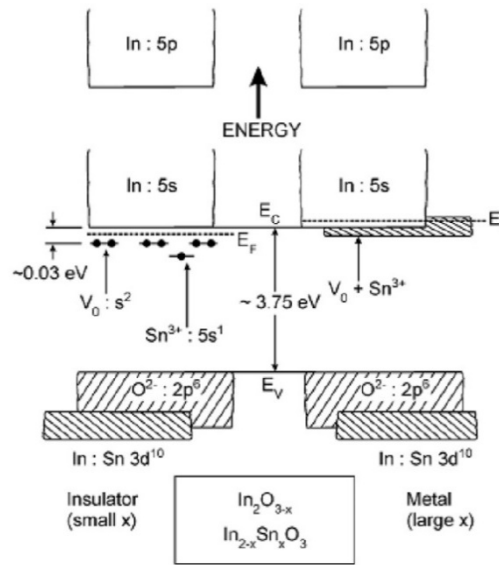


Figure 4: Schematic energy-band model of SnO_2 doped In_2O_3 for small and large amount x of extrinsic doping.

Since tin is a tetravalent metal (Sn^{4+}), substituting In^{3+} by Sn^{4+} provides a free electron to the conduction band. The doping process can also be affected by point defects, like oxygen vacancies (V_o). For each V_o (i.e. a missing O^{2-}), the In^{3+} provides two electrons to the 5s conduction band, which means that each V_o forms a shallow double donor state with an ionization energy close to the conduction bands. These point defects have got low energy of formation and good stability, explaining why oxygen sub-stoichiometric material is preferred.

On the left side of Fig.4, for low amount of doping x , we can observe a direct optical band-gap, E_{gap} , of about 3.75 eV, between the empty conduction band, formed by Indium 5s orbitals, and the full valence band formed by oxygen 2p⁶ and indium 3d¹⁰ orbitals. The 2p orbitals are very low in energy compared to 5s orbitals, explaining why a large band gap can be obtained in the intrinsic stoichiometric oxides. Moreover, it displays the shallow donor states Sn^{3+} and V_o , just below the bottom of the conduction

band energy. While, in the right side of Fig.4, for high doping, we observe a composition-induced transition from non-metallic to metallic type conduction: the conduction band is filled with delocalized electrons coming from the shallow state. The transition from insulating to metallic state of the materials is described by the Mott transition [14, 15], which takes place above a critical electrons density n_c (at $T = 0$ K) given by:

$$a_H n_c^{\frac{1}{3}} = 0.26 \pm 0.05 \quad (1)$$

with $a_H = \frac{h^2 \epsilon_0 \epsilon^m}{\pi e^2 m_c^*}$ the effective Bohr radius, where ϵ_0 and ϵ^m are the permittivity of the free space and of the host lattice, respectively, and m_c^* is the effective mass of the electron in the conduction band. Collected data from the literature [13, 16] suggest that the effective mass of electron in In_2O_3 is about a third of the electron mass, m_0 , of the hydrogen, i.e. $m_c^* \approx 0.35 m_0$, and $\epsilon^m \approx 4$. Using these values, we obtain $a_H \approx 1.3$ nm and consequently a critical electron density of about $6 \times 10^{18} \text{ cm}^{-3}$. Usually, the electron density in TCOs is above (up to 10^{21} cm^{-3}) this Mott critical density value, so it justifies the transition from insulator to metallic behavior in the transparent conductive oxides. The schematic representation in Fig.4 is valid for most binary metal oxide wide bandgap semiconductors; e.g. in ZnO the conduction band is also composed of s-like states of the cation (Zn 3s level) while the valence band is composed of O 2p and Zn 3d levels [17].

Once understood how we can increase the conductivity without degrading the transparency in TCOs materials, we can move into the transport theory within the framework of n-type degenerated semiconductors. The electrical properties of TCO can be well explained using the simple Drude free-electron theory [3, 18]. For carrier concentration n higher than n_c , one can consider having a full valence band and a parabolic band partially filled by a free electrons gas up to the Fermi energy: $E_F = \frac{h^2(3\pi^2 n)^{2/3}}{8\pi^2 m_c^*}$.

In the Drude theory, the differential equation of motion of the electrons as a function of the time and electric field is:

$$\frac{d\vec{p}(t)}{dt} = e\vec{E}(t) - \frac{\vec{p}(t)}{\tau} \quad (2)$$

$\vec{p}(t)$, e and τ are the electron's momentum, elementary charge and relaxation time, respectively, and $\vec{E}(t)$ is the electric field. The relaxation time is the interval of the time between successive random collisions of the electrons. Since we assume the case of steady state, the electron emerges from a collision in a random direction and the average electronic velocity is given by:

$$\langle \vec{v} \rangle = \frac{e\vec{E}}{m} \tau = \mu\vec{E} \quad (3)$$

Where m and μ are the free electron's mass and mobility, respectively. In general, taking into account that electrons are not totally free in the materials, we replace m with the effective-mass m^* . The concept of effective-mass arises because the electrons inside a crystalline (atoms of the material arranged in a lattice) are subjected to others forces, beyond the external electric field, that act to "alter its mass". If n electrons per unit of volume, in presence of a electric field \vec{E} , all move with velocity $\langle \vec{v} \rangle$, then the current density is $\vec{J} = n e \langle \vec{v} \rangle$.

According to the Ohm's law:

$$\vec{J} = \sigma\vec{E} = \vec{E}/\rho = n e \langle \vec{v} \rangle = ne\mu\vec{E} \quad (4)$$

where the conductivity, σ is given by:

$$\sigma = ne\mu \quad (5)$$

with $\mu = \frac{e\tau}{m^*}$ directly proportional to the electron relaxation time and inversely proportional to the electron effective mass.

The crucial requirement for a transparent electrode is an electrical conductivity as high as possible. The best strategies to maximize the conductivity in TCO materials are to increase the electron density and/or the mobility. Very high electron density (or doping), as we will discuss in detail in the following sub-paragraph, can be deleterious because it decreases the visible wavelength transparency; moreover n and μ are correlated so, behind a certain electron density value, the electron mobility is strongly reduced due to scattering of electrons with ionized impurities [9]. Therefore, it seems that the best strategy to increase the conductivity is to limit the electron density n while increasing the electron mobility μ . As mentioned earlier, mobility depends on effective-mass, m^* , and relaxation time, τ , which, in turn, depends on the average velocity and mean free path λ_e of the electron. These parameters in TCO are limited by several scattering processes [2, 3, 17] such as:

- *Ionized Impurity scattering*: the coulomb interaction between the ionized impurities (intrinsic and/or extrinsic donors) and the free electrons.
- *Grain boundary scattering*: they are especially present in polycrystalline films, disturbing the translation symmetry of the crystal and thus causing scattering. Grain boundary diffusion can be significant if the grain size, D , is comparable to the mean free path of the electron λ_e .
- *Optical and acoustic phonons scattering*: the former is the interaction between electrons and the electric field induced by electric polarization associated with the lattice vibration at optical frequencies. While the latter is the interaction between the electrons and the lattice deformations corresponding to pressure waves.
- *Piezoelectric scattering*: interaction between electrons and the electric field produced by the strain associated with acoustic phonons.

According to the Matthiessen rule [19], the total probability for an electron to be scattered in the unit time is the sum of the probabilities of the independent scattering processes:

$$\frac{1}{\tau_{tot}} = \sum_i \frac{1}{\tau_i} \rightarrow \frac{1}{\mu_{tot}} = \sum_i \frac{1}{\mu_i} \quad (6)$$

Therefore, the dominating scattering process will limit the electron mobility. As we can see from Fig. 5 [18], in the case of impurity doped ZnO (similar for impurity-doped In_2O_3 and SnO_2), at room temperature the dominating scattering process in TCO, (degenerately doped metal oxide, $n > 10^{19} \text{cm}^{-3}$) which limits the mobility, is the ionized impurity scattering.

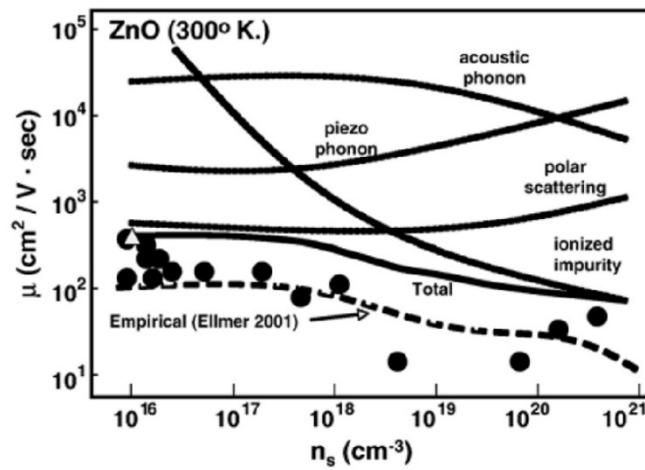


Figure 5: Influence of scattering processes on ZnO mobility, at room temperature, as a function of carrier concentration

Taking into account only this scattering mechanism and very high electron density, theoretical study established an absolute limit to the TCO conductivity of about 10^5 S cm^{-1} [20, 21]. About one order of magnitude higher than the best bulk metallic conductors (Ag, Cu, Au, Al, Mg, etc...).

Another parameter controlling the mobility is the effective mass: the smaller the effective mass, the higher the mobility is. The effective mass is considered an intrinsic parameter of a material that depends on its composition, however the effective mass has also a strong dependence on the electron concentration by means of the dispersion relation $E(k)$ [22]. The reciprocal of the effective mass is proportional to the curvature of the energy band, which in turn depends on the doping concentration. Therefore, we can conclude that the best strategy to achieve high conductivity is to maximize the product $n \mu$, eq. 5, by acting on these scattering mechanisms, which dominate the mobility at not very high doping concentration.

Finally, the electrical performances of a thin film are expressed by the electrical resistance offered by a square shaped sample of homogeneous material having a thickness d , known as sheet resistance $R_{sh} = \rho/d$ (Ω/square). The sheet resistance depends on the resistivity and thickness, while it does not depend on the film dimensions (length and width). Generally, a certain sheet resistance is needed in order to meet the electrical functionality of a specific application. For instance, a sheet resistances of 400-700 Ω/sq in touch screens, and below 10 Ω/sq in flat panel display and thin film solar cells [23].

1.2.3 Optical properties

As mentioned above, besides high electrical conductivity value $\sim 10^5 \text{ S cm}^{-1}$, from a practical point of view, TCO should have a wide transmission window in the near ultraviolet-visible-near infrared region. The optical transmission of a material is defined as the ratio between the incoming light intensity and the transmitted light intensity averaged over the wavelength range. Figure 6 shows the typical reflection, transmittance and absorption spectra of a TCO film, with a high transmission in the visible range [1]. The width of the transmission window is controlled by two different phenomena taking place in the near ultraviolet and infrared regions.

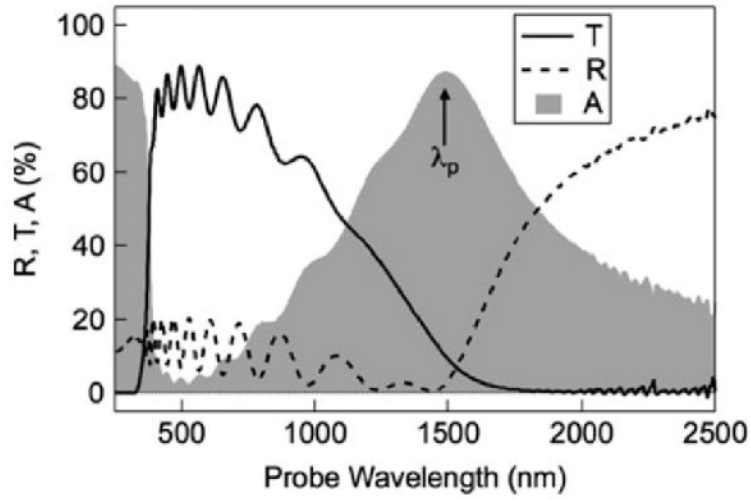


Figure 6: Optical spectra of typical transparent conductive oxides (ZnO)

In the near IR, for wavelengths $> \sim 1000$ nm, the decreasing of the transmission and the corresponding increasing of the reflection are due to the oscillations of the electrons in the conduction band, known as plasma oscillations, and intra-conduction band transitions. The characteristic frequency, known as plasma frequency ω_p , can be predicted using the Maxwell's equations of the electromagnetic theory within the framework of the Drude model: the free electrons in the conduction band are assumed to oscillate in response to the electric field components of the electro-magnetic field, i.e the light [3, 18]. We can define ω_p starting from the Drude form of the frequency-dependent dielectric function $\epsilon(\omega)$ of the material: $\epsilon(\omega) = \epsilon_1 + i\epsilon_2$, with the real part and imaginary parts given by:

$$\epsilon_1 = \epsilon_\infty - \frac{\sigma_0 \tau}{\epsilon_0} \left(\frac{1}{1 + \omega^2 \tau^2} \right) \quad \epsilon_2 = \frac{\sigma_0}{\epsilon_0 \omega} \left(\frac{1}{1 + \omega^2 \tau^2} \right) \quad (7)$$

where τ is the time between two successive collisions of the electrons in the lattice, $\sigma_0 = \frac{ne^2\tau}{m^*}$ the d.c. conductivity, ϵ_∞ the high-frequency permittivity, ϵ_0 the vacuum permittivity and ω the angular frequency of the electric field. Assuming that $\omega^2\tau^2 \gg 1$, the condition $\epsilon_1(\omega_p) = 0$ defines the plasma frequency of a TCO materials which is given by:

$$\omega_p^2 = \frac{ne^2}{\epsilon_\infty\epsilon_0m^*} \quad (8)$$

As we can see, there is a negative correlation between the electron density and the wavelength position in the IR region ($\lambda_p^2 \propto \frac{1}{n}$) where the free carriers start to reflect and absorb the incident electromagnetic wave. It is important to point out as for most TCO materials, due to their electron concentration, the plasma frequency falls in the near-infrared part of the spectrum. Therefore, if we increase by doping the number of electrons in the conduction band, the conductivity increases but also the IR absorption edge shifts towards shorter visible wavelength, narrowing the transmission window.

Across the visible range (400 – 800 nm) of the solar spectrum, the transmission reported in Fig. 6 is characterized by a transparency up to 90% and oscillations due to the thin film interference effects. The high transparency is correlated to the schematic electronic structure previously shown, in which p and s orbitals produce a completely filled lower valence and an upper conduction band separated by large band-gap energy, more than 3 eV, which makes the material transparent in this wavelength range.

Moving to shorter wavelengths, in the near UV range, we observe an abrupt drop in the transmission at around ~300 nm. The TCO material becomes opaque due to the absorption of UV photons: the photon energy is higher than the band-gap energy and photons are absorbed.

As above mentioned, mostly of TCO are n-type degenerate semiconductors. Due to the high doping, the Fermi level shifts into the

conduction band, hence the lowest energy states are occupied by free electrons, Fig. 7(a).

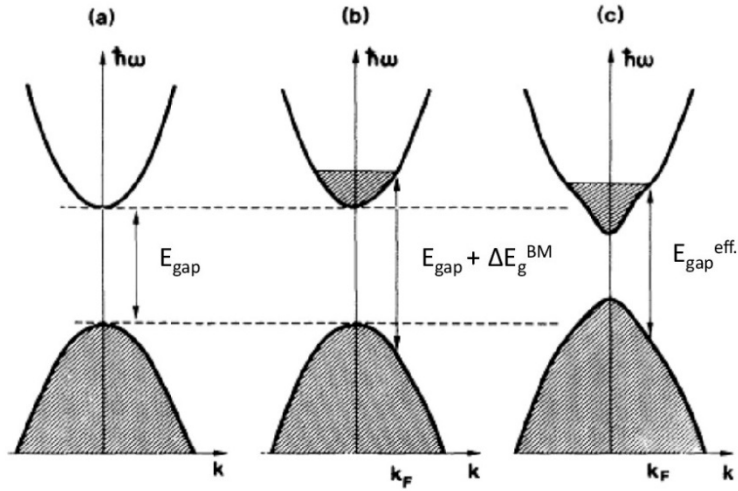


Figure 7: Burstein-Moss and Band-gap renormalization band-filling effect contributions to the E_{gap} .

Now, the photon energy required to promote an electron from the the valence band to the first available unoccupied state in the conduction band will be higher than the original band-gap energy, Fig. 7(b). The wider band optical gap is consequence of Pauli's exclusion principle that forbids excitation into occupied states in the conduction band. This doping-dependent E_{gap} shift is known as Burstein-Moss effect [24], responsible for the band-gap energy widening when increasing the doping concentration. The effective energy band-gap between the top of valence band and lowest empty state in the conduction band (both assumed parabolic) is given by:

$$E_{gap}^{eff} = E_{gap} + \Delta E_g^{BM} = E_{gap} + \frac{\hbar^2}{2m^*} (3\pi^2 n)^{2/3} \quad (9)$$

In this formula E_{gap} is the intrinsic bandgap of the material, m^* the effective mass of the electrons, and n the electron concentration. Here we have a direct relationship between the carrier concentration (doping) and the UV absorption edge, $\Delta E_g^{BM} \propto n^{2/3}$. By increasing the carrier concentration, we increase both the conductivity and the transmission windows, due to the shift of UV edge towards shorter wavelength. This feature does not correctly describe the experimental data, because we employed a rigid band model, which takes into consideration only the shift of the Fermi level into the conduction band. Due to the high electronic density we have to take into account the many-body effects (electron-electron and electron-impurity scattering), which leads to a band-gap narrowing [25, 26], Fig.7(c). Moreover, we can also observe a modification in the shape and curvature of the conduction band, which can modify the effective mass of the electrons. The theory, combining the many-body and Burstein-Moss effect, provides an effective band gap energy of:

$$E_{gap}^{eff.} = E_{gap}^0 + \Delta E_g^{BM} - \hbar\Sigma \quad (10)$$

The term $\hbar\Sigma$ in the equation represents the self energies due to many-body effect, causing a band gap narrowing that counteracts the Burstein-Moss effect. In particular, as demonstrated by Sernelius et al., for highly-doped ZnO this theory was found agree well with the experimental data [26].

In conclusion, the ideal TCO would be fully transparent in a wide range of wavelengths as well as have metal-like conduction but, as we have seen, the electrical and optical properties are intrinsically interconnected; therefore, TCO optimization needs the ability to trade-off carrier concentration against mobility to increase transmission window while maintaining high conductivity.

1.3 Development of alternative transparent electrodes

The best and most commercialized transparent electrodes are based on impurity-doped metal oxide, of which the most common is ITO. The key material issues related to indium and the persistent increasing in advanced devices that require transparent electrodes with higher conductivity and transparency, as well as other features such as lower cost and abundance elements, fabrication at low temperatures and plastic substrates, have stimulated the research, leading to many alternative and new transparent conductors.

This paragraph briefly explores the properties of these alternative transparent electrodes, principally covering multilayer structures and some of the current nano-materials coatings.

1.3.1 Multilayered Structures

Since early 1950s, very thin film of Ag, Cu or Au have been used as transparent electrode [27]. In order to achieve electrical properties very close to bulk material, the thickness of these films must be about 10 nm or more, depending on the metals, so have a continuous layer without holes or clusters. Higher thickness are even better for the electrical conductivity but, in this case, a high reflectance and absorption of the light are strong limiting factors for their application as transparent electrodes. In order to increase the transmittance through metal films and exploit its excellent electrical properties, TCO/metal/TCO multilayer structure have emerged as a promising alternative. Substantially, the outer TCOs act as anti-reflection coatings, so decreasing the reflectance [3]. A carefully adjustment of the refractive index and thickness in these structures can decrease the reflectance within a broad wavelength range. Usually the best electro-optical performances of a standard ITO are obtained with thickness higher than 500

nm. These very ultra-thin multilayer structures such as ITO/Ag/ITO, with 100 nm of overall thickness, can provide a significant drop in indium consumption and allow the achievement of electrical-properties comparable to single ITO. Analogous performance has been achieved with other TCO/metal/TCO, as reported in table 3 [28].

TCO/metal/TCO description	substrate	R_{sh} [Ω/sq]	T [%]
ITO 50 nm/Ag 8 nm/ITO 50 nm	Glass	15	89
GIO 40 nm/Ag 8 nm/GIO 40 nm	Glass	11.3	92.9
ITO 37 nm/Ag(PdCu) 8 nm/ITO 37 nm	Glass	10	89
AZO 40 nm/Ag(PdCu) 8 nm/AZO 40 nm	Glass	10	88
ITO 30 nm/Ag 8 nm/ITO 30 nm	PEN	6.8	85
ZnO 57 nm/Ag 9 nm/ZnO 40 nm	Glass	7	95
ITO 35 nm/Ag 10 nm/ITO 35 nm	PET	10	77
ITO 35 nm/Ag 10 nm/ITO 35 nm	Glass	9	80
SnO ₂ 45 nm/Ag 10 nm/ITO 45 nm	Arton	7	85
GZO 30 nm/Ag 10 nm/GZO 40 nm	Glass	7	90.7
ITO 30 nm/Ag 10 nm/ITO 30 nm	Glass	6	90
ITO 40 nm/Ag 10 nm/ITO 40 nm	Glass	6	87
ITO 45 nm/Ag 10 nm/ITO 45 nm	Arton	6	86
AZO 40 nm/Ag 10 nm/AZO 40 nm	PET	6	85
ITO 50 nm/AgCu-alloy 10 nm/ITO 50 nm	Glass	5.7	83
ITO 50 nm/Ag 10 nm/ITO 50 nm	Glass	5	88
ZnO 35 nm/Ag 12 nm/ZnO 35 nm	PET	10	75
GZO 30 nm/Ag 12 nm/GZO 30 nm	PES	7	87.2
IZO 30 nm/Ag 12 nm/IZO 30 nm	PET	6.9	84.8
AZO 40 nm/Ag 12 nm/AZO 40 nm	Glass	7	82
GZO 40 nm/Ag 12 nm/GZO 40 nm	Glass	6	87
ITO 40 nm/Ag 12 nm/ITO 40 nm	PES	4.3	89.3
ITO 50 nm/Ag 14 nm/ITO 50 nm	PET	11	81
ITO 70 nm/Ag 14 nm/ITO 70 nm	PPC	6.5	68
IZTO 30 nm/Ag 14 nm/IZTO 30 nm	PET	5	86
IZO 40 nm/Ag 14 nm/IZO 40 nm	Glass	4.2	87.7
ITO 40 nm/Ag 15 nm/ITO 40 nm	Glass	4.2	85
ITO 42 nm/Ag 15 nm/ITO 42 nm	Glass	3.3	85
ITO 43 nm/Ag 16 nm/ITO 43 nm	Glass	8.9	79.4
ITO 40 nm/Ag 16 nm/ITO 40 nm	Glass	4.4	86.5
ITO 50 nm/Ag 17 nm/ITO 50 nm	PET	6.7	83.2
ITO 54 nm/Ag 20 nm/ITO 54 nm	Glass	3.5	75
ZnO 50 nm/Cu 5 nm/ZnO 50 nm	Glass	10	83
ZnO 30 nm/Cu 6 nm/ZnO 30 nm	PEN	10	88
AZO 40 nm/Cu 8 nm/AZO 40 nm	Glass	9	84
ITO 40 nm/Cu 14 nm/ITO 40 nm	Glass	6	69
ITO 30 nm/Cu 16 nm/ITO 30 nm	Glass	6	88
AZO 50 nm/Au 9 nm/AZO 50 nm	Glass	12	83
ITO 50 nm/Au 10 nm/ITO 40 nm	PC	5.6	72
IZO 40 nm/Au 12 nm/IZO 40 nm	Glass	5.5	81

Table 1: Sheet resistance (R_{sh}) and optical transmittance (T) values reported for several TCO/metal/TCO structures grown on different substrates.

Usually, the best electrical performance of many TCOs are obtained after thermal treatment at high temperature, more than 250 °C, during or after the deposition process, which are incompatible with thermoplastic substrates. All the multilayer structures listed in table 3 have been prepared by several deposition techniques, such as sputtering and evaporation, on different substrates, among which PEN (polyethylene naphthalate), PET (polyethylene terephthalate) and PC (polycarbonate). The main feature of these structures is the achievement of the high visible transmittance and low electrical resistance at room temperature deposition, which offers the chance to substitute rigid glass with thermoplastic polymers as substrate. Moreover, the very thin thickness of the multilayer structure and the flexibility of the metallic interlayer assure a better mechanical stability than thicker TCO single layers [29]. From the point of view of the manufacturing, advantages like simple deposition techniques, flexibility of the material and lower production costs (plastic substrate and no thermal treatments) make multilayer structures extremely favourable in the development of low-cost, high quality, flexible electronics and photovoltaic devices. Other characteristics such as surface roughness, thermal stability [30,31] and durability against humidity and chemical agent have been evaluated by several tests [32-34], because in addition to the crucial requirements of flexibility, low cost and high conductivity-transparency these features can also be decisive for their commercial applications. Nowadays, these features allowed the use in several conventional and emerging applications such as flexible random access memories [35], organic photovoltaic devices (OPVs) [29, 36-38] and organic luminescent displays (OLEDs) [39, 40].

1.3.2 Emerging nanomaterials

Over the last years, a high level of technological abilities, from synthesis to in-depth analysis, opened the door to several emerging nanoscale materials. These new materials offer new physical properties

combined with low costs, making them excellent candidates for the next generation of transparent conductors [3-6]. Here we will focus on carbon nanostructures such as graphene and carbon nanotubes, and metal nanostructures, as silver nanowire networks.

Single or multiple graphene sheets, Fig.8 (a), are rapidly emerging as transparent electrodes due to the intrinsic high in-plane conductivity and transmittance.

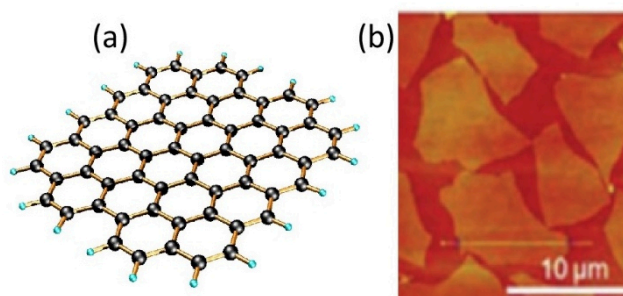


Figure 8: (a) Carbon atoms arranged in a graphene lattice, (b) AFM of a network of random graphene flakes.

The high conductivity in a single layer of graphene is due to the low concentration of charge carriers and very high electron mobility, up to $\sim 10^4$ $\text{cm}^2/\text{V s}$ over the sheet, like a two-dimensional electron gas [41, 42]. While the high optical transmittance is due to the low optical opacity of a single graphene layer, about 2.3%. Moreover, as predicted by Peumans et al. the sheet resistance and the optical transmittance of a large and defects-free structure of graphene, linearly decrease with the number of layers N : $R_{\text{sh}} \sim 62.4/N \Omega/\text{sq}$ and $T \sim 100 - 2.3N \%$ [42-45], respectively.

The extensive research and the various fabrication methods developed to study and grow large, defects-free and industrially scalable graphene sheets, such as mechanical exfoliation of highly oriented pyrolytic graphite (HOPG) [46], chemical vapor deposition on Ni films [47] and solution

based process [48], have drastically improved the opto-electrical properties of this material. From $R_{sh} \sim 2000 \text{ } \Omega/\text{sq}$ and $T \sim 85\%$, to $R_{sh} \sim 700 \text{ } \Omega/\text{sq}$ and $T \sim 90\%$ in the cases of solution and CVD processes, respectively. However, the high sheet resistance prevents their application in solar cells and flat panel display, which require a value of $\sim 10 \text{ } \Omega/\text{sq}$. With the goal of decreasing the sheet resistance, two main strategies are pursued: to increase the carrier mobility synthesizing large and single sheets without defects, or to increase the carrier concentration by doping. For example, Bae et al. [4] achieved sheet resistance and optical transmission of $\sim 30 \text{ } \Omega/\text{sq}$ & $T \sim 90 \%$, respectively, growing a layer-by-layer stack to fabricate a doped four-graphene layer film by chemical vapor deposition onto Cu foil and then transferring it onto plastic substrate. For practical use, thermal [49] and mechanical/electrical stability [50] have also been demonstrated. These outstanding properties of graphene make it very attractive for applications in many fields, from flexible electronics to photovoltaics. However, large-area deposition technologies of graphene films are still in their infancy, and a main drawback is related to the higher temperature ($\sim 700\text{-}900 \text{ } ^\circ\text{C}$) needed to grow graphene. Moreover, instead of a single sheet of graphene, often a network of graphene flakes is synthesized, Fig.8 (b), which shows high resistivity due to the contact areas [4].

Another emerging subclass of carbon based transparent electrodes is carbon nanotubes (CNTs), cylindrical structures of carbon atoms, Fig. 9. Although the first experimental synthesis was made in the early 1990s [51], and the subsequent studies have shown amazing electrical (mobility higher than $10^5 \text{ cm}^2/\text{V s}$), optical and mechanical properties, CNTs needed several years to find widespread appeal as transparent electrodes due to several issues.

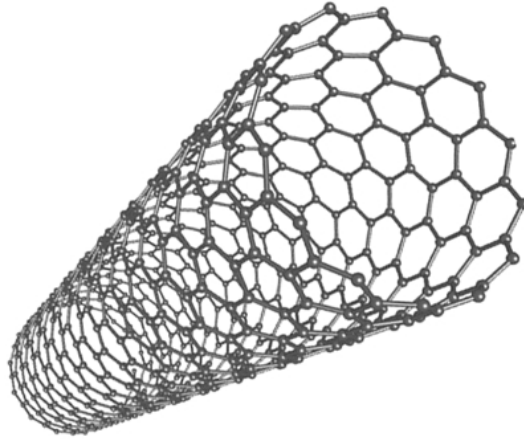


Figure 9: Single walled CNT.

One of major factor limiting their application is the high conductivity of CNTs compared to single CNT, because the high junction resistance between CNTs, typically of the order of 200 k Ω -20 M Ω , produces a drastically increasing in the conductivity. There has been much work done to increase the conductivity value, such as doping with nitric acid or using longer CNTs [52, 53], however films of CNTs still have a much lower opto-electrical performance than commercial ITO. Another impediment is related to the material synthesis. Typically, as produced CNT films consist of a mixture of both semiconducting and metallic CNT, with the metal/semiconductor ratio influencing the opto-electrical performances. The metallic CNTs have a much higher conductivity than semiconductor ones, moreover the latter absorb light, so reducing the optical transmission. The junction resistance between two metallic CNTs is much lower than metallic-semiconductor CNTs, which form a schottky barrier, therefore the whole conductivity can be decrease if we made a film entirely of metallic CNTs [54]. Although some methods have been introduced to separate metal and semiconductor CNTs

or to synthesize only metallic CNTs, these challenges are still to be won, also including large scale low-cost fabrications for commercial applications.

In order to use the high conductivity of silver and also to avoid the absorption and/or reflection in the visible/NIR range, silver ultra-thin films have been replaced with silver nanowires networks [55-58]. One of the main advantages of using nanowires lies in the increased transparency, because the light can pass through the empty spaces. Another advantage is the simple and low cost solution-based synthesis, especially when they are fabricated as network of silver nanowires randomly oriented. Silver nanowire films can be fabricated either at room temperature, or at low annealing temperatures [59, 60], which make them compatible with plastic flexible substrates. Networks of silver nanowires can achieve low sheet resistance, $R_{sh} \sim 10-20 \Omega/sq$, and high transparency, $T \sim 90\%$ by using pure and smooth metallic nanowires with suitable diameter and length [4]. Moreover, a denser network will result in a decreasing of the sheet resistance but also of the transmission of light, Fig.10. Recent works proved that sheet resistance and surface roughness of this mesh can be decreased by mechanical pressing, melting the nanowire junctions [59]. This network also shows the noticeable feature of scattering the transmitted light, known as haze, which is not desired for displays and touch panels but it can be very useful to increase the light absorption in solar cells. In order to decrease the haze, nanowires can be in theory made with diameters smaller than 50 nm, although, to date, the published results range from 50 to 200 nm, with a length in between 1 and 20 μm . In any case, thinner nanowires would result in a worsening of the conductivity due to the increasing of surface scattering.

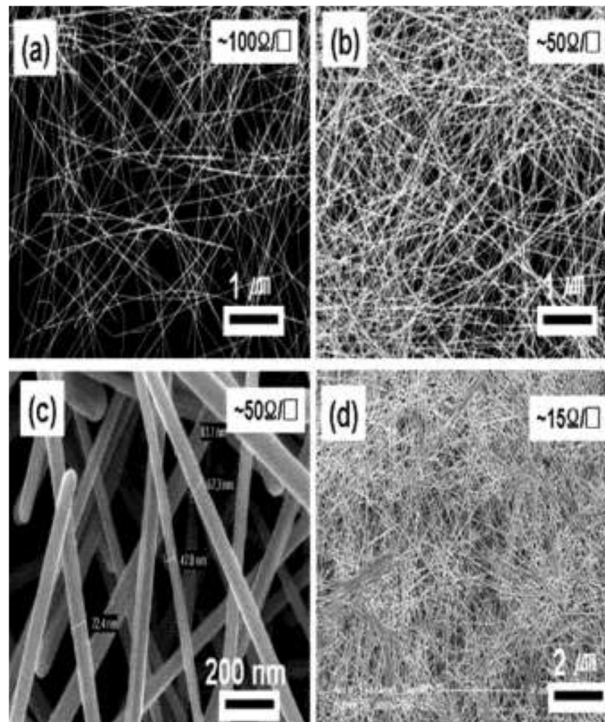


Figure 10: SEM images of Ag NW films with different densities. The different densities lead to different sheet resistances: (a) 100, (b), (c) 50, and (d) 15 Ω /Sq.

Although a network of silver nanowires is low cost, flexible, and shows desirable transparency and conductivity values, there are some issues that need to be addressed before these transparent electrodes can be used in commercial devices, such as the structurability, the long-term stability and large-scale fabrication.

In conclusion, in Figure 11 reports the best optical (lower graph of (a)) and electrical (b), results for CNTs, graphene, silver nanowires and standard transparent electrodes, along with the luminosity function of the human eye and the spectral irradiance from the Sun under AM1.5 conditions (upper part of (a)) [2].

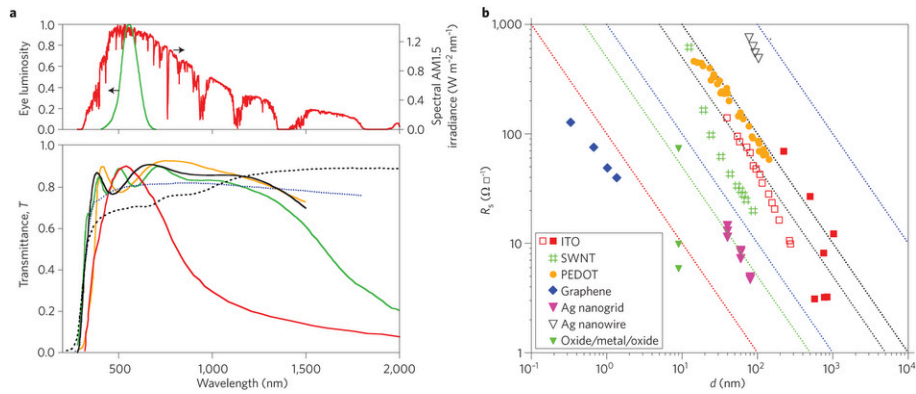


Figure 11: (a) spectral transmission of several transparent electrodes: ITO (black line), FTO (green line), AZO (orange line) carbon nanotubes (dashed black line), silver nanowires (dotted blue line) and SnO₂/Ag/SnO₂ (red line). (b) sheet resistance, R_{sh} , as a function of the thickness for different transparent electrodes.

Although these new materials show a significant progress in improving optoelectronic performances, and also offer some advantages such as low costs, room temperature deposition, flexibility, etc., they still have to reach the performance of ITO and, moreover, to demonstrate the capability of large area industrial production.

1.4 Industrial applications

TCOs materials found a widespread use in many important technologies ranging from architectural (low- ϵ windows) to information & energy applications (e-paper, display, touch-screen, photovoltaics) [1-8]. Briefly, several of these consolidate and emerging technologies will be described in the following two sub-paragraphs.

1.4.1 Solar energy

Over the last decade there has been an increasing interest in the use of photovoltaic (PV) technology as a renewable and inexpensive energy source, which has resulted in a plenty of solar cells technologies: mono and polycrystalline silicon solar cells, thin-films, organic and hybrids. While the absorber materials can vary a lot, each one with advantages and disadvantages, all photovoltaic technologies use very similar geometry and operation mode [61]. The solar cell is fabricated by sandwiching the absorber materials between two electrodes (with the exception of the all back contact solar cells). One of the electrodes, "front or top" electrode, is typically a transparent conductive oxide material, and usually is placed between a transparent supporting substrate (glass) and the absorber material. The sunlight passes through the glass and TCO before it is absorbed by the active layer. The "back or bottom" electrode which is opposite to the front electrode, generally comprises a metal thin-film or alternatively a transparent conductive material. Some of the most consolidated and emerging photovoltaic devices, with the required properties of TCOs, are listed in table 4 [62].

As we can see, beyond the crucial requirements of high transmission and high conductivity, the choice of the best TCO for a specific solar cell should also be considered, along with processing, cost, material compatibility, work function and energy band alignment. In fact, for a widespread use of PV technologies, it is essential to take into account lower production cost and environmental impact. In this context, the high price, scarcity and toxicity of In are a remarkable drawback, which endangered the expanding use of ITO and the development of In based solar cells.

Cell type	TCO in current use	TCO needs	Materials goal
Heterojunction with intrinsic thin layer (HIT) cell	ITO	Smooth and good interfacial properties, optimum conductivity, low temperature deposition, light trapping	IZO, indium-free material, ZnO
Copper indium gallium selenide (CIGs)	i-ZnO/Al:ZnO	Inferfacial stability to CdS, Low temperature deposition, resistance to diffusion and shorting, need to make/improve the junction.	Single-layer TCO to replace two layers and CdS layer
CdTe	SnO ₂ Zn ₂ SnO ₄ /Cd ₂ SnO ₄	Stable interface to CdS/CdTe at high temperature, diffusion barrier	Doping of Zn ₂ SnO _x materials, Single layer TCO
Nano-hybrid polymer cell	ZnO, SnO ₂ ,TiO ₂	Nanostructure with right length scale, work-function, interface with organic and correct doping level	Self-organized structures core-shell structure, new non conventional TCOs
Grätzell cell	TiO ₂	Nanostructure with high electron mobility	Improved TiO ₂ morphology and possible used of doped materials, new non-TiO ₂ materials
Amorphous Si	SnO ₂ ,ITO and ZnO many cells employ two TCOs	Temperature and chemical stability, and appropriate texture for both TCO	Higher conductivity, texture and ohmic contact for both TCO

Table 2: Features required to TCO employed in solar cells and new materials goals.

In the Heterojunctions with Intrinsic Thin-film layer (HIT) solar cell, Fig 12 (a), two TCO layer are employed, one for the top and one for the bottom of the cells [62,63].

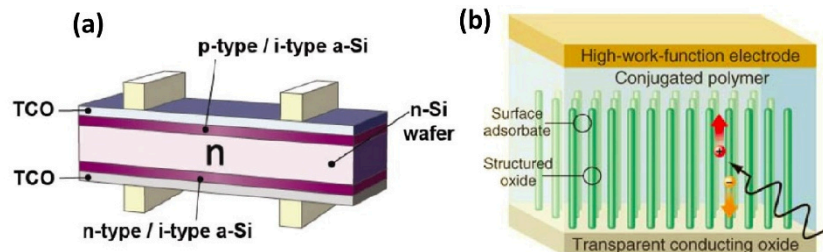


Figure 12: (a) Typical configuration for HIT solar cell. (b) Schematic view of an organic photovoltaic cell using a nanostructured TCO grown on a planar TCO layer and intercalated with a conjugated polymer

As the lateral conductivity of doped a-Si:H layers is poor, the front of the devices must be coated with a TCO layer to transport charge to the device terminals. The front TCO also serves as an antireflecting coating in order to limit losses. Usually ITO has been used, but the low thermal stability of crystalline/amorphous structure limited the thermal treatments up to temperature value that does not allow the reaching of the ITO's best performance. For this reason, there is an increasing interest to use amorphous IZO, which shows high quality even at room temperature deposition. This represents an important driving factor to further improve the device performances. While the other TCO acts primarily as a transparent electrode without incurring contact resistance losses.

In wafer-based and thin-film type solar cells, a specific feature, beyond high transparency and conductivity, is required for TCO: texturing. A textured surface will not only reduce reflection, but will also give a longer optical path to the light inside the absorber material (light-trapping). As a result, the incoming light will be completely absorbed during one single pass. The light scattering is usually achieved by texturing TCO substrate (before or after the deposition) by wet-chemical and lithography etching steps. Therefore, the

optimization of the texturing technique can lead to an improving of the solar cells efficiency and a reduction of the absorber thickness, with strong advantages on the production costs.

In CdTe and Cu(InGa)Se₂ (known as CIGS) thin film solar cells, low temperature deposition and thermal stability after the deposition also play a crucial role for choosing the most suitable TCO. In particular, in CIGS solar cells, a three-layer TCO (CdS/i-ZnO/AZO) is used, which acts both as defect passivation layer and as transparent electrode. While in cadmium telluride solar cells, where the CdTe/CdS stack begins with TCO coated glass, the goal is to find an optimum tradeoff between the resistivity value and the ability to act as barrier against diffusion during the high temperature deposition of the CdTe layer.

Transparent conductive oxides are traditionally used in devices as thin film, while hybrid and dye sensitized (Grätzel) solar cells, Fig.12 (b), require TCO materials of different type, for instance, three dimensional nanostructures like nanorods. Nanostructured TCO electrodes help to maximize the inorganic/organic interface and reduce the distance between the organic film and the TCO contact. The poor exciton and charge carrier transport in the organic layer require very short distance, less than 10 nm, between TCO and organic layer for a successful device. Additional properties of the TCO used to contact the organic layer are important, such as work function, surface morphology and chemistry. The work function must be optimized to match the energy levels in the organic absorber material in order to facilitate the charge collection, while the surface chemistry is critical for the charge transfer at the interface.

1.4.2 Towards transparent electronics

After the advent of flat-panel display (FPD) technology, around 1970, this field became one of the largest and fastest-growing applications of TCO. Traditionally, this role has been well performed by ITO due to its excellent electro-optical properties and the relative ease of acid etching.

Briefly, in FPD each pixel consists of a layer of nematic liquid crystal aligned between two ITO thin film layers, and two polarizing filters (parallel and perpendicular) which have axes of transmission (in most of the cases) perpendicular to each other. Without the liquid crystal between the polarizing filters, due to their polarization, the light passes through the first filter but will be blocked by the second filter. Viceversa, by controlling the applied voltage across the liquid crystal layer in each pixel, we will modify the polarization of the light. Therefore, light can pass through the liquid crystal with different intensities, thus constituting different levels of gray. Generally ITO is etched as pattern of lines oriented perpendicular to each other on the two substrate, this allows addressing individual pixels by applying a voltage to the row and column lines which intersect at a given pixel [64,65]. Thus patterning of the ITO film is a crucial requirement.

Touch panels are the other devices using TCO thin film, with an exponential growth rate. In touch screen applications, usually, very low overall sheet resistance of TCO is not fundamental, but rather the long-term post-deposition stability and mechanical durability. In this application, TCO allowed to define the x-y position on the surface of the screen, therefore a change in the resistance, either locally or globally, leads to a shift of the contact position [64, 65].

Another dominant markets for TCOs is the architectural window applications. In application such as defrosting windows, TCO coated glass is used because by applying an electrical current to the TCO layer, it warms up due to the Joule effect and prevents the condensing of the air. While in the low- ϵ windows the conductivity of TCO is irrelevant and they are used only for their optical properties: the high reflectivity in the the infrared spectral range. To this purpose, depending on which side the TCO layer is exposed, i.e. outside or inside the building, we can control the heat and light flux passing through the window. This feature is used to minimize air conditioning in summertime and heating in the wintertime. Fluorine doped tin oxide (FTO) is the TCO most often used in this application due to the advantages that it is inexpensive both in terms of raw material and processing .

In addition to the conventional and consolidated TCO applications, there is an emerging area that could rapidly be mature and increasing the TCO use on a large scale: oxide based thin film transistor (TFTs and T(transparent)TFTs) [3]. All TCOs discussed and employed are n-type semiconductors, however p-type TCOs have been also developed and represent an important milestone in transparent electronic, allowing fabrication of wide band-gap p-n junction. Though significant progresses have been achieved over the last ten years, further intensive research is needed because p-type TCOs are still a critical issues, as demonstrated by p-type ZnO. High carrier concentration ($>10^{19}\text{cm}^{-3}$), high mobility and persistence of p-type behaviour for long times is needed in order to win the challenge to obtain p-type TCO with resistivity lower than about $10^{-3}\ \Omega\text{cm}$ [3-17]. Another important issue is the development of transparent amorphous semiconductors ($[\text{In}_2\text{O}_3]_x[\text{ZnO}]_{1-x}; [\text{Ga}_2\text{O}_3]_x[\text{In}_2\text{O}_3]_{1-x}$) discovered by the Hosono group more than 10 years ago [66-68]. The advantages of these materials are the deposition at lower temperature (amorphous material) with respect to crystalline TCO materials and performances comparable to the TCO polycrystalline materials. Other remarkable properties are their high temperature stability and flexibility, thus allowing the use of plastic substrate. Therefore, if a pn-junction with good performance and stability is fabricated with polycrystalline and/or amorphous TCOs on plastic substrate by cheap deposition technique, this would be a breakthrough for flexible electronics.

References

- [1] K. Bädeker, *Ann. Phys. (Leipzig)* **22**, 749 (1907).
- [2] K. Ellmer, *Nature Photonics* **6**, 809 (2012).
- [3] D. S. Ginley, H. Hosono, D.C. Paine, *Handbook of transparent conductors*, Springer 2011.
- [4] D. S. Hecht, L. Hu, G. Irvin, *Adv. Mater.* **23**, 1482 (2011).
- [5] F. Bonaccorso, Z. Sun, T. Hasan, A.C. Ferrari, *Nature Photonics* **4**, 611 (2010).
- [6] Y. Sun, Q. Wu, G. Shi, *Energ. Env. Sci.* **4**, 1113 (2011).
- [7] C. Thiele & R. Das, *Transparent Conductive Films (TCF) 2012-2022*, IDTechEx 2013.
- [8] K. Ghaffarzadeh & R. Das, *Transparent Conductive Films (TCF) 2014-2024*, IDTechEx 2014.
- [9] L. Castaneda, *Materials Science and applications* **2**, 1233 (2011).
- [10] T. Minami, *Semicond. Sci. Technol.* **20**, S35 (2005).
- [11] B.J. Ingram, G.B. Gonzalez, D.R. Kammler, M.I. Bertoni and T.O. Mason, *Journal of Electroceramics* **13**, 167 (2004).
- [12] H. Morkoç, Ü. Özgür, *Zinc Oxide: Fundamentals, Materials and Device Technology* WILEY-VCH Verlag GmbH & Co 2009.
- [13] P.P. Edwards, A. Porch, M.O. Jones, D.V. Morgan, R.M. Perks, *Dalton Trans.* **19**, 2995 (2004).
- [14] N.F. Mott, *Can. J. Phys* **34**, 1356 (1956).
- [15] N.F. Mott, *Philos. Mag.* **6**, 284 (1961).
- [16] H. Köstlin, R. Jost & W. Lems, *Phys. Status Solidi A* **29**, 87 (1975).
- [17] K. Ellmer, A. Klein, B. Rech, *Transparent conductive Zinc Oxide: Basics and Applications in Thin Film Solar Cells*, Springer 2008.
- [18] G. J. Exarhos X.-D. Zhou, *Thin Solid Films* **515**, 7025 (2007).
- [19] S. Calnan, A.N. Tiwari, *Thin Solid Films* **518**, 1839 (2010).
- [20] J.R. Bellingham, W.A. Phillips, C.J. Adkins, *J. Mater. Sci. Lett.* **11**, 263 (1992).

- [21] M. Chen, Z.L. Pei, X. Wang, Y.H. Yu, X.H. Liu, C. Sun, L.S. Wen, *J. Phys. D: Appl. Phys.* **33**, 2538 (2000).
- [22] V. Kaydanov, Thesis, Colorado School of Mines (1999)
- [23] M. Fahland, T. Vogt, W. Schoenberger, N. Schiller, *Thin Solid Films* **516**, 5777 (2008).
- [24] E. Burstein, *Phys. Rev.* **93**, 632 (1954)
- [25] B.E. Sernelius, *Phys. Rev. B* **36**, 4878 (1987)
- [26] B.E. Sernelius K.-F Berggren, Z.-C. Jin, I. Hamberg, C.G. Granqvist, *Phys. Rev. B* **37**, 10244 (1988)
- [27] C.G. Granqvist, *appl. Opt.* **20**, 2606 (1981)
- [28] C. Guillén, J. Herrero, *Thin Solid Films* **520**, 1-17 (2011).
- [29] Y.S. Park, K.H. Choi, H.K. Kim, *J. Phys. D: Appl. Phys.* **42**, 235109 (2009).
- [30] Y.S. Jung, Y.W. Choi, H.C. Lee, D.W. Lee, *Thin Solid Films* **440**, 278 (2003).
- [31] D.R. Sahu, C.Y. Chen, S.Y. Lin, J.L. Huang, *Thin Solid Films* **515**, 932 (2006)
- [32] K. Koike, S. Fukuda, *J. Vac. Sci. Technol. A* **26**, 444 (2008).
- [33] E. Ando, M. Miyazaki, *Thin Solid Films* **392**, 289 (2001)
- [34] J.Y. Lee, J.W. Yang, J.H. Chae, J.H. Park, J.I. Choi, H.J. Park, D. Kim, *Opt. Commun.* **282**, 2362 (2009).
- [35] J.W. Seo, J.W. Park, K.S. Lim, S.J. Kang, Y.H. Hong, J.H. Yang, L. Fang, G.Y. Sung, H.K. Kim, *Appl. Phys. Lett.* **95**, 133508 (2009).
- [36] J.A. Jeong, H.K. Kim, *Sol. Energy Mater. Sol. Cells* **93**, 1801 (2009).
- [37] J.A. Jeong, Y.S. Park, H.K. Kim, *J. Appl. Phys.* **107**, 023111 (2010).
- [38] M. Chakaroun, B. Lucas, B. Ratier, C. Defranoux, J.P. Piel, M. Aldissi, *Thin Solid Films* **518**, 1250 (2009).
- [39] K.H. Choi, H.J. Nam, J.A. Jeong, S.W. Cho, H.K. Kim, J.W. Kang, D.G. Kim, W.J. Cho, *Appl. Phys. Lett.* **92**, 223302 (2008).
- [40] S.W. Cho, J.A. Jeong, J.H. Bae, J.M. Moon, K.H. Choi, S.W. Jeong, N.J. Park, J.J. Kim, S.H. Lee, J.W. Kang, M.S. Yi, H.K. Kim, *Thin Solid Films* **516**, 7881 (2008).
- [41] de Heer W.a, *MRS bulletin* **36**, 632 (2011)

- [42] K. S. Novoselov, A. K. Geim, S. V. Morozov, D. Jiang, Y. Zhang, S. V. Dubonos, I. V. Grigorieva, A. A. Firsov, *Science* **306**, 666 (2004) .
- [43] J. B. Wu, M. Agrawal, H. A. Becerril, Z. N. Bao, Z. F. Liu, Y. S. Chen P. Peumans, *ACS Nano* **4**, 43 (2010).
- [44] R. R. Nair, P. Blake, A. N. Grigorenko, K. S. Novoselov, T. J. Booth, T. Stauber, N. M. R. Peres, A. K. Geim, *Science* **320** ,1308 (2008).
- [45] H. A. Becerril, J. Mao, Z. Liu, R. M. Stoltenberg, Z. Bao, Y. Chen, *ACS Nano* **2**, 463 (2008).
- [46] K. S. Novoselov, A. K. Geim, S. V. Morozov, D. Jiang, M. I. Katsnelson, I. V. Grigorieva, S. V. Dubonos, A. A. Firsov, *Nature* **438**, 197 (2005).
- [47] A. Reina, X. T. Jia, J. Ho, D. Nezich, H. B. Son, V. Bulovic, M. S. Dresselhaus, J. Kong, *Nano Lett.* **9**, 30 (2009).
- [48] V. C. Tung, M. J. Allen, Y. Yang, R. B. Kaner, *Nat. Nanotechnol.* **4**, 25 (2009) .
- [49] X. Wang, L. J. Zhi, K. Mullen, *Nano Lett.* **8**, 323 (2008).
- [50] K. S. Kim, Y. Zhao, H. Jang, S. Y. Lee, J. M. Kim, K. S. Kim, J.-H. Ahn, P. Kim, J.-Y. Choi, B. H. Hong, *Nature* **457**, 706 (2009)
- [51] S. Iijima and T. Ichihashi, *Nature* **363**, 603 (1993).
- [52] H. Z. Geng, K. K. Kim, K. P. So, Y. S. Lee, Y. Chang, Y. H. Lee, *J. Am. Chem. Soc.* **129**, 7758 (2007).
- [53] D.S. Hecht, L.Hu, G. Gruner, *Appl. Phys. Lett.* **89**,133112 (2006).
- [54] M. S. Fuhrer, J. Nygård, L. Shih, M. Forero, Y. G. Yoon, M. S. C. Mazzoni, H. J. Choi, J. Ihm, S. G. Louie, A. Zettl, and P. L. McEuen, *Science* **288**, 494 (2000)
- [55] S. De, T. M. Higgins, P. E. Lyons, E. M. Doherty, P. N. Nirmalraj, W. J. Blau, J. J. Boland, J. N. Coleman, *ACS Nano* **3**, 1767 (2009).
- [56] D. Azulai, T. Belenkova, H. Gilon, Z. Barkay, G. Markovich, *Nano Lett.* **9**, 4246 (2009).
- [57] J. Y. Lee, S. T. Connor, Y. Cui, P. Peumans, *Nano Lett.* **8**, 689 (2008).
- [58] Z. Wang, J. F. Yuan, J. Zhang, R. B. Xing , D. H. Yan , Y. C. Han , *Adv. Mater.* **15**, 1009 (2003) .
- [59] L. Hu, H. S. Kim, J. Y. Lee, P. Peumans, and Y. Cui, *ACS nano* **4**, 2955–2963 (2010)

- [60] T. Tokuno, M. Nogi, M. Karakawa, J. Jiu, T. T. Nge, Y. Aso, and K. Suganuma, *Nano Research* **4**, 1215-1222 (2011).
- [61] Bovatsek J, Tamhankar A, Patel RS, Bulgakova NM, Bonse, *Thin Solid Films*, **518**, 2897-2904 (2010).
- [62] Fortunato E., Ginley D., Hosono H., Paine D.C., *MRS Bulletin*, **32**, 242-247 (2007).
- [63] Perkins J.D., Ginley D.S., Transparent conducting oxides for advanced photovoltaic applications, www.pv-tech.org
- [64] Lewis B. G., Paine D.C., *MRS Bulletin* **25**, 22-27 (2000)
- [65] R. Gordon, *MRS Bulletin* **32**, 52 (2000)
- [66] Hosono H., *J. Non-Cryst. Solids* **352**, 851-858 (2006)
- [67] Narushina S., Orita M., Hirano M., Hosono H., *Phys. Rev. B* **66**, 035203 (2002)
- [68] Hosono H. Kikuchini N., Ueda N., Kawazoe H., Shimidzu K., *Appl. Phys. Lett.* **67**, 2663-2665 (1995)

Chapter 2

Al-doped ZnO

Over the past years, Aluminum-doped ZnO has gained widespread attention as TCO, due to its cheaper, abundant, and less toxic constituents compared to ITO, the dominant transparent conductive oxide material today. These features are fundamentals for large-scale applications of ZnO, especially as transparent electrode in solar cells.

Among a wide variety of thin film deposition methods of AZO films, radio-frequency magnetron sputtering (RFMS) is considered the most suitable one since it offers unique features, i.e, ease scaling to large areas, high material density, good film adhesion and low substrate temperature. In the undoped material (ZnO), the electrical and optical properties are completely controlled by intrinsic doping defects (oxygen vacancy and interstitial zinc), and a small amount of Al (2 wt% Al₂O₃) acts as extrinsic doping and enhance the electro-optical properties of this material.

In this chapter, a detailed, systematic study of the dependence of the electro-optical performance of AZO thin film, deposited by RFMS, on process parameters and post deposition treatments, such as thermal and ion implantation, is presented.

2.1 AZO deposited by RF magnetron sputtering

In the previous chapter, we dealt about the main physical properties of TCOs, the factors that mainly influence their behavior and the main needs required for applications to solar cells. Now we turn our attention to aluminium-doped zinc oxide (known as AZO), a material which is able to satisfy these requests.

Due to the polar nature of the ZnO, the electrical, optical and structural properties of AZO have a strong reciprocal influence. In stoichiometric ZnO, the electrons of the Zn $4s^2$ and O $2p^4$ levels are reorganized in Zn^{2+} ($4s^0$) and O^{2-} ($2p^6$) of the hexagonal wurtzite structure, Fig. 1, with the “ c ” axis of 0.5207 nm and “ $a=b$ ” axis of 0.326 nm [1,2]. This material has a direct optical band gap $E_g = 3.2-3.4$ eV, depending on several factors such as purity, structural quality and growth technique [1,2].

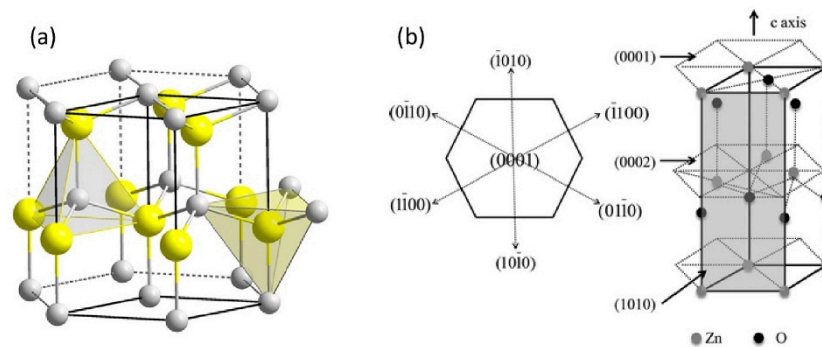


Figure 13: Wurtzite crystal structure with oxygen atoms (yellow) and zinc atoms (grey) (a). Orientations and associated directions of the wurtzite structure (b).

A process of substitutional doping with aluminium and/or intrinsic doping by oxygen vacancy and interstitial zinc is able to modify the properties of the material making it conductive as discussed in section 1.2.1. The presence of defects, such as Zn in interstitial positions or O vacancies,

produces shallow donor levels, which make the ZnO an n-type intrinsically doped semiconductor, with a free electrons concentration in the range of about 10^{17} - 10^{19} cm³. At the same time, the presence of Zn interstitial atoms produces an elongation of the c axis, i.e. a tensile strain along the (002) direction of the wurtzite crystal, which implies a strong charge displacement for a piezoelectric material such as ZnO. Extrinsic n-type doping of ZnO is often achieved by a few percent (1-3 %) of Al, so obtaining AZO. The Al in substitutional sites gives rise to Al³⁺, supplying 2 electrons to O (as in the case of ZnO) and 1 electron to the conduction band. AZO can achieve electron density of the order of 10^{21} cm⁻³. Further levels within the band gap are introduced by other kind of defects [1]. Moreover, due to the difference in the ionic radius between Zn²⁺ (0.060 nm) and Al³⁺ (0.039 nm), substitutional Al reduces the tensile strain along the c axis. Increasing the introduced aluminium percentage produces multiple effects that we have already mentioned in the previous sections 1.2.2 and 1.2.3. The increase of the free carriers concentration, above a certain value, causes a drastic reduction of mobility, due to enhancement of the scattering probability, besides the reduction of the transparency window, due to the shift of the plasma frequency at higher energies. Furthermore, an excessive concentration of dopant impurities leads to the creation of defect states within the band-gap that compromise the transparency even at the characteristic energies of the visible, approaching the material behaviour to the metal one.

The presence of intrinsic and extrinsic n-type dopants, and the consequent filling of the conduction band, not only affects the structural properties of the materials, but it also increases the optical band gap value, E_g^{opt} , due to the Burstein-Moss effect, see sections 1.2.3, and thus reduces the electrical resistivity. However, the B-M effect is strongly reduced by taking into account many body interactions. AZO electrical properties are also related to other effects which directly depends on the structural properties of the material, such as the scattering at the grain boundaries for polycrystalline films (as those grown by sputtering) and with ionized impurities (as Al³⁺) for doping level higher than 10^{20} cm⁻³. In these cases, the

carrier mobility is another critical parameter influencing the electrical resistivity.

Thermal processes are an efficient way to modify structural and electrical properties of AZO. In particular, a thermal annealing can strongly reduce the electrical resistivity of TCO films [3, 4], attributing this to several concurrent modifications: the size increasing of crystalline domains in polycrystalline thin films, the re-positioning of Al atoms into Zn substitutional sites, the release of the strain. For these reasons, thermal processes at around 250-300 °C are often mandatory for industrial applications of AZO as transparent electrodes. However, thermal budgets can be incompatible with the use of plastic or organic substrates and alternative routes must be considered. A wide variety of thin film deposition methods has been investigated in the past for the growth of undoped and doped ZnO: sol-gel process, spray pyrolysis, atomic layer deposition, pulsed-laser deposition, molecular beam epitaxy, electrochemical deposition, as well as chemical vapor deposition (CVD) such as atmospheric pressure-CVD (AP-CVD), low pressure-CVD (LP-CVD) and with plasma assistance (PE-CVD). Compared to these thin film deposition techniques, magnetron sputtering is characterized by the following advantages for the deposition of undoped and doped ZnO [1,2]:

- Scalability to large area
- Relatively cheap deposition method
- Good reliability and long-term stability of the process
- Very good thickness uniformity and high density of the film
- Low substrate temperatures (room temperature)
- Good adhesion of the film
- High deposition rates
- avoids the use of toxic gases
- ZnO has a high stability against hydrogen plasma

By considering sputtering, the Thornton-structure-zone model must be taken into account. Originally, this model made use of the dependence of two parameters, the substrate temperature and the sputter pressure, to

describe the growth of sputtered metals. Later Kluth et al. developed a modified Thornton-structure-zone model for the magnetron sputtering of ZnO:Al films from ceramic targets, see Fig 2 [5].

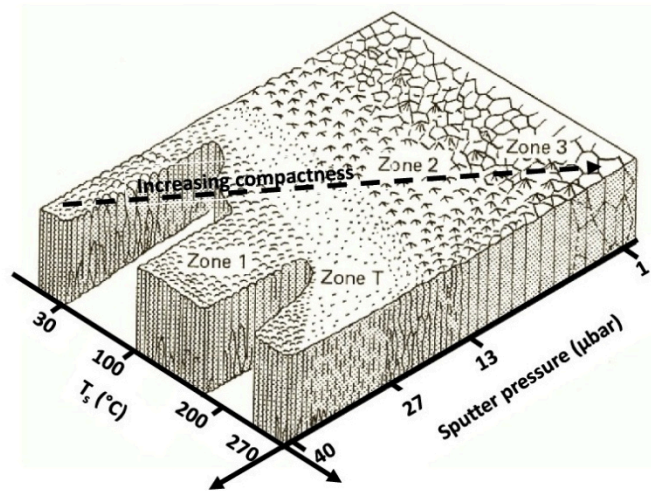


Figure 14: Modified Thornton-structure-zone model for the RF magnetron sputtering of ZnO:Al films, according to Kluth et al., describing the correlation between sputter pressure and substrate temperature.

Thornton proposed his model for magnetron sputtering of metallic films as a function of the argon pressure and the substrate temperature T/T_m , relative to the melting temperature T_m of the metal. On the other hand, Kluth et al. used the absolute value of the substrate temperature (T_s) and inverted the pressure and the temperature axis. This model, where the surface structure is classified in terms of four zones (Zone 1, 2, 3, and T) as a function of T_s and argon pressure, provides, by increasing the substrate temperature and reducing the sputter pressure, a more compact and denser film structure:

- Zone 1: Porous structure consisting of tapered crystallites separated by voids.

- Zone 2: Dense layer with small columnar grains from top to bottom.
- Zone 3: Grains coalesce to form larger, not necessarily columnar, grains.
- Zone T: Transition zone in which grain outlines are difficult to be identified.

The aim of this chapter is to propose a comprehensive study of sputtered AZO thin films on glass substrates, focusing on the understanding of the influence of sputtering process parameters and post deposition thermal treatment on the film properties. To this purpose, AZO thin film samples were deposited simultaneously on quartz substrates and SiO₂ grown onto silicon, through the RF-magnetron-sputtering technique, with an initial Argon pressure of 10⁻³ Pa. The choice of depositing the films on two different substrates was due to the different kind of characterization: quartz was used for optical, Rutherford Back-scattering Spectrometry (RBS) and electrical measurements, while SiO₂ for scanning electron microscopy (SEM) analysis. Substrates, before being placed in the deposition chamber, were cleaned with acetone and isopropyl alcohol. Inside the chamber, it was possible to place the substrates at two different distances (d) from the target. In particular, films grown on substrates placed at a major distance (7 cm) were subjected to heat treatments at 200 ° C for a 60 minutes after the deposition; while those placed at the minor distance from the target (4 cm), were grown at room temperatures or 200 ° C and 300 ° C during the deposition. All films are summarized in table 1. The samples, placed at 7 cm distance from the target, were synthesized by varying the sputtering power, used during the growth phase, leaving unchanged other parameters of working pressure and deposition time. The samples grown on the crucible were deposited keeping constant the sputtering power, the working pressure, the deposition time, and only varying the substrate temperature. In particular, for the latter types of films, it has been selected a RF power of 150 W, corresponding to the minimum value of resistivity among the AZO films grown as a function of the RF power.

Sample	Power [W]	d [cm]	Substrate temperature [°C]	Post annealing @ 200°C, 1h
AZO_50	50	7	RT	v
AZO_100	100	7	RT	v
AZO_150	150	7	RT	v
AZO_200	200	7	RT	v
AZO_250	250	7	RT	v
AZO_RT	150	4	RT	--
AZO_T200	150	4	200	--
AZO_T300	150	4	300	--

Table 3: AZO thin films grown under different conditions .

2.2 Material characterization

The effects on the AZO properties of the deposition parameters, such power applied to the target, substrate temperature, or post deposition treatment, are here presented and discussed.

2.2.1 Influence of RF power

The growth rate of sputtered AZO films as a function of the RF power for a given working pressure (pure Ar atmosphere at 1 Pa) and room temperature substrate is shown in figure 3. The growth rate is found to be directly proportional to the RF power. This can be explained by the enhancement of the ion flux and energy with increasing the RF power.

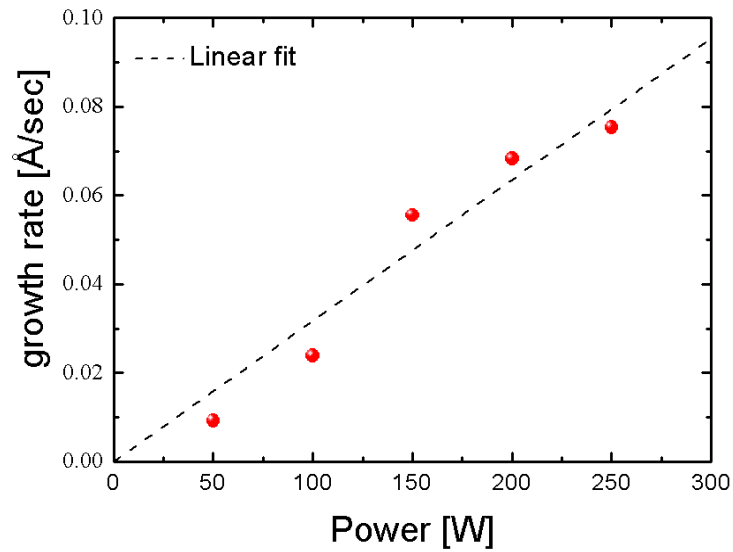


Figure 15: Growth rate versus RF power for a fixed Ar pressure of 1 Pa and room temperature substrate.

RBS analyses were used to determine the stoichiometry and the areal density of zinc (Zn), aluminium (Al) and oxygen (O) in the AZO layers. In particular, standard RBS analysis with 2 MeV He^+ beam in random configuration at 165° backscattering angle has been used. Figure 4 shows RBS spectra of AZO films deposited at RF powers from 50 to 250 W, on quartz substrate at room temperature, with a gas working pressure of 1 Pa. Depending on the thickness, signals arising from Zn (AZO), O (AZO and quartz) and Si (quartz) are well distinguishable from each other or not. The signal due to Al is not visible due to the small amount of this element and to the superposition with Si and O.

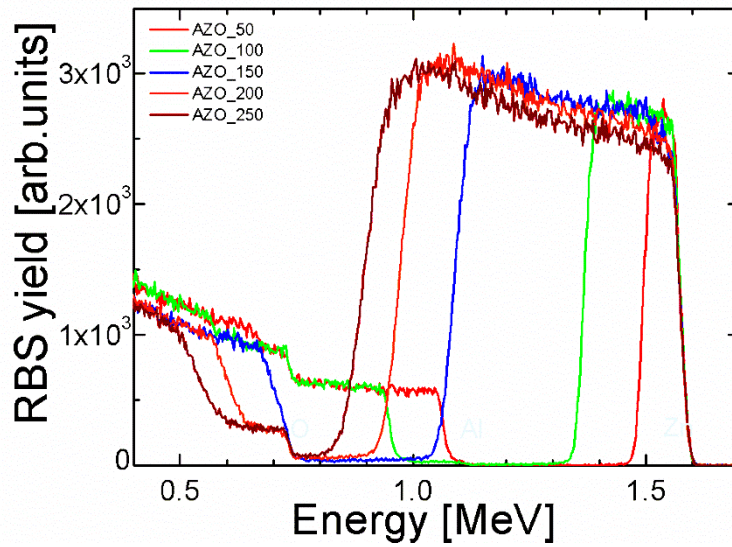


Figure 16: RBS spectra of the sputtered AZO thin film as a function of the RF power.

In particular, Fig 5 shows the experimental data of AZO_100 (red) and the corresponding simulated (blue) spectrum by *SimNRA* [6]. The signals related to the atoms of Zn, Al and O belonging to the film, as well as those related to Si and O in the substrate are indicated. The simulation, in excellent agreement with the experimental data, allows to obtain the stoichiometry of the sample. The same procedure was used for all samples. As discussed in detail in the Appendix, through position, height and width of the peaks in the energy spectra we can obtain quantitative information, such as chemical composition of the analysed thin films and the areal density, of each elements in the film. All RBS spectra, Fig. 4, were simulated by *SimNRA* software and the results are summarized in the Table 2. Within the experimental error, our samples show a stoichiometry compatible with the known composition of the AZO target (98% wt ZnO and 2% wt Al₂O₃).

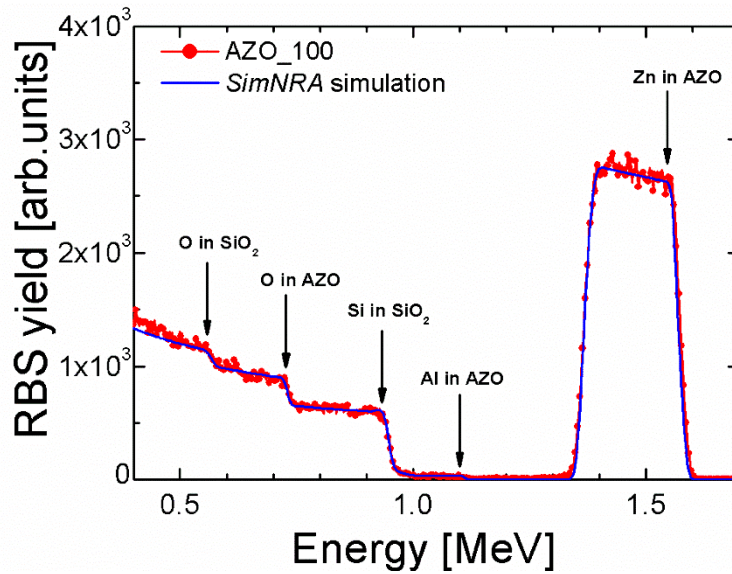


Figure 17: RBS spectrum of AZO_100 (dotted red line) and the corresponding computer simulation spectra by SimNRA (blu line).

Sample	Zn [%]	O [%]	Al [%]	Zn dose [10 ¹⁷ cm ⁻²]	O dose [10 ¹⁷ cm ⁻²]	Al dose [10 ¹⁷ cm ⁻²]
AZO_50	46	51	3	3,68	4,08	0,24
AZO_100	44	53	3	9,24	11,1	0,63
AZO_150	44	53	3	21,3	25,7	1,46
AZO_200	44	53	3	26,4	31,8	1,80
AZO_250	43	54	3	29,0	36,5	7,64

Table 4: Summary of the simulation results on analyzed samples. The percentage error measured on Zn is of 1%, while that measured on O and Al is of 5%.

Details about the structural properties are obtained by X-ray diffraction measurement performed by using a D8Discover Bruker-AXS diffractometer, equipped with a thin film attachment, with long soller slits and a CuK α source. The diffraction patterns were collected in a symmetric

configuration, with a Θ - 2Θ acquisition scheme. Figure 6 shows the XRD diffraction patterns of AZO films deposited at 50 (a), 150 (b) and 250 W (c), respectively, with the reference data for wurtzite ZnO standard powder in the diffraction angle (2Θ) in the range 24° - 60° using $\text{Cu}_{K\alpha}$ source ($\lambda=1.540562$ Å). Comparing this reference peaks with the experimental peaks of AZO films, it can be seen that they fit very well the ZnO reference data showing different phases in the film as a function of the sputtering power. Only a strong peak (002) is observed at 2Θ value of $\sim 34.4^\circ$ for the sample deposited at 150 W, showing a well oriented film preferentially grown along the c -axis (perpendicular to the substrate surface) with a wurtzite structure. While the appearance of the (100), (101) and (110) peaks, both at higher and lower sputtering power, indicate a degradation of the preferred orientation of the crystallinity. Therefore, the observed increasing in (002) peak intensity along with the disappearance of the other peak reveals that the sputtering powers of 150 W improves the crystallinity of the films. The crystalline domain size can be estimated using the Scherrer formula:

$$D = 0.9 \frac{\lambda}{W \cos \theta} \quad (1)$$

where λ is the X-ray wavelength, W is the full width at half maximum (FWHM) of the peak in radians, and Θ is the peak position in degrees. This formula gives a grain size increasing from 7 nm to 19 nm for rf power ranging from 50 to 250 W.

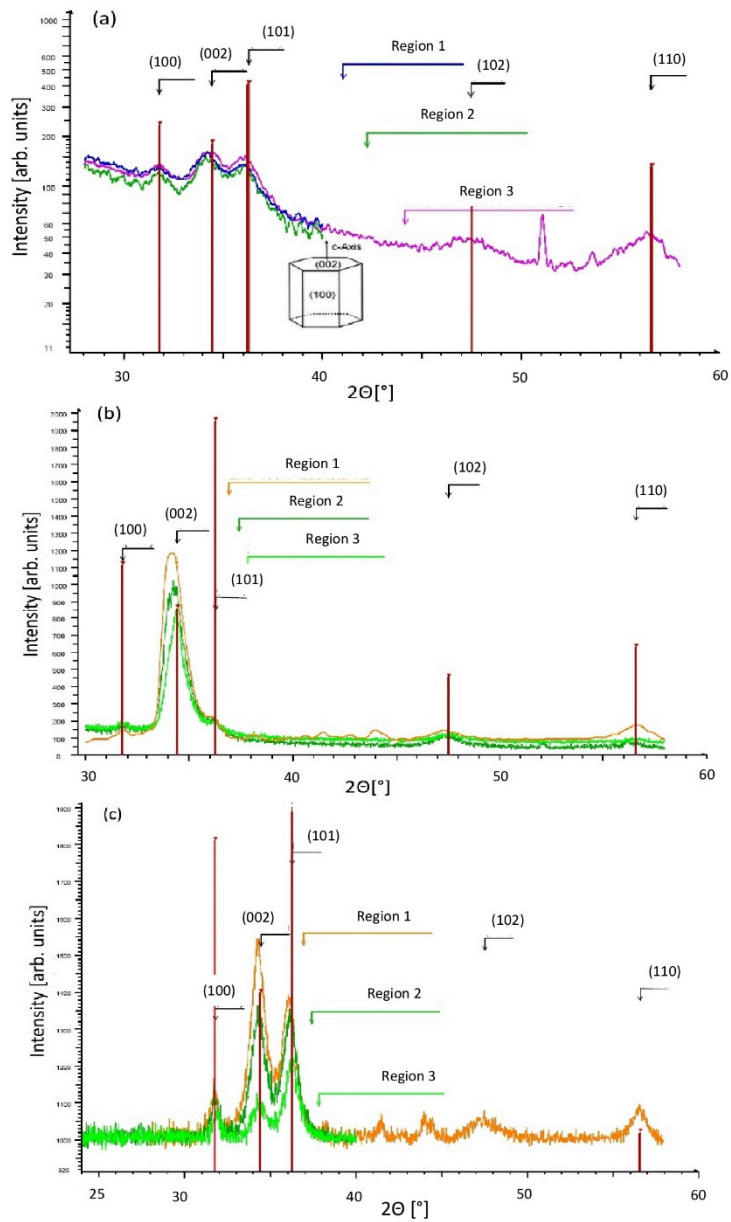


Figure 18: XRD pattern of AZO films deposited at room temperature and various RF power: 50 W (a), 150 W (b), and 250 W (c). The XRD patterns are acquired in three different regions of the sample and the reference data for wurtzite ZnO standard powder is reported too.

To the purpose of an accurate electrical and optical characterization, an exact knowledge of the samples thickness and surface morphology are fundamental to estimate the performance of the film. Therefore, scanning electron microscopy (SEM) of AZO thin films were taken to evaluate the surface and cross-section morphology of the samples. Figure 7 shows SEM images of the AZO films previously analyzed by RBS. As can be clearly seen, the surface morphologies vary significantly for AZO films grown at different RF power. We observe symmetric granular structure at low power (50 and 100 W), less symmetric granular structure at intermediate power (150 W), and, finally, fully asymmetric granular structure at higher power (200 and 250 W). By increasing the RF power, the grain size increases from ~30nm to ~120 nm and the surface of the films seems to become more rough. At 50 W, tiny packed grains and a relatively smooth surface is obtained, while at higher power, 250 W, the film exhibits a textured surface consisting of a dense array of large grains with distinct grain boundaries separated by voids. Furthermore, there are also remarkable structural differences among the films in cross-section. We can notice the transition from poor defined columnar structure, in the case of AZO_50, to a well defined columnar structure, AZO_100, AZO_150 and AZO_200, and, finally, to almost complete loss of the columnar structure. These columnar structures confirm the XRD analysis and the polycrystalline nature of the thin-films grew preferentially along the c-axis. By increasing the RF power, we deposit films of different thickness. It increases monotonically from 110 nm to 290, 668, 820 and 905 nm, for a RF power moving from 50 W to 100, 150, 200, and 250 W, respectively. It should be noted that the grain size determined by SEM are much larger than those previously determined by XRD, which indicate that AZO grains visible by SEM are not single-crystalline but consist of many crystallites.

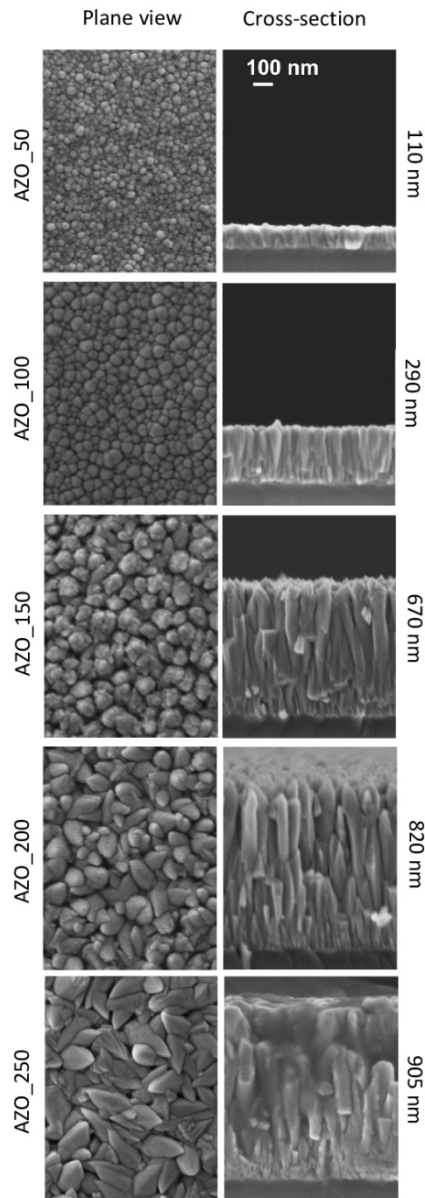


Figure 19: SEM images, in plane view (above) and cross-section (below), of the AZO_50, AZO_100, AZO_150, AZO_200, and AZO_250 film deposited with sputtering power of 50, 100, 150, 200, and 250 W, respectively.

Figure 8 shows the resistivity of the grown AZO films, measured at room temperature, as a function of the RF power.

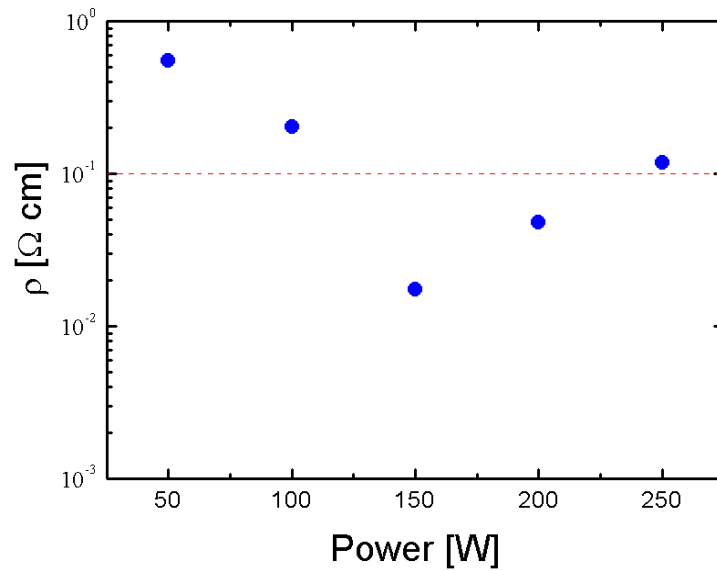


Figure 20: AZO film resistivity versus RF power

We observe that the resistivity of the AZO films initially decreases with increasing the power, reaching a minimum value at 150 W, after which it increases again. This behaviour of the resistivity as a function of the RF power is in agreement with the literature [7]. The red dashed line in the figure is used to identify the resistivity value of $10^{-1} \text{ } \Omega \text{ cm}$, below which AZO is compatible with industrial applications. The lowest resistivity of $10^{-2} \text{ } \Omega \text{ cm}$ is achieved for the film deposited with 150 W. In addition, the sheet resistance, carrier density and electron mobility, in the range 80-300 K have been investigated, Fig.9. These quantities are almost temperature-independent confirming that the film is a degenerate semiconductor [1]. AZO_150 sample, with a thickness of 680 nm, shows an electron concentration of about $2 \times 10^{20} \text{ cm}^{-3}$.

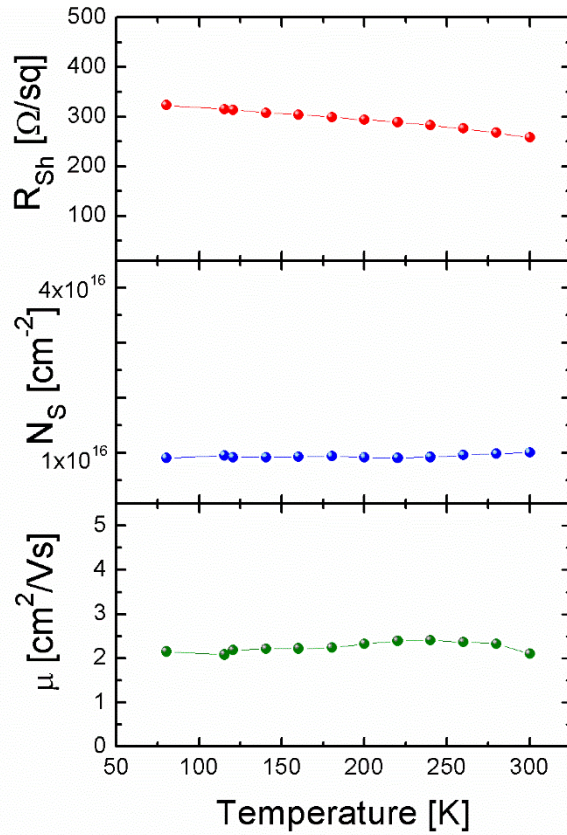


Figure 21: Sheet resistance, electron density and electron mobility as a function of the temperature measurement for AZO_150 film.

Finally, the transmittance and reflectance spectra have been measured on this set of samples by using a Varian Cary 500 double scanning UV-VIS-NIR spectrophotometer in the wavelength range 200-2000 nm, as described in the Appendix. In particular, we define an average visible transmittance, T_{vis} , by considering the average value of the transmittance in the visible range (400-800 nm). The absorption coefficient spectra have been obtained by combining the measured transmittance and reflectance spectra

[8], while the optical band-gaps were evaluated by using the Tauc's model [9], see Appendix. In Figure 10, T (a) and R (b) spectra are plotted as a function of the incident wavelength, together with the transmittance of the quartz substrate ($T_Q \sim 93\%$), shown for comparison. The presence of AZO films induces a decrease of T spectra in the UV-VIS-NIR region with respect to quartz substrate, and interference fringes with deep valleys and tall crests (thin film interference phenomenon) in the VIS range for all the investigated samples. All AZO films have an average transmission, T_{vis} , of over 75 % in the visible range and show a transmittance cut off at approximately 360 nm.

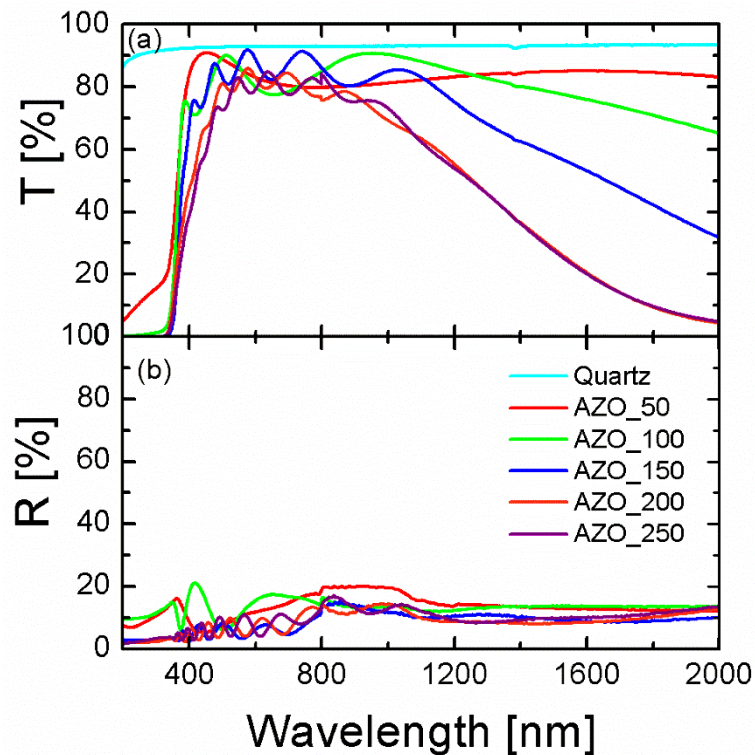


Figure 22: Transmission (a) and reflection (b) spectra of AZO films deposited at room temperature substrate, $P_w = 1$ Pa and different sputtering power of 50, 100, 150, 200, 250 W. The transmission of the bare substrate is also reported for comparison.

The RF power has a strong influence on T and R. Above 1000 nm, the general trend is that the transmittance decreases with increasing RF power, this dependence very likely simply originates from the increasing of the thickness. At low power of 50 W, an high optical transmission (above ~80 %) and low reflectance (below ~20 %) are observed, while a power of 250 W reduces the transmission to values very close to ~10 % above 1800 nm leaving the reflectance almost unchanged. These reflectance values, along with very different transmittances, suggest that the reducing may be attributed to an increasing absorption due to free-carriers, and not only to thickness. Below 1000 nm, the best T_{vis} ~85 % is obtained for a sputtering power of 150 W, whereas T_{vis} drops to ~84 % and 82%, for 50 and 100 W respectively, and to ~77 % and ~75% for 200 and 250 W, respectively. The gradual decrease of the transmittance in the visible range can be explained by the increasing of the film thickness [10].

The cut-off behaviour in the near ultraviolet of the spectrum is determined by direct electronic transitions from valence to conduction band. In a direct band gap semiconductor like AZO layer, the direct optical band-gap, E_g^{opt} , can be determined by the theoretical Tauc relation, see Appendix:

$$(E\alpha)^2 = B^2 (E - E_g^{opt}) \quad (2)$$

where B is the Tauc coefficient and E the incident photon energy. If the Tauc law properly describes the light absorption for AZO thin films, $(\alpha E)^2$ versus E should give a linear trend in the energy range for which $\alpha > 1 \times 10^4 \text{ cm}^{-1}$, E_g^{opt} is derived by the linear extrapolation to $\alpha E = 0$. Figure 11(a) shows the Tauc plot for AZO_150 that has a $E_g^{opt} = 3.5 \text{ eV}$, while the variation of the direct band gap of samples with the RF power used for their deposition is shown in Figure 11 (b). We can observe that the band-gap energy of AZO films increases from 3.41 to 3.61 by increasing the RF power. These values are higher than the ones reported in literature for ZnO [1,2].

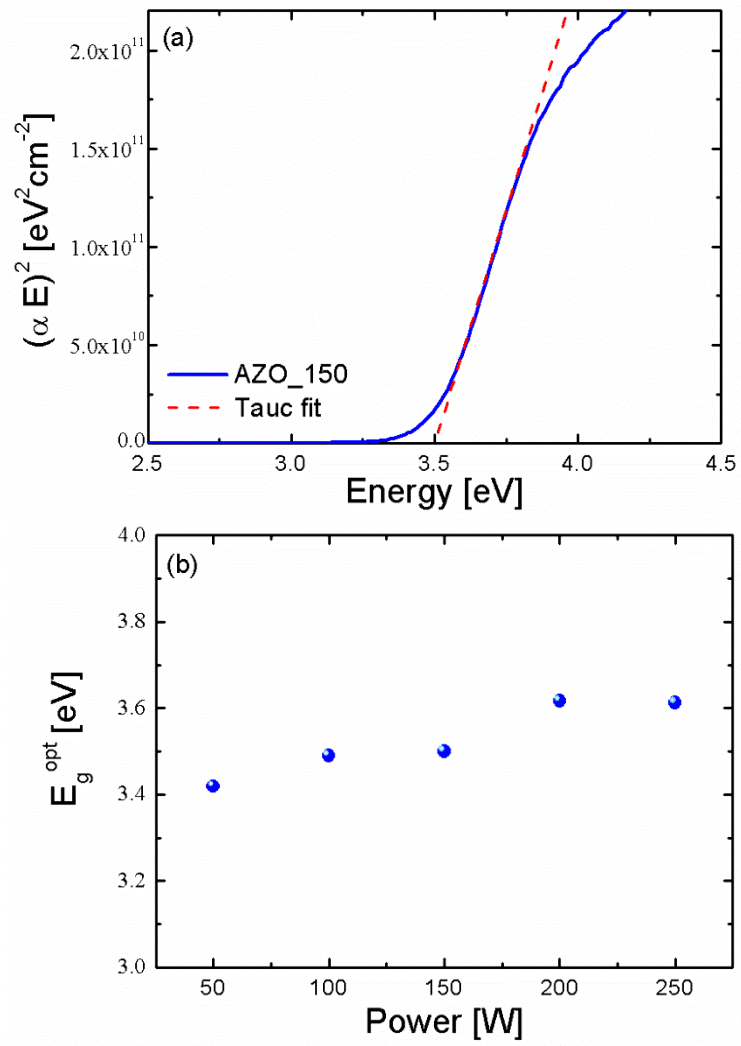


Figure 23: Tauc plot of AZO_150 layer (a), band-gap energy as a function of RF power

2.2.2 Effects of post deposition thermal treatment

In this section, we report the effects of post-deposition annealing, performed at 200°C in pure N₂ atmosphere for 1 hour, on the structural, optical and electrical properties of AZO samples. The elemental composition of the films after thermal annealing was determined by RBS analysis and SIMNRA simulation of the experimental data, as previously explained. By comparing the RBS spectra of two AZO samples before and after annealing, Fig 12, we observed an overlapping that clearly indicated that no modification of the structures occurs during thermal treatment up to 200 °C.

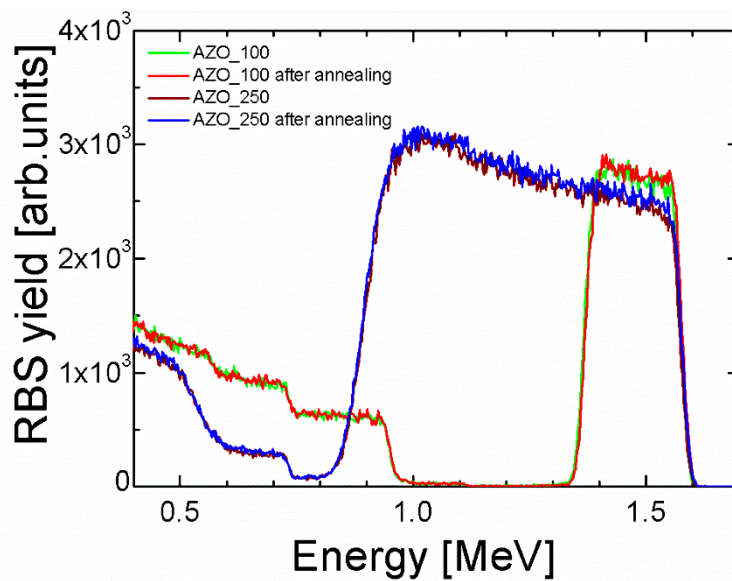


Figure 24: Energy spectra of He backscattered by AZO_250 and AZO_100 samples as deposited and after annealing at 200 °C, 60 min.

As far as the surface morphology is concerned, the SEM analysis show no significant changes, see Fig.13 for AZO_250, before and after thermal treatment at 200°C for 60 min.

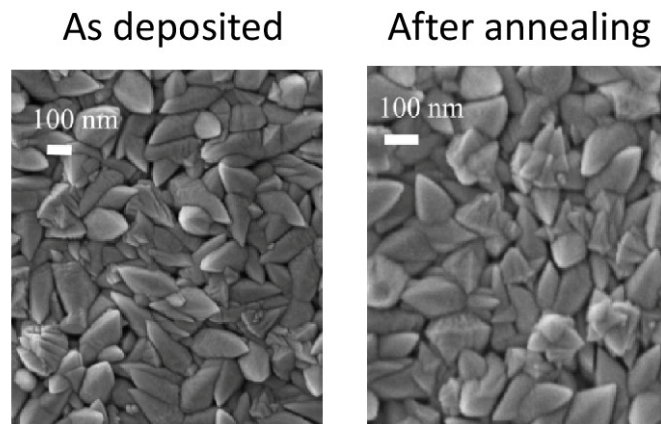


Figure 25: Plane view SEM images of AZO_250 films as deposited and after annealing at 200 °C, 60 min

The electrical properties of the AZO_150 film measured, as a function of temperature in the range 70-300 K, after thermal annealing are quite close to the data measured before the annealing process, Fig. 14. This indicates that a temperature of 200 °C was not enough to promote material crystallization, increase the grain size (as confirmed by SEM analysis), reduce point defects and/or dislocation density, and activate more Al dopant atoms. In literature, high quality TCO single layers are obtained by annealing at temperature higher than 200°C [11]. However, it is important to emphasize that the commonly thermal treatments performed at high temperature to obtain high transparent and conductive TCO, are incompatible with thermoplastic polymers because they cannot reach these temperatures without strong deterioration. This is one of the major impediments towards implementing TCO thin film on plastic substrates.

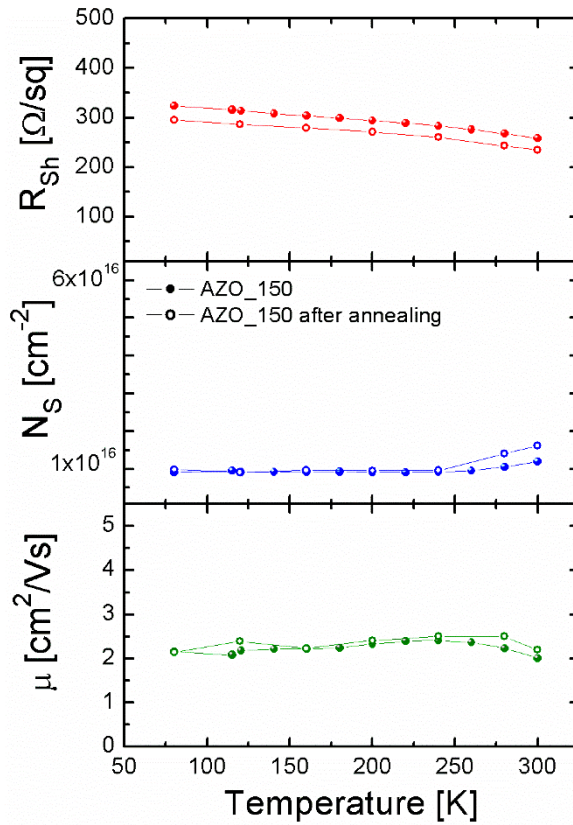


Figure 26: Sheet resistance, sheet electron density and electron mobility as a function of the temperature measurement for AZO_150 film as deposited and after annealing at 200 °C, 60 min.

In addition, the optical transmittance and reflectance in the 200–2000 nm wavelength range of all annealed AZO layers show the same trend of the as deposited ones. Despite of the similar trend, all films exhibit an increase of the transmittance in the near infrared range, an unchanged transmittance in the visible range and a decrease of the optical band gap after the annealing step. As an example, Fig. 15, is reported the optical transmission spectra of AZO_150 before and after thermal treatment.

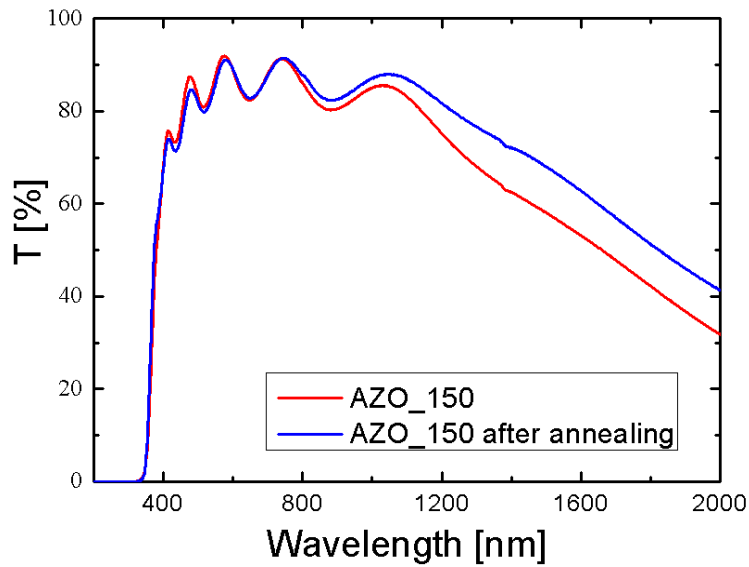


Figure 27: Transmittance spectra of AZO_150 film before and after annealing at 200 °C, 60 min.

The average transmission in the visible range, T_{vis} , of the sample before and after annealing are summarized in the table 3. These values are almost unchanged.

Sample	Before annealing	After annealing
	T_{vis} [%]	T_{vis} [%]
AZO_50	84	84
AZO_100	82	83
AZO_150	85	84
AZO_200	77	77
AZO_250	77	72

Table 5: average transmission in the visible range of the samples before and after annealing at 200 °C, 60 min.

Finally, after the annealing we measured a decrease in the optical band gap, from 3.50 eV to 3.48 eV for AZO_100 film, see Fig. 16, and from 3.42,

3.50, 3.62, 3.61 to 3.38, 3.47, 3.57, 3.58 eV for AZO_50, AZO_150, AZO_200, and AZO_250, respectively.

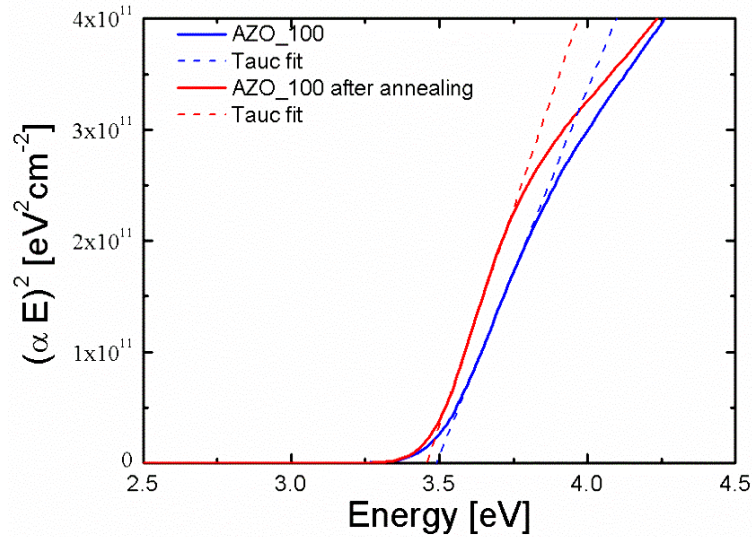


Figure 28: Tauc fit of AZO_100 before and after annealing at 200 °C, 60 min.

These observed band-gap shift are in agreement with the increase of the transmittance in the infrared region.

2.2.3 Influence of the substrate temperature

According to the Thornton-structure-zone model, the substrate temperature is an important processes parameter. AZO thin films have been deposited at various substrate temperatures (RT, 200 and 300 °C) at 1 Pa pure Ar atmosphere, with a RF power applied to the target of 150 W, for a deposition time of 20 minutes. The distance between target and substrate was 4 cm. As for the previous samples, RBS analysis have been performed in

order to check the chemical composition too. Once again, it was found an unchanged stoichiometry with respect to the as-deposited and annealed AZO.

Vice versa, the substrate temperature have a strong influence on the morphology of the films, as we can clearly see, Fig 17, from the plane view and cross-section SEM images. The film deposited at room temperature (AZO_RT), has a rough surface with clearly visible grain boundaries, while, when the substrate temperature raises to 300 °C (AZO_T300), the surface becomes smooth with larger grains tightly packed without voids. The reason for this behaviour is that the atoms at the surface of the growing AZO layer are more energetic and mobile, so the coalescence is enhanced resulting in smoother surfaces and larger grains.

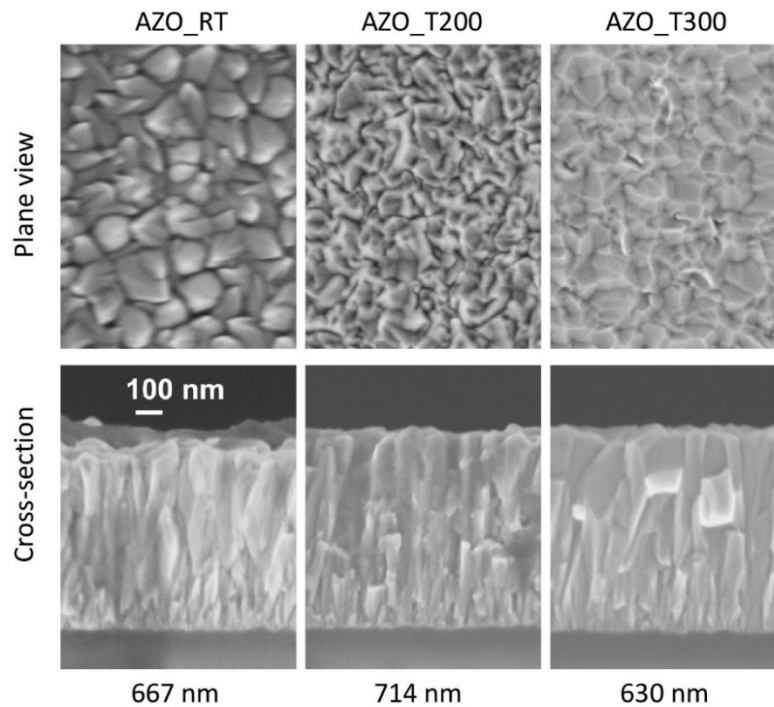


Figure 29: SEM images, in plane view and cross-section, of AZO film deposited at 150 W, $d = 4$ cm and $P_w = 1$ Pa, with different substrate temperature RT, 200 and 300 ° respectively for AZO_RT, AZO_T200 and AZO_T300

Again according to the Thornton-structure-zone model, the increase of the grain size (without voids) with the substrate temperature is accompanied with an increase of the lateral dimension of the columns. As we can see from cross section images, the AZO films go from defined columnar structure at room temperature deposition, to a complete loss of the columnar structure at 300 °C. It should be noted that the grain shape of AZO_RT is different from that observed in AZO_150, such discrepancy due to the smaller target-substrate distance as well as to the substrate temperature of the sample. As far as the thickness is concerned, values of 667, 714 and 630 nm in correspondence to substrate temperature of RT, 200 °C and 300 °C, respectively, were found.

The electrical properties of the AZO thin films as functions of the temperature for the three different substrate temperatures are shown in Figure 18. A clear degradation of the electrical properties can be observed for the sample deposited up to 300°C. Moving from RT to 300 °C substrate temperature, the decreased carrier concentration, from $8 \times 10^{15} \text{cm}^{-2}$ to $2 \times 10^{15} \text{cm}^{-2}$, combined with a decrease in the mobility, from $2.5 \text{ cm}^2/\text{Vs}$ to $4.5 \text{ cm}^2/\text{Vs}$ at 300 °C, results in an increase of the sheet resistance from $\sim 150 \text{ } \Omega/\text{sq}$ to $\sim 750 \text{ } \Omega/\text{sq}$. As already seen by SEM images, also from the point of view of the electrical properties, AZO_RT and AZO_150 are different, probably due to the shorter distance between target and substrate. In particular, a slightly decrease on the sheet resistance was observed due to the enhancement of the electron mobility, twice with respect to the AZO_150. Depending on the substrate temperature, different trends are observed on the evolution of the sheet resistances as a function of the temperature during the Hall effect measurements. In particular, although AZO_T300 shows almost constant values of carrier concentration and mobility over all the probe temperature range, its sheet resistance, measured at 320 K, strongly decreases to a value about half of the sample measured at 80 K. Once again, the carrier concentrations are temperature-independent, meaning these films are degenerate semiconductors.

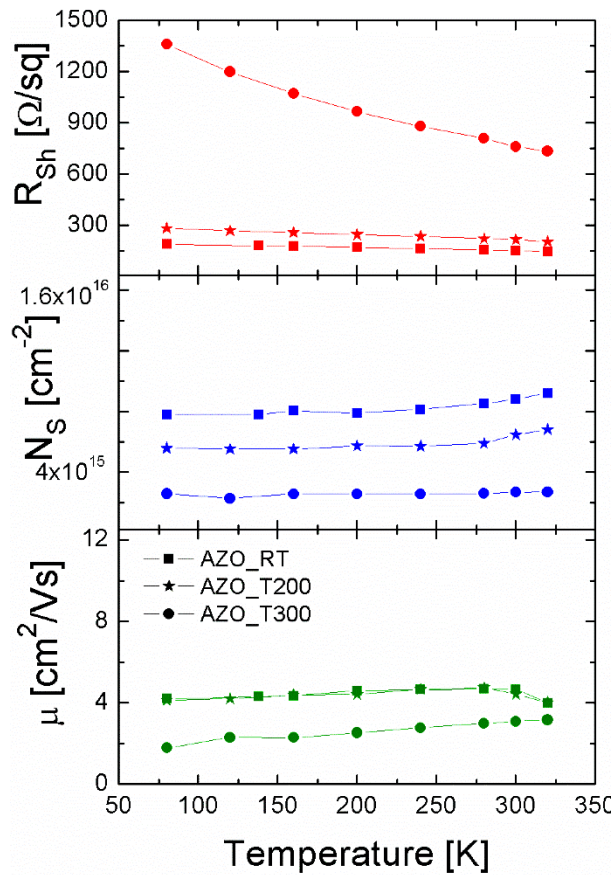


Figure 30: Evolution of sheet resistance, sheet electron density and electron mobility as a function of the temperature measurement of AZO_RT, AZO_T200 and AZO_T300.

In Fig. 19 transmission spectra of the samples deposited at different substrate temperatures are plotted as a function of the incident wavelength, together with the transmittance of the quartz substrate and AZO_150 for comparison. The substrate temperature has a strong impact on the optical properties. In particular, it has a strong impact on the transmittance at long (IR) and short (UV) wavelengths, and no impact in the visible range. The latter point was confirmed by the average transmittance of the samples,

which have the same value (within the experimental error): 84 % for the as-deposited AZO_150 layer and 83 %, 82 %, and 82 % after the deposition at substrate temperature respectively of RT (4cm), 200 and 300 °C.

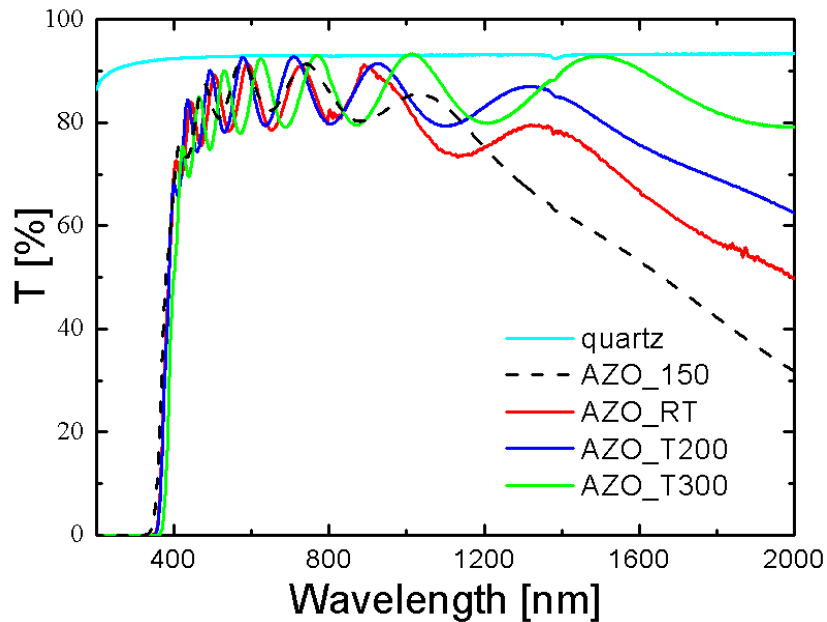


Figure 31: Transmission spectra of the AZO_RT, AZO_T20 and AZO_T300. The transmission spectra of the bare quartz substrate and AZO_150 are also reported for comparison.

As far as the infrared region is concerned, the transmission strongly increases when moving from room temperature (AZO_RT) to 300°C (AZO_T300). This behaviour can be explained in terms of plasma frequency. By increasing the substrate temperature, a reduction of the free carrier concentration has been observed, Fig. 18, and thus also a shift of the plasma frequency to lower values (the IR cut-off wavelength shift to higher values). Moreover, samples grown at higher temperature show a significant variation of the UV cut-off wavelengths, which moves to higher values. Such a red-shift, taking into account the Burstein Moss effect and the reduction of the carrier

concentration, suggests a reduction of the band-gap energy, which is confirmed by Tauc analysis as reported in Fig. 20.

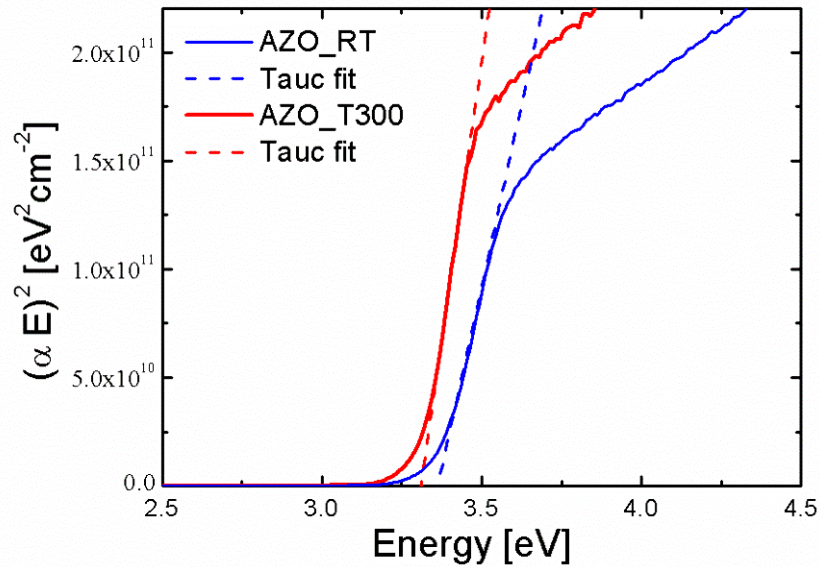


Figure 32: Tauc fit of AZO_RT and AZO_T300

The observed band-gap shift is of 3.38 to 3.32_eV, for the samples AZO_RT and AZO_T300, respectively. The decreasing of the band-gap for higher temperature is consistent with the fact that the carrier density decrease and the IR cut-off wavelength moves to higher value. AZO thin films grown at high temperature have lower performances than those deposited at room temperature (Fig. 18 and Fig. 19). These results clearly show how the substrate temperature in a critical deposition parameter that, in these circumstances, penalizes the performances of the AZO films.

2.3 Ion Implantation

Several studies have been reported in literature on the use of energetic electron or ion beams as an efficient way for material modification and improvement; structural, optical and electrical properties of thin films and surfaces, in fact, strongly experience the release of energy during electron and ion irradiations [12-16]. The possibility of controlled modification without thermal budgets makes the use of ion beams a critical issue in the field of TCOs. So far, scientific papers published on the ion beam modification of TCO based on ZnO mainly focused on the effect of light and heavy ion irradiation at very high energy on electro-optical properties [12-19]. Ion implantation has been also tested as a doping technique, especially for p-type, which seems to be an impassable limit for ZnO.

In this paragraph, we report a study of the modifications of structural, optical and electrical properties for 60 nm AZO polycrystalline thin films grown by RF sputtering after ion beam irradiation and/or thermal annealings. We used Ar^+ and O^+ projectiles at different energies and doses to study the effect of a beam passing through the AZO film or implanted within it. A strong decrease of the resistivity of samples upon irradiation with passing 350 keV O^+ ions or Implanted 30 keV Ar^+ , along with modification of strain, optical band-gap and crystalline grain size, was observed. On the contrary, despite of similar structural and optical properties, samples implanted with 30 keV O^+ (ion beam stopped within the AZO film) show a huge increases of the resistivity (above the measuring instrument limits). Annealing effects on the as deposited and O^+ irradiated samples are also reported for thermal processes up to 400°C.

2.3.1 O⁺ ion irradiation of AZO

AZO samples have been irradiated with O⁺ ions at 30 keV and 350 keV kinetic energy, scanning over an area of 1cm×1cm, at room temperature, normal incidence and at three different fluencies: 3×10^{15} , 1×10^{16} and 3×10^{16} cm⁻² (columns A and B of Table 4). At 350 KeV the O⁺ ions have a projected range, R_p, of ~700 nm, as calculated using SRIM simulations [20], so passing through the AZO films and stopping into the glass substrate. This condition was chosen to avoid O implantation within the AZO films. Vice versa, O implantation into the AZO films was achieved at 30 keV, with an R_p ~45 nm.

RBS analysis with He⁺ ion beam at 2.0 MeV was employed for a quantitative analysis of the Zn dose in the AZO films which, converted into thickness, confirmed a value of 60 ± 5 nm.

XRD analysis were performed in order to evaluate lattice structure, crystallographic domain size and strain of the AZO material before and after the ion irradiation processes. Fig. 21 displays the XRD spectra of various AZO samples, recorded in the Bragg-Brentano θ - 2θ configuration and normalized to the same arbitrary intensity. All samples exhibit only the (002) peak, which indicates a hexagonal wurtzite structure strongly texturized, with the *c*-axis along the growth direction. Two main features can be discussed for the (002) peak: the Full Width Half Maximun (FWHM) and the angular value θ of the maximum. The FWHM is related to the size *D* of the monocrystalline domains within the polycrystalline film by the Scherrer formula, Eq.1. A reduction of the FWHM indicates the increasing of *D* that is, in turn, an improvement of the crystalline quality of the film. The position of the peak is a measurement of the lattice parameter of the material.

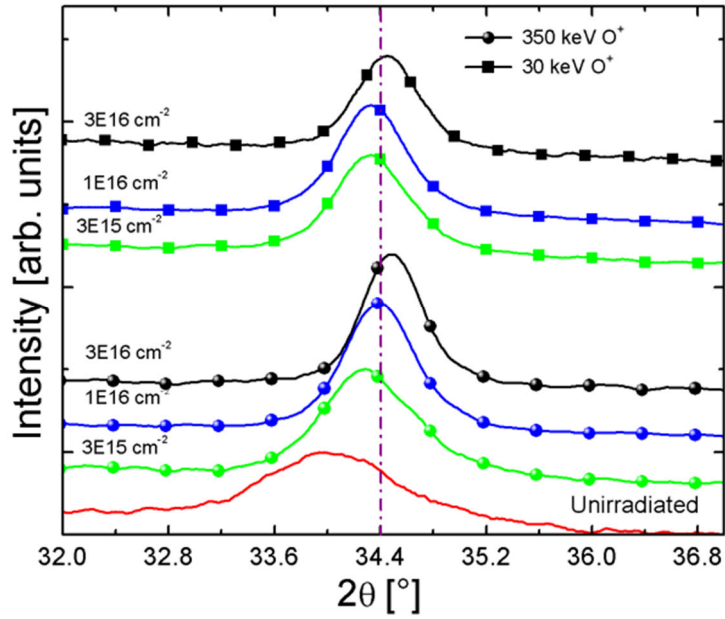


Figure 33: XRD spectra of AZO films before and after ion beam processes. The dashed-dot line at 34.42° is the reference for the (002) planes in bulk crystalline ZnO. Spectra intensities have been arbitrarily modified for an easier comparison.

The lattice constants can be calculated by the crystallographic plane distance, for indexes (hkl) , using [21]:

$$d_{hkl}^2 = \left(\frac{4(h^2 + k^2 + hk)}{3a^2} + \frac{l^2}{c^2} \right)^{-1} \quad (3)$$

In the simple case of the (002) peak, we end up with: $c=2d_{002}$ with d obtained from the Bragg formula $d = \lambda/2\sin\theta$. The film strain along the c axis is calculated as [22]:

$$\mathcal{E} = \frac{c_{film} - c_{bulk}}{c_{bulk}} \quad (4)$$

where c_{film} is obtained from XRD data and $c_{bulk} = 0.5207$ nm is the value for unstrained bulk ZnO [1]. Thus, from the (002) peak position we can measure the residual strain of the film along the c axis. The dashed line in Fig. 21 indicates the value of θ for a film with zero strain, while lower and higher θ values indicate tensile and compressive strains, respectively. XRD spectra show that the as deposited sample has the broader peak at the lowest θ value with respect to all the other AZO films. The contemporary angular shift and narrowing of the peaks after ion irradiation indicate an improvement of these samples with respect to the as deposited one, with a relief of the strain (θ shift) and an increasing of the crystalline domain size (peak narrowing). According to the eq. 1, 3 and 4, D and ϵ derived from the XRD measurements are listed in table 4 (columns C and E). In particular, XRD analyses show that all the implantation processes produce a relief of the strain (up to an inversion to slight compressive values at the highest doses) and an increase of the single crystalline domain size. At the lowest dose of 3×10^{15} cm⁻² the beam at 30 keV produces bigger variations with respect to the 350 keV one, while the effects on the structural parameters are more evident by increasing the ion fluence at the higher energy. These results indicates that the lattice damage expected upon ion irradiation is completely recovered by the local energy release during the collision cascades. In this regards, ion irradiation acts as a thermal annealing, as will be discussed in more details below.

Ion dose [cm ⁻²]	Ion Energy [keV]	Grain size D [nm]		Strain ϵ_c [%]		E_{gap} [eV]		Resistivity ρ [Ω cm]	
		C	D	E	F	G	H	I	L
A	B	RT	400°C	RT	400°C	RT	400°C	RT	400°C
0	0	7.3	11.1	1.17	-0.37	3.40	3.51	3.0	0.02
3×10^{15}	30	13.0	-	0.33	-	3.41	3.51	o.r	0.01
	350	10.4	-	0.48	-	3.44	3.48	7.0	0.01
1×10^{16}	30	14.1	-	0.33	-	3.40	3.47	o.r.	0.01
	350	13.6	14.6	0.17	-0.44	3.46	3.46	0.96	0.01
3×10^{16}	30	14.3	-	-0.02	-	3.45	3.56	o.r.	0.01
	350	16.6	16.6	-0.10	-0.56	3.48	3.49	0.02	0.01

Table 6: Crystalline grain size D , strain ϵ , optical energy gap E_{gap} and electrical resistivity ρ of all measured samples. Columns A and B gives the O^+ fluence and the ion beam energy respectively. Columns C, E, G, I, and D, F, H, L report the physical parameter measured before and after, respectively, a thermal process at 400 °C. For the resistivity in column I, the label o.r. means a value out of the range of the instrument (ρ was too high to be measured by our equipment).

Another consequence of the ion irradiation process concerns the surface morphology. Fig.22 reports the 3-dimensional AFM reconstructions of $1\mu\text{m} \times 1\mu\text{m}$ AZO surface regions irradiated with 350 keV O^+ . The root-mean-square (RMS) variation of the surface height profile obtained from the mean height [23, 24] are of ~ 3 nm in the as deposited, which increases to ~ 5 nm for lowest dose sample then decreasing to about 1.6 nm at higher doses.

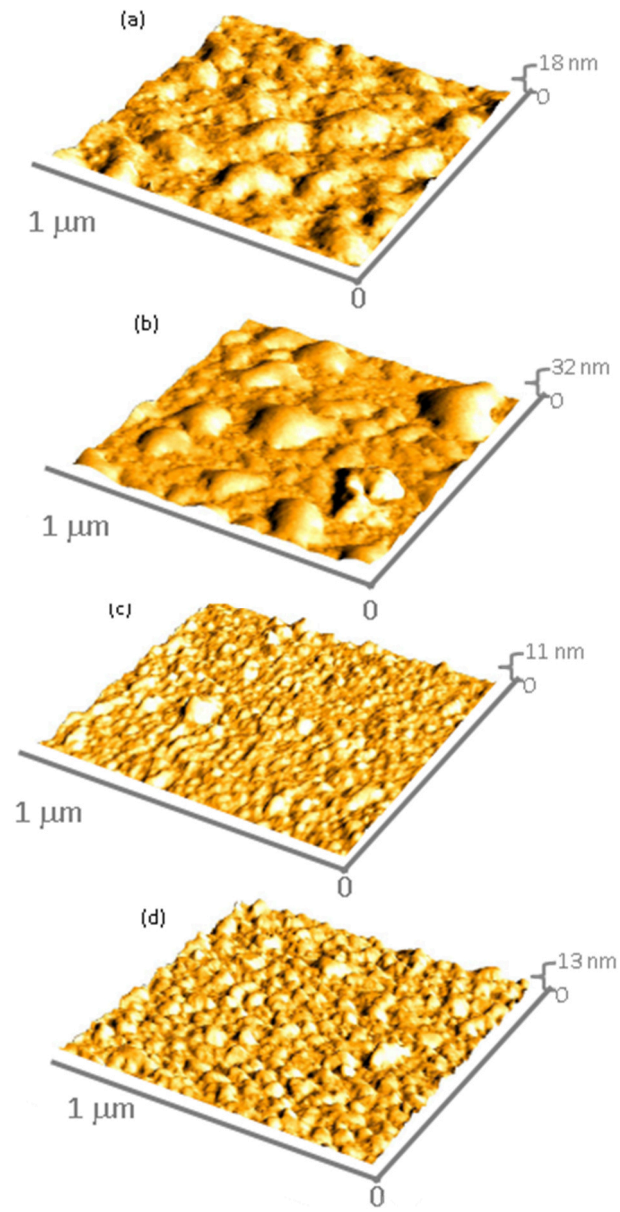


Figure 34: AFM images of the as deposited AZO film (a) and after irradiation at 350 keV beam energy with 3×10^{15} ions/cm² (b), 1×10^{16} ions/cm² (c) and 3×10^{16} ions/cm² (d).

This roughness is associated with an average height ranging from ~12 nm, at low ion fluence, and ~5 nm at higher ion fluence. It is then clear that ion irradiation at 350 keV, despite of an ion projected range of 700nm, is able to modify and to improve also the surface of the AZO films. The smoothing of the surface is another effect that makes this kind of ion beam processing an alternative way to improve the morphological and structural properties of AZO thin films.

The optical properties of samples were investigated by direct transmittance T , and specular reflectance R versus light wavelength. As an example, Fig 23(a) reports T and R for the as deposited AZO and films irradiated with 350 keV O^+ and 30 keV O^+ at the highest dose. No remarkable differences are observed but a small variation of the optical band gap E_{gap} arises when the Tauc analysis of these films is performed, Eq.2.

A blue-shift of the two irradiated samples of Fig. 23(a), with respect to the as deposited film, is visible in the Tauc plots of Fig. 23(b). Values measured for all samples are reported in the column G of Table 4. The unirradiated AZO film has $E_{gap} = 3.40$ eV, while a maximum value of 3.48 eV is observed in the case of the highest dose at the highest beam energy. The increase of E_{gap} is usually ascribed to the M-B effect, in turn related to a most efficient doping of the material and the consequent promotion of electrons into the conduction band [3]. Thus, being the presence of Al atoms in substitutional Zn sites the most effective way of extrinsic doping of AZO, an improvement of the structural parameters of the AZO films, as the one detected by XRD analyses for the implanted samples, agrees with the observed increasing of E_{gap} . This is also consistent with the strain relief due to the smaller ionic radius of Al^{3+} versus Zn^{2+} , as said in paragraph 2.1. However, the observed increases of the energy gap with the ion beam processes are quite small and not always directly related to the improvements of the electrical properties.

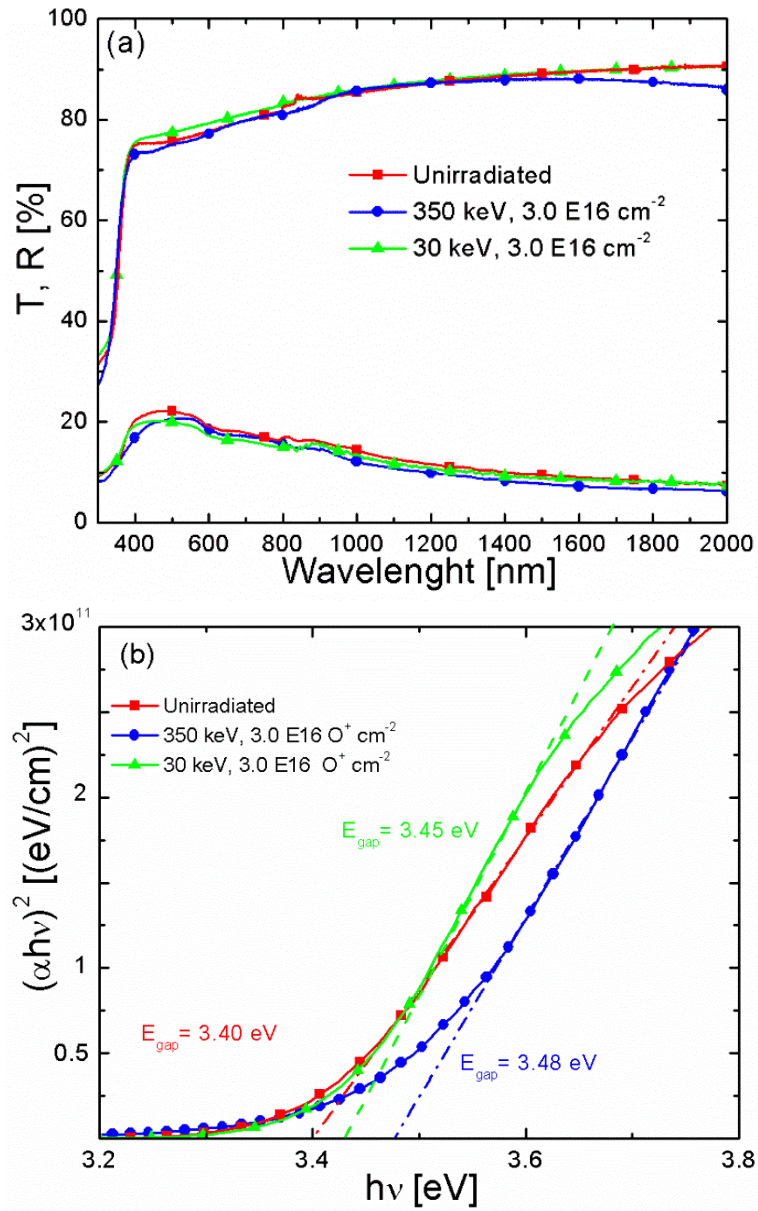


Figure 35: (a) Optical transmittance and reflectance spectra of three different AZO films: as deposited, after irradiation with $3 \times 10^{16} \text{ cm}^{-2}$ at 350 keV O^+ and 30 keV O^+ ion beam energies. (b) the Tauc plots of the same samples are reported and slight variations of the optical energy gap, calculated by the linear extrapolation to $(\alpha h\nu)^2 = 0$ (dash-dot lines), have been found.

Among the modifications induced by the ion irradiation, the most remarkable one concerns the electrical behavior. We found that the electrical resistivity, ρ , has a strong dependence on the ion beam parameters. Values of ρ are listed in the column I of Table 4 and graphically shown in Fig.24 (a), giving an impressive evidence of the effects of dose and energy of the ion beam on this parameter. In particular, a strong worsening for O^+ at 30 keV (corresponding ρ values are too high to be measured and out of scale), while, after a weak increasing at the lowest ion dose, a lowering down to 2 orders of magnitude is found for O^+ at 350 keV. In order to find any eventual direct relationship among electrical and structural properties, in Figs. 24(b) and 24(c) we plot the crystalline domain size and the strain, respectively, versus the ion dose. As already said, all the ion irradiation processes in our study improved the structural quality of the AZO films. Because of a lower scattering rate at the grain boundaries and Al in substitutional Zn sites, large grain size and low strain are reported in the literature as two of the major causes for improving the electrical properties of polycrystalline AZO films. In our case, however, the structural improvements observed after implantation of O^+ at 30 keV, Figs. 24(b) and 24(c), are accompanied by a detrimental increase of the resistivity, Fig. 24(a). The structural benefits due to ion irradiation, in this case, are completely suppressed by the presence of the O atoms implanted within the AZO film, with a huge worsening with respect to the as deposited material. As reported by many work in the literature [1, 17], thermal annealing of AZO is known to induce larger grain size, strain relief, energy gap increasing and resistivity decreasing. For this reason, we checked the effect of post deposition and post implantation thermal processes too. All the expected structural, optical and electrical improvements were observed in our samples, as reported in Table 4 in the columns D, F, H and L, relative to measurements done after a thermal annealing at 400 °C. By looking into details, we see that ion implantation is much more effective than thermal annealing to increase the grain size, being 7.3 nm the value in the as deposited AZO, 11.1 nm after 400 °C (without ion irradiation) and 16.6 nm after $3 \times 10^{16} \text{ cm}^{-2}$ at 350 keV (without annealing).

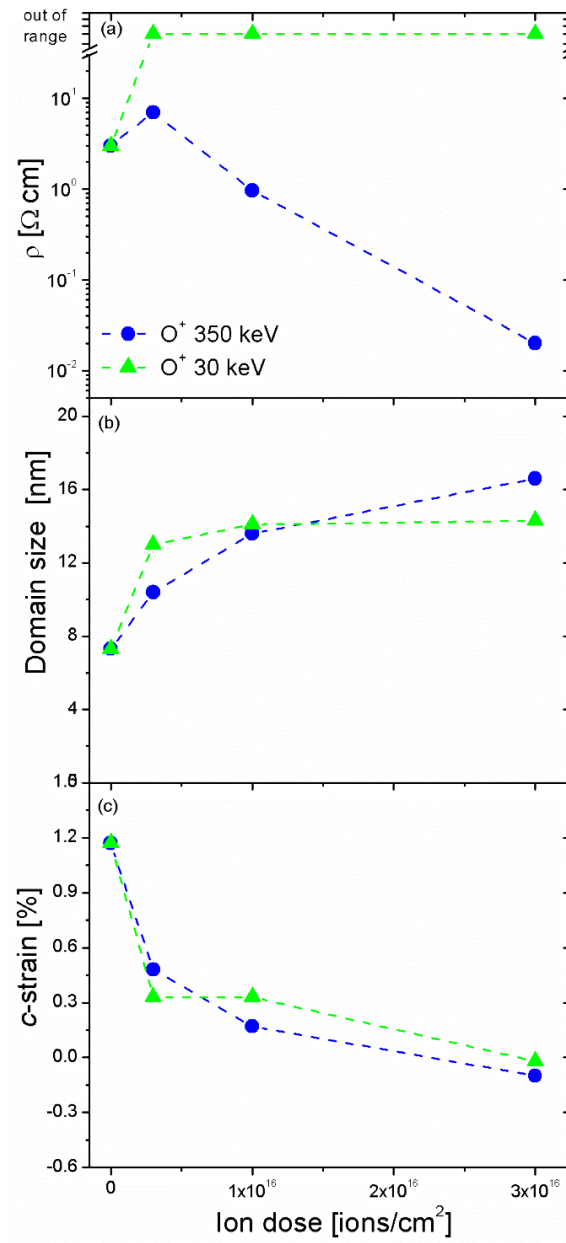


Figure 36: Electrical resistivity ρ (a), average size of the crystalline domains D (b) and film strain along the c axis (c), for our AZO samples as a function of O^+ ion dose irradiation for the two different energies of the beam.

We also notice that thermal annealing after the implantation does not produce any further increasing of this parameter. On the other hand, the strain is more sensitive to thermal than ion beam processes, as demonstrate by the strong variation from the value of +1.17% of the as deposited material to the -0.37% measured after 400 °C with respect to the -0,10% found after the heaviest ion beam irradiation. Moreover, thermal processes after ion beam irradiation, still modify the strain increasing it from -0.10% to -0.56 %. The great efficiency of the thermal energy in changing the strain, even after ion irradiation, could be attributed to the positioning of Al atoms into substitutional Zn sites, being Al³⁺ much smaller than Zn²⁺.

Small changes upon thermal annealing are observed also for the energy gap. In all cases the gap shows an increasing, in agreement with a more efficient electrical activation of the Al and the consequent population of the conduction band. However, if E_{gap} tends to increase with the ion beam energy and dose (column G of Table 4), after thermal annealing there is not a clear trend, although all the values are slightly increased with respect to the same samples before annealing. Finally, the electrical resistivity shows a strong lowering after thermal processes. In particular, for the unirradiated sample we find a continuous improvement with temperature, squares in Fig. 25, till the lowest value of 0.02 Ωcm at 400 °C (see also column L in table 4). It is worth of noting that this is the same value of resistivity obtained at room temperature after $3 \times 10^{16} \text{ cm}^{-2}$ at 350 keV ion irradiation. Also for the implanted samples the resistivity shows a clear reduction with thermal annealing, both for low and high beam energies. AZO implanted with $3 \times 10^{16} \text{ cm}^{-2}$ at 350 keV reaches a minimum of $\rho = 5 \times 10^{-3} \Omega \text{ cm}$ after 300 °C, to go to $1 \times 10^{-2} \Omega \text{ cm}$ at 400 °C. This identical value is obtained for all the implanted samples at 400 °C (column L in Table 4), independently of the ion beam processes. A different behavior is observed for the sample implanted at 30 keV for which Fig. 25 shows that only after a thermal process at 300 °C the resistivity fall down to measurable values, so recovering the worsening due to the O ion implantation. It is likely that the excess of O introduced in the AZO, with the effect of compensating the doping due to O vacancies and substitutional Al, is expelled from the surface during the thermal annealing

processes. This recall the behavior of AZO deposited in presence of high O_2 partial pressure [1] having high resistivity after the growth and requires thermal annealing to remove the O from the lattice and to lower the resistivity.

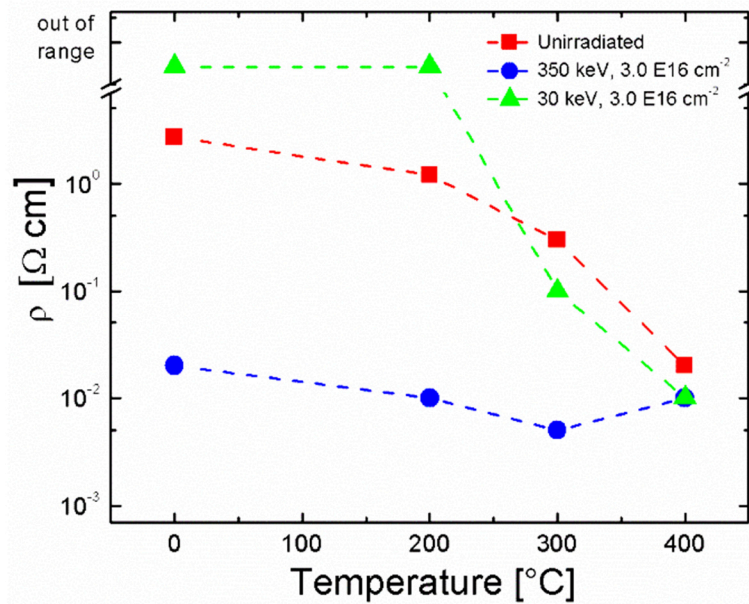


Figure 37: Electrical resistivity versus thermal annealing temperature of the as deposited AZO and two different groups of ion irradiated samples. In particular, the results for samples annealed after irradiation with 350 keV O^+ or 30 keV O^+ with a fluence of 3×10^{16} ions /cm² are reported.

2.3.2 Ar^+ ion implantation of AZO on polymer substrate

Based on this promising results, we have also investigated the 30 keV Ar^+ ion-beam-induced modifications of AZO thin films deposited on polyethylene naphthalate (PEN) substrate.

The experimental method is similar to that described previously but, in this case, the sample was irradiated at room temperature by 30 keV Ar^+ ions

at $3 \times 10^{16} \text{ cm}^{-2}$. This condition was chosen in order to avoid chemical interaction between the ions (Ar^+ is an inert gas) and the constituent elements of AZO, and to implant ions into the AZO films ($R_p \sim 25 \text{ nm}$) without compromising the quality of PEN substrate, which is sensitive to ion irradiation. For instance, in AZO films deposited on plastic substrate and then irradiated with passing O^+ ions at 350 keV kinetic energy with a fluence of $3 \times 10^{16} \text{ ions/cm}^2$, we observed a darkening of the polymer substrate indicating that the plastic substrate can be damaged.

The measurements performed on AZO layer grown on polymer substrate show that there are many similarities with the AZO deposited on glass substrate, discussed previously. Because the obtained experimental results showed that after ion irradiation a clear improvement of the structural quality, Fig. 26, with a growth of the polycrystalline grain size (14.1 nm) and strain release (-0.1 %) were achieved

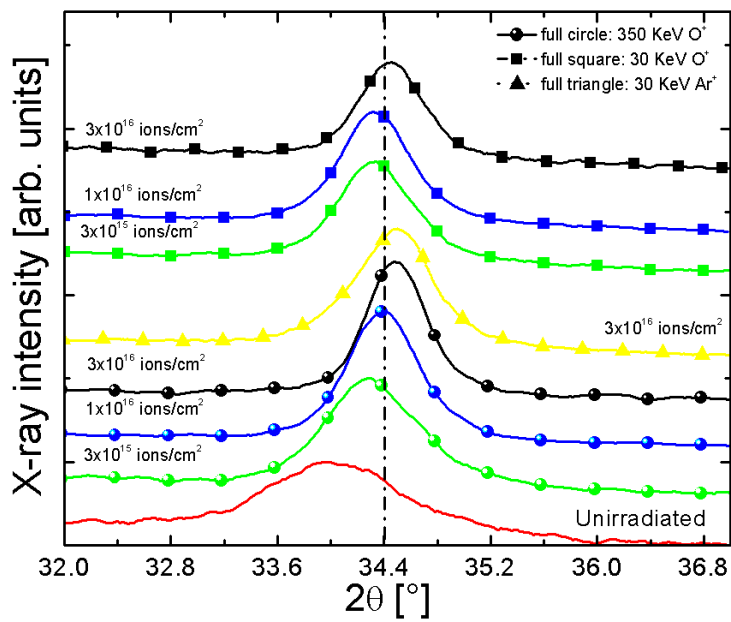


Figure 38: XRD spectra of AZO films before and after ion beam processes.

We found a high (~80%) and constant optical transmittance over the whole wavelength range (200-2000 nm) along with a shift of the optical absorption edge to higher wavelength indicating an increase in the optical band-gap up to 3.56 eV, Fig. 27.

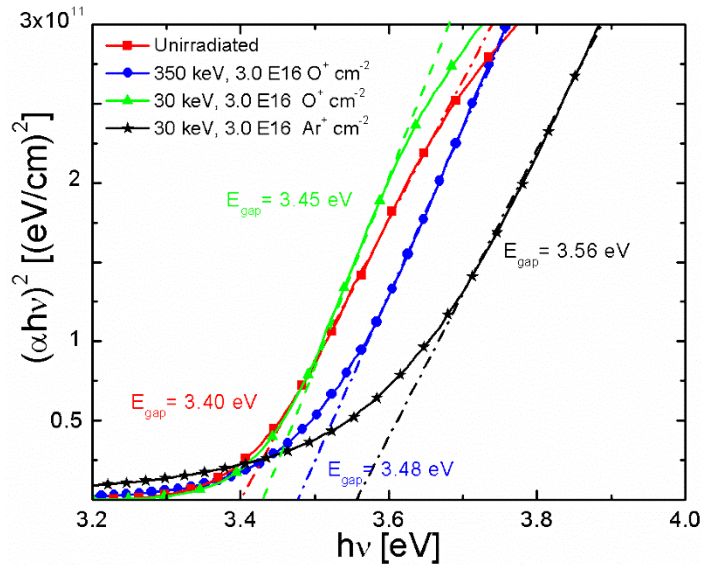


Figure 39: (b) Tauc plots of as deposited 60 nm AZO layer before and after irradiation with $3 \times 10^{16} \text{ cm}^{-2}$ at 350 keV O^+ , 30 keV O^+ and 30 keV Ar^+ ion beam energies.

We also found that the structural and optical improvements are accompanied by a strong decreases of the electrical resistivity, Fig. 28, more than two orders of magnitude, as already observed for 350 keV O^+ irradiation on quartz ($10^{-2} \Omega \text{ cm}$). These data show similar or even better structural, optical and electrical results than those observed after 400 °C thermal annealing of the as deposited AZO layer. Therefore, this technique can be considered a real good alternative to thermal processes to get highly quality AZO transparent electrodes deposited on plastic or organic substrates; since the latter cannot withstand the high temperatures required to make highly quality TCO.

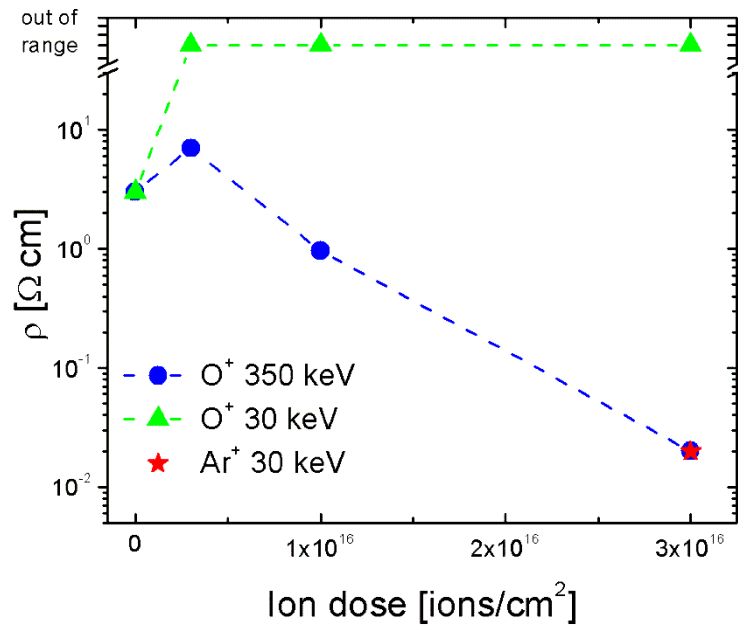


Figure 40: Electrical resistivity, ρ , of AZO samples as a function of ion dose irradiation for the two different ion type and energies of the beam.

2.4 Conclusions

In this chapter we presented a detailed experimental investigation on the synthesis, structural, optical and electrical analysis of Al-doped ZnO. In particular, we studied the role of sputtering parameters (RF sputtering power and substrate temperature) and post-deposition processes (thermal treatments and ion implantation) to optimize the opto-electronic properties of the AZO thin films. From the data reported and discussed in this chapter, the following conclusions can be drawn:

- Concerning the RF sputtering power, the lowest resistivity was reached at 150 W, thanks to a higher crystallinity quality, along with

the high transmittance in the visible range. While in the case of the substrate temperature, at a given RF power of 150W, a temperature of 300°C leads to the worst opto-electronic performance. The evolution of surface and cross section morphology as a function of these two parameters have been discussed, and they fit with the modified Thornton-structure-zone model. The influence of the post-deposition thermal treatment at 200°C was also studied, showing tiny opto-electrical improvements due to the temperature, not enough to promote a consistent material crystallization. Moreover, in all samples, the temperature independence of electron mobility and concentration confirms that our films are degenerate semiconductors. Due to the heavy doping, it is reasonable to assume that the smaller band-gap increase (compared to the only Burstein-Moss effect) is a net result of the competition between Burstein-Moss and many body effects.

- We investigated the modification of optical, electrical and structural properties of AZO thin films upon ion irradiation with 350 keV O⁺ and 30keV O⁺ or Ar⁺ ions at different doses, before and after thermal treatments up to 400°C. For all samples we report a clear improvement of the structural quality upon ion implantation, with a growth of the polycrystalline grain size and strain release. Very similar effects are shown after thermal annealing at 300-400 °C for the unimplanted AZO films, so demonstrating that ion irradiation, in this regards, acts as a thermal process. On the other hand, a peculiar behavior is found as far as the electrical properties are concerned. When O⁺ ions at 350 keV kinetic energy pass through the AZO film without stopping in it, or Ar⁺ ions at 30 keV kinetic energy stop in it, the structural improvement is accompanied by a strong decrease of the electrical resistivity, again with similar, even better, results observed after 400 °C thermal annealing on the as deposited sample. When the O⁺ beam is stopped inside the AZO film, at 30 keV implantation energy, the same structural improvements are not

associated to the electrical ones and, on the contrary, the AZO film becomes strongly electrically insulating. A thermal annealing at 300 °C is needed for these samples to show a decrease of the electrical resistivity, so recovering the detrimental effect of the ion implantation. These experimental evidences demonstrate how the electrical properties of AZO films are not simply related to their structural quality, as often trivially reported in the literature. Moreover, the role of oxygen is highlighted as the predominant one in the activation and deactivation of the doping levels, likely due to the compensation of O vacancies and/or formation of Al_2O_3 , both mechanisms subtracting donor levels for efficient AZO doping. High temperature thermal processes recover the electrical properties also in these samples probably because of surface thermal desorption of the shallow implanted O atoms. Finally, it is worth noting that ion irradiation with Ar^+ at 30 keV can be considered a real good alternative to thermal processes to get highly conductive AZO thin films, especially in the case of plastic or organic substrates that cannot be processed at high temperatures.

References

- [1] D. S. Ginley, H. Hosono, D.C. Paine, *Handbook of transparent conductors*, Springer 2011.
- [2] P. Barquinha, R. Martins, L. Pereira, E. Fortunato, *Transparent Oxide Electronic*, Wiley 2012
- [3] C. Guillen, J. Herrero, *Phys. Status Solidi A* **206**, 1531 (2009)
- [4] C. Guillen, J. Herrero, *Vacuum* **84**, 924 (2010)
- [5] O. Kluth, G. Schöpe, J. Hüpkes, C. Agashe, J. Müller and B. Rech, *Thin Solid Films* **442**, 80 (2003)
- [6] M. Mayer, *SIMNRA, a Simulation Program for the Analysis of NRA, RBS and ERDA*, Proceedings of the 15th International Conference on the Application of Accelerators in Research and Industry, J. L. Duggan and I.L. Morgan (eds.), American Institute of Physics Conference Proceedings 475, p. 541 (1999)
- [7] T. Minami, T. Miyata, T. Yamamoto, H. Toda, *J. Vac. Sci. Technol.* **A18**, 1584 (2000).
- [8] S. Mirabella, R. Agosta, G. Franzo, I. Crupi, M. Miritello, R. Lo Savio, M.A. Di Stefano, S. Di Marco, F. Simone, T. Terrasi, *J. Appl. Phys.* **106**, 103505 (2009)
- [9] J. Tauc, *In Amorphous and Liquid Semiconductor*, Plenum, New York 1974
- [10] W. J. Jeong, G.C. Park, *Sol. Ener. Mat. Sol. Cells* **65**, 37 (2001).
- [11] C. Guillén, J. Herrero, *Thin Solid Films* **520**,1 (2011).
- [12] Angadi B., Jung Y. S., Choi W. K., Kumar R., Jeong K., Shin S. W., Lee J. H., Song J. H., Khan M. W. and Srivastava J P , *Appl. Phys. Lett.* **88**, 142502 (2006)
- [13] Look D. C., Reynolds D. C., Hemsley J. W., Jones R. L. and Sizelove J R *Appl. Phys. Lett.* **75**, 811 (1999)
- [14] S. K. Neogi , S. Chattopadhyay , Aritra Banerjee , S. Bandyopadhyay, A. Sarkar and Ravi Kumar, *J. Phys: Condens Matter.* **23**, 205801 (2011)

- [15] Matsunami N., Fukushima J., Sataka M., Okayasu O., Sugai H., Kakiuchida H, *Nucl. Instr. Meth. Phys. Res. B* **268**, 3071 (2010)
- [16] Fukuoka O., Matsunami N., Tazawa M., Shimura T., Sataka M., Sugai H. and Okayasu O. *Nucl. Instru. Meth. Phys. Res. B* **250**, 295 (2006)
- [17] Sugai H, Matsunami N, Fukuoka O, Sataka M, Kato T, Okayasu O, Shimura T and Tazawa M., *Nucl. Instr. Meth. Phys. Res. B* **250**, 291 (2006)
- [18] Zang H., Wang Z.G., Peng X.P., Song Y., Liu C.B., Wei K.F., Zhang C.H., Yao C.F., Ma Y.Z., Zhou L.H., Sheng Y.B., Gou J., *Nucl. Instr. Meth. Phys. Res. B* **266**, 2863 (2008)
- [19] Matsunami N., Fukuoka O., Tazawa M., Sataka M. 2005 *Surface & Coatings Technology* **196**, 50 (2005)
- [20] J. F. Ziegler, J. P. Biersack, and U. Littmark, *The Stopping and Range of Ions in Solids, Topping and Ranges of Ions in Matter Vol. 1* (Pergamon, New York, 1984).
- [21] Min-Chul Jun and Jung-Hyuk Koh, *Nanoscale Res. Lett.* **7**, 294 (2012)
- [22] Cebulla R., Wendt R. and Ellmer K., *J. Appl. Phys.* **83**,1087 (1998)
- [23] Ruffino F., Grimaldi M.G., Giannazzo F., Roccaforte F., Raineri V. *Nanoscale Res Lett.* **4**, 262 (2009)
- [24] A-L. Barabasi, H.E. Stanley, *Fractal Concepts in Surface Growth* (Cambridge University Press, Cambridge, 1995)

Chapter 3

TCO/Ag/TCO ultra-thin multilayers

Among many transparent electrodes, TCO/metal/TCO structures can achieve optical and electrical performances comparable to single TCO layers and very thin metallic films.

Therefore, in this chapter we will initially investigate the synthesis and the structural, optical and electrical properties of AZO/Ag/AZO multilayer coatings. Thermal stability of the compositional, optical and electrical properties of the AZO/Ag/AZO structures are investigated up to 400 °C and as a function of Ag film thickness.

Then, we also report on thin multilayers based on Ag (fixed thickness), AZO and ITO with all combinations of the TCOs as top and bottom layers in order to analyze how the TCO deposition sequence and TCO nature can modify the electro-optical response of the whole multilayer structure. In particular, the structural, electrical and optical properties are studied to optimize the three-layer structure for very thin transparent electrodes suitable for photovoltaic applications.

3.1 Materials selection

To reduce the TCO thickness and, at the same time, to get the desired electrical conductivity while maintaining high transmittance, the inclusion of very thin metallic films within TCO material has recently received a renewed interest as a highly promising route in the framework of very thin devices [1,2], including solar cells. Earlier works reported that ITO/Ag/ITO can be used to surpass ITO for higher conductivity and lower cost [3-5]. S. Sutthana *et al.* used DC magnetron sputtering to synthesize AZO/Ag/AZO multilayers for applications in dye-sensitized solar cell [6]. Sahu *et al.* investigated the performances of structures with three to five alternating layers of AZO and Ag deposited in an e-beam evaporation system [7,8] and reported highest transmittance spectra in case of three layers. In order to meet the expectations for growing demand and lower production costs for photovoltaic and electronic applications, there is a need to develop alternative low-cost, high-quality, transparent electrodes with properties comparable to the conventional ITO [9–12]. TCO/metal/TCO structures represent the better alternative to ITO in terms of film preparation and electro-optical properties [13].

In the next two sub-paragraphs, we will investigate in more details the best options for the metal and TCOs selection to be used in transparent multilayered electrodes for very thin devices, including solar cells.

3.1.1 Silver as intralayer

The key role, in the overall opto-electronic properties of the TCO/metal/TCO structures, is played by the metal intralayer. Among many kinds of metals, Ag is the first choice because in thin film shows better optical characteristics than other metals with the same thickness on the UV-VIS-NIR wavelength range [14-18], and as bulk it has lower electrical resistivity compared to other metals (see table 1) [19].

Metal	Resistivity at 20°C [$\mu\Omega$ cm]
Ag	1.6
Cu	1.7
Au	2.4
Al	2.8
Mg	4.6
W	5.6
Mo	5.7
Zn	5.8
Ni	7.8
In	8.0
Pt	10.0
Pd	11.0

Table 1: Electrical resistivity values of several bulk metals

Therefore, the electrical and optical properties of silver make it the most common metal intralayer used in TCO/metal/TCO multilayer structures. Other metals such as Cu, Au, Al, Ni and Pd as well as Ag-based alloys, including Cu, Au and Pd, have also been utilized [20-25], however their optical and electrical properties were suitable for specific applications and in any case of low quality with respect to Ag based multilayer thin film.

In our experiments, silver thin film have been grown by RF-magnetron sputtering of Ag target (2 Pa Ar atmosphere, room temperature), onto fused silica or silicon substrates keep at 7 cm from the target. Different Ag thin films have been obtained by varying the applied power at the silver target, 20-200W, and deposition time, 15-180 sec. This systematic research was carried out to determine the best deposition parameters to optimize the structural properties and electrical resistivity of Ag thin film along with optical properties, essential for a practical use. Table 2 summarizes the characteristic of the synthesized samples.

Sample	Substrate	Power	Deposition time
		[Watt]	[sec]
Ag_1	Si	20	30
Ag_2	Si	20	60
Ag_3	Si	20	120
Ag_4	Fused silica	20	15
Ag_5	Fused silica	40	15
Ag_6	Fused silica	70	15
Ag_7	SiO ₂	50	180
Ag_8	SiO ₂	100	180
Ag_9	SiO ₂	150	180
Ag_10	SiO ₂	150	30
Ag_11	SiO ₂	200	30

Table 2: Deposition parameters of Ag silver films deposited by RF- magnetron sputtering on different substrates

Scanning electron microscopy analysis in plane and cross section view have been used to study the evolution of the surface morphology and to measure the thickness respectively. It is well known that the evolution of metal thin films such as Ag, Cu or Au deposited on glass or other materials (dielectric or not) strongly depends on the deposition technique as well as many parameters such as substrate type, vacuum condition, substrate temperature, metal, etc. In addition, the evolution of all metals from distinct island to a continuous film goes through a series of well defined stages of growth [26, 27]. By comparing the samples Ag_1, Ag_2, Ag_3, Fig.1, we can clearly observe, as a function of the deposition time, different stages of evolution from tiny metallic nuclei on the substrate observed after 30 s of deposition, passing through a “worm like” structure for 60 sec., to continuous film after 120 sec.

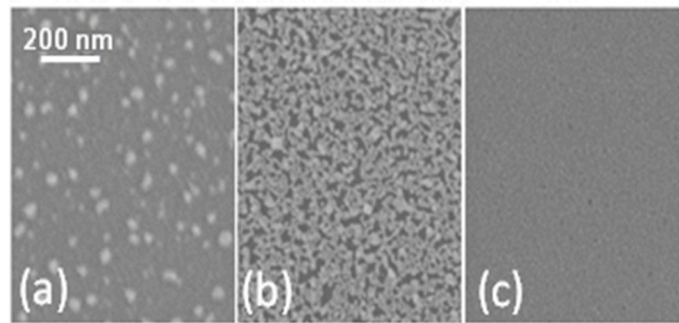


Figure 1: Plan- view SEM images of the samples (a) Ag_1, (b) Ag_2 and (c) Ag_3. Samemarker for all samples.

RBS analysis (2,0 MeV He⁺ beam, 165° backscattering angle) was also performed to quantify the dose of Ag. Then, the layer thickness has been derived by assuming the atomic density of 5.86×10^{22} Ag at./cm³. By means of RBS analysis we confirmed the thickness measured by SEM. The energy spectra of He⁺ elastically scattered at 165° are reported in Fig.2. The increasing area of the Ag signal corresponds to $14 \pm 1 \times 10^{15}$ atoms cm⁻² at 30 sec., $28 \pm 1 \times 10^{15}$ atoms cm⁻² at 30 sec. and $62 \pm 1 \times 10^{15}$ atoms cm⁻² at 120 s, i.e. to 2.5, 5 and 11 nm Ag film thickness respectively.

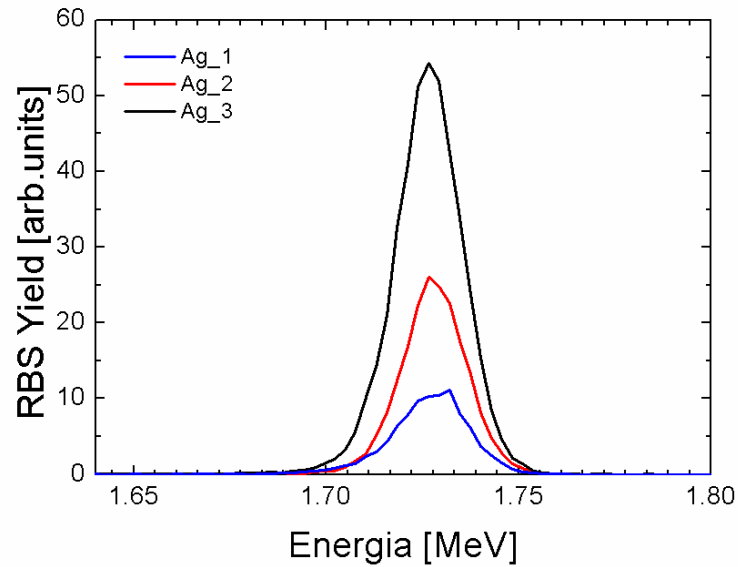


Figure.2: RBS spectra for Ag films deposited on silicon substrate.

The next step was to check the optical properties of our thin films as a function of the applied power to the target, while the other parameters were kept constant. These experiments were performed on samples deposited on fused silica: Ag_4, Ag_5, Ag_6. The optical properties in terms of transmittance and reflectance have been obtained in the range 300-800 nm by a Varian Cary 500 double scanning UV-VIS-NIR spectrophotometer. A critical requirement is that the Ag film must be sufficiently thin to be transparent in the visible range. As we can see from the transmittance and reflectance spectra of the three samples, reported in Fig.3, along with the spectrum of fused silica substrate for comparison, the progressive decrease in the transmittance is due to the increase in the reflectance.

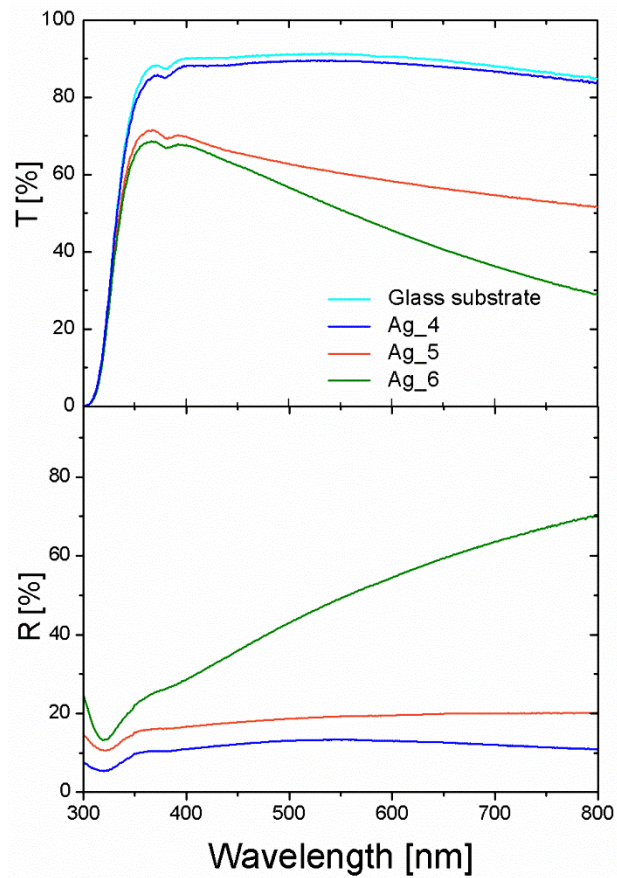


Figure 3: Optical transmittance and reflectance spectra of silver films deposited by magnetron sputtering on soda lime glass substrate. The bare soda lime glass substrate was also measured for comparison.

Finally, we investigated the properties of Ag films deposited by using powers higher than the previous ones: samples Ag_7 – Ag_11 . Plane view and cross sectional SEM analysis are displayed in Fig. 4. By using 50 W and long deposition time (180 s), this is the case of sample Ag_7, for which we observe a no porous film but with a high density of bubbles, Fig.4 (a). This suggested that the film is not well adherent to the substrate, as evident from the cross sectional SEM analysis shown in Fig.4 (b). While at higher power

and shorter deposition time (Ag_11) we deposited a more uniform film, Fig.4 (c), well adherent to the substrate (SiO₂ layer on Si) visible in Fig.4 (d).

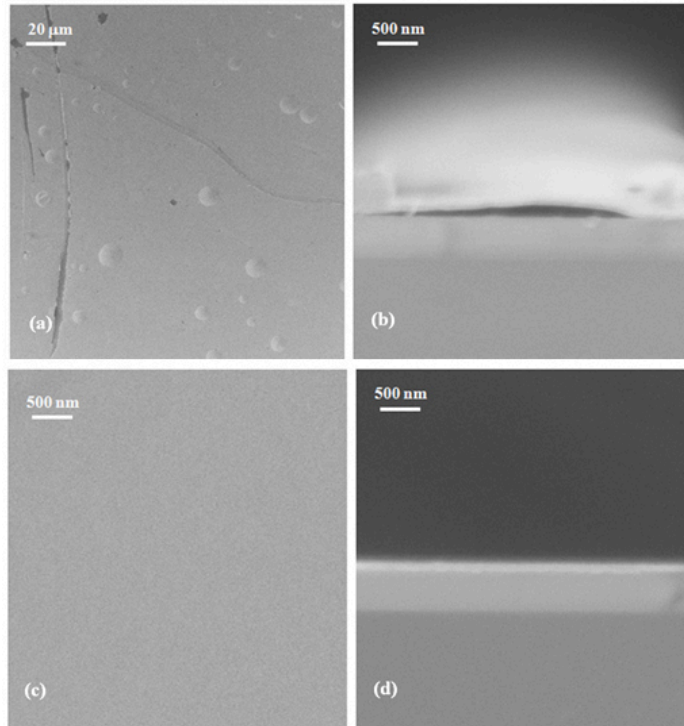


Figure.4: SEM images in plane view (a, c) and cross section (b, d) of Ag_7 and Ag_11 samples, respectively.

The Ag thicknesses, measured by RBS analysis, were of 67, 190, 241, 57 and 76 nm, for Ag_7, Ag_8, Ag_9, Ag_10, Ag_11, respectively. These thicknesses were confirmed by the cross sectional SEM analyses. In addition, reflectance measurements, Fig.5, showed a progressive reflectance enhancement by increasing the metal film thickness, up to values close to 100% in the visible range for Ag_9.

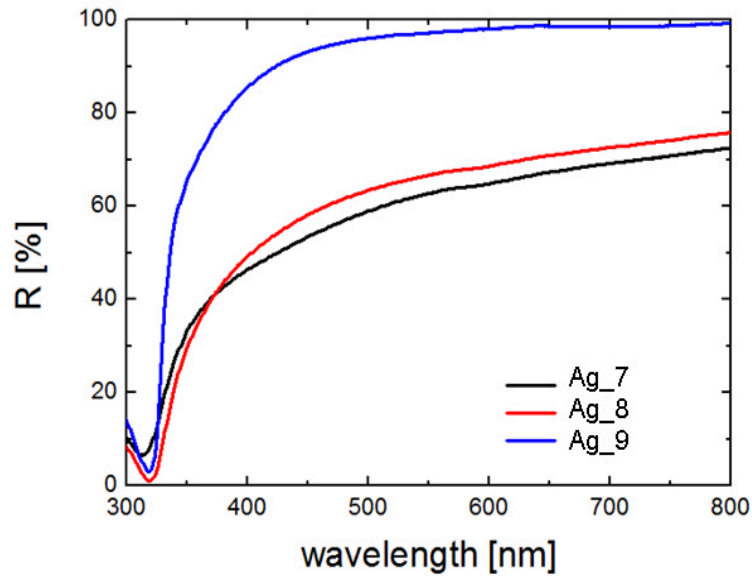


Figure 5: Reflectance spectra of Ag_7, Ag_8 and Ag_9 samples.

These results are useful to evaluate the effect of some deposition parameters on the properties of Ag thin film, but for practical applications, it is necessary to investigate the role of TCO thin films on the whole multilayer structure. To this aim, in the following sub-paragraph we will first investigate the properties of TCOs thin films.

3.1.2 Which TCO?

The TCO material in the TCO/metal/TCO structure plays two important roles:

- It protects the Ag thin layer, also avoiding detrimental interdiffusion within the active materials of the solar cells. It acts as an antireflective coating.

Due to their high free-electron density, of the order 10^{22} - 10^{23} cm^{-3} , metals are highly reflective in the visible spectral range; therefore the TCO, acting as antireflective coating on top of the metal, can drastically increase the transmittance. The goal is to obtain a maximum transmittance at some specific wavelengths, typically 550 nm [24], or to maximize the overall transmission in the visible range (400-800 nm) [25]. To this aim, TCO thickness needs to be properly selected to adjust the constructive and destructive interferences of the light waves at the different interfaces of the multilayer structure [28,29]. Many TCOs (ZnO, GZO, IZO, GIO) are used for TCO/metal/TCO fabrication [30-33]. In our study we decided to focus only on AZO and ITO since they are the mostly used in many technologies .

On chapter 2 we have already presented a detailed research activity on the dependence of the AZO electro-optical properties on the the growth parameters. Our best AZO thin film was grown by using a sputtering power of 150 W, a target-substrate distance of 7 cm, a working pressure of 2 Pa at room temperature. Now we present a detailed investigation for the optimization of ITO thin film.

Indium tin oxide thin films were deposited at room temperature on glass substrate by RF magnetron sputtering, using a commercially available ITO target (10 wt% SnO_2 -doped In_2O_3). The distance between the target and the substrate was 7 cm. The influence of sputtering power (100-250 W) and working pressure (0.4-1.4 Pa, argon atmosphere) were investigated in order to optimize the deposition conditions. A preliminary study on the dependence of the electrical and optical of ITO films on the working pressure showed the best properties at a value of 1 Pa, therefore this value was maintained fixed in all the depositions. Results on the electrical and optical performance of thin films, as a function of the deposition power are presented in Fig.6.

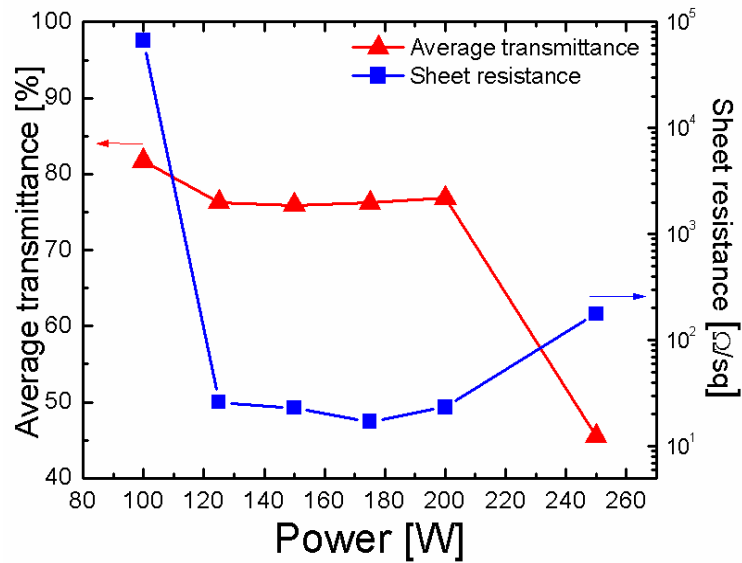


Figure 6: Dependence of average transmittance and sheet resistance of ITO thin on power.

The sheet resistance shows a minimum value of $9 \times 10^{-4} \Omega\text{cm}$ at 175 Watt. The optical transmittance was measured between 300-800 nm, and the average transmission in the visible part of the spectrum was calculated. No noticeable variations in the transmittance and sheet resistance have been observed in the samples deposited with power in the range of 125-200 W, while a very low value of about 45% and high value of about 81% were achieved for the transmittance at 250W and at 100 W, respectively. The ITO films fabricated with the previous sputter powers showed optical or electrical properties not suitable for their application as transparent electrodes. The physical properties of a thin film, especially a metal one, greatly depends on the substrate [34-37], therefore, before the investigation of TCO/Ag/TCO multilayers, we present the electrical and optical properties of Ag/AZO/glass structure.

Silver thin films were deposited, with the same experimental conditions reported in the previous sub-paragraph, onto ~900 nm thick AZO film, with a sheet resistance of $R_{\text{sh}}=19.03 \Omega/\text{sq}$. We have grown the three

samples presented in table 3 by using the same fused silica substrate and deposition time of 15 s.

Sample	Power [Watt]	R _{sh} [Ω /sq]
Ag_4/AZO	20	18.30
Ag_5/AZO	40	11.16
Ag_6/AZO	70	4.79

Table 3: Deposition parameters and sheet resistance of Ag silver films deposited by RF-magnetron sputtering on AZO film.

The transmittance and reflectance spectra of the three samples, together with the one measured on the bare AZO substrate are shown in Fig.7. First of all, we can see that in both spectra there are oscillations due to thin film interference for both transmission and reflection. The presence of the Ag_4 layer on the AZO surface resulted in a slight reduction of its optical transmittance and sheet resistance, while in the case of Ag_6, we observed a remarkable drop in both optical and electrical properties.

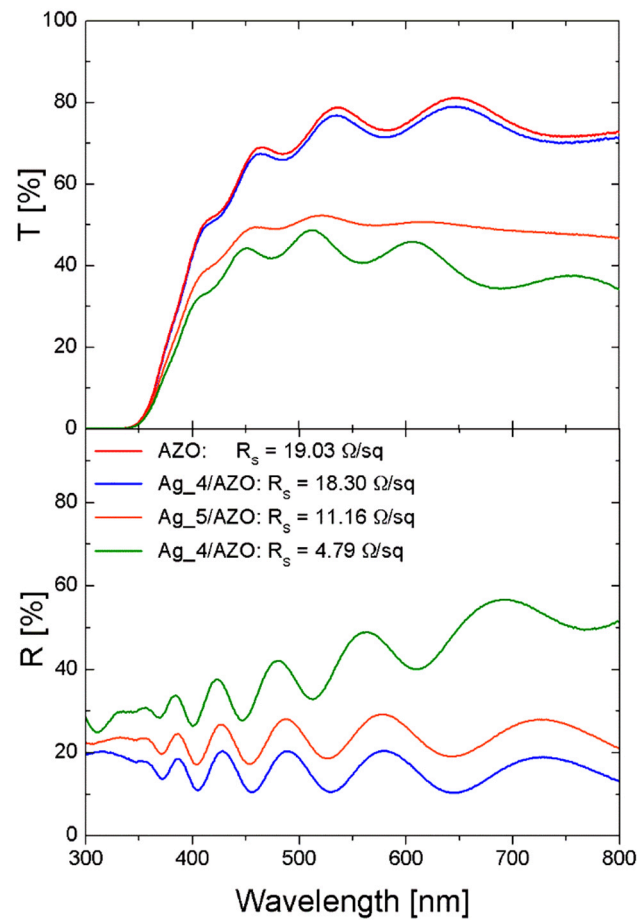


Figure 7: Optical transmittance (top) and reflectance (bottom) spectra of three different Ag silver films deposited by RF-magnetron sputtering on AZO film. The transmission of the bare AZO/glass stack substrate was also measured for comparison.

SEM analysis, acquired in plane view, were also employed to further characterize our dual-layer samples as well as the bare substrate. Fig.8 shows the comparison between the AZO film before and after the deposition of Ag₄ thin film. The most crucial requirement affecting the performance of the Ag/AZO/glass structure, is the structural uniformity of the metal film. As soon as the thickness of the Ag layer is beyond a critical threshold, too thin

or too thick, it begins to suffer of poor optical transmission or electrical conductivity, respectively.

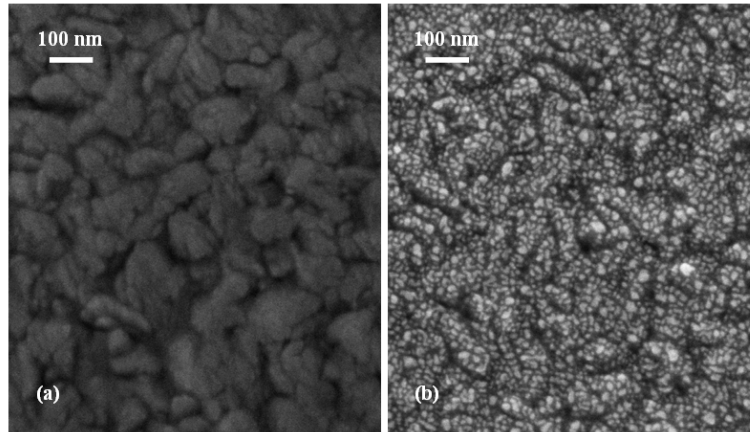


Figure 8: plane view SEM images of bare AZO substrate, (a), and Ag₄/AZO sample (b).

Therefore, it is very important to select the proper Ag thickness in order to find the right tradeoff between optical and electrical properties in the multilayered structures.

3.2 High performance AZO/Ag/AZO transparent electrode

Nowadays, among the most utilized TCO thin films in modern technologies, AZO has attracted much attention due to its good electrical properties with high optical transparency comparable to ITO. Moreover, AZO is abundant, non-toxic, easily fabricated at industrial scale and cheap, which are the reasons stimulating the research on In-free electrodes. Typically, the best electrical conductivity of AZO films is obtained when heating treatments are employed during or after the deposition process, which, unfortunately,

increases the overall cost of TCO layer fabrication. To reduce the TCO thickness and, at the same time, to get the desired electrical conductivity while maintaining high transmittance, we investigate the inclusion of very thin Ag film within AZO material. For this reason, in the following subparagraphs we will first investigate the evolution of the optical and electrical properties of these structures as a function of Ag metal film thickness. Then the effect of post deposition annealing, under the temperature conditions normally used for manufacturing a thin film solar cell, will be discussed.

3.2.1 Appropriate Ag thickness

AZO/Ag/AZO multilayers, with different silver thickness, were sequentially deposited on soda lime glass substrates by RF magnetron sputtering at room temperature and without vacuum break. The substrates were first cleaned in acetone, rinsed in deionised water and in absolute ethanol, then placed parallel to the target surface at a distance of 7 cm. The base pressure of the sputtering chamber was $\sim 2 \times 10^{-3}$ Pa prior to deposition and the sputtering process was performed with a working pressure of 2 Pa in argon atmosphere. AZO layers (top and bottom) were deposited with a sputtering power of 150 W, while the Ag layers at power of 30 W. Before each run, both targets were pre-sputtered in a pure Ar atmosphere for few minutes in order to remove the natural surface oxide layers. The Ag mid-layers were grown, with a rate of 0.2 nm/s, with various sputtering times in order to have different thickness, while the AZO layers were grown, with a rate of 0.33 nm/s, keeping the sputtering time fixed at 60 s. For comparison a 40 nm AZO thin film, without the silver intralayer, was also grown.

Rutherford Backscattering Spectrometry (RBS) in high resolution mode was employed to quantify the doses of Ag and Zn in the AZO/Ag/AZO structure. A 2.0 MeV He⁺ ion beam hits the sample surface at normal incidence, while backscattered He atoms are detected at an angle (independently measured) of 106° from the beam axis. The overall energy resolution (14 keV) and the glancing detection mode allowed to distinguish

between the top and bottom AZO layers and to check the broadening of Ag or Zn profiles after annealing, if any, Fig.9. Scheme of the RBS experimental set-up is shown in the inset of figure 9.

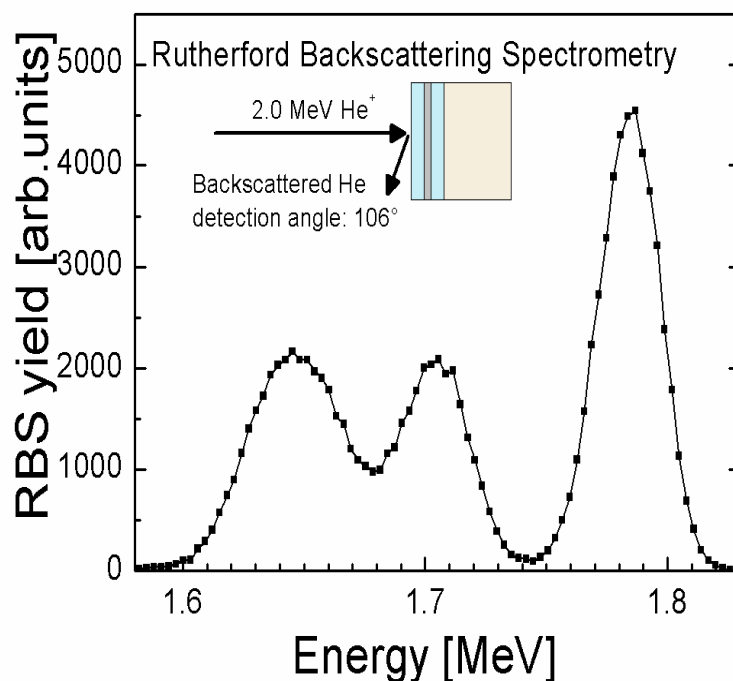


Figure 9: Typical Rutherford backscattering spectra in “glancing detection” of AZO/Ag/AZO multilayers grown on glass substrate. The peak centered at 1.8 MeV is relative to He backscattered from Ag atoms, while the two peaks at 1.7 and 1.65 MeV are due to backscattering from the Zn atoms in the top or bottom AZO layers, respectively

Once Ag and Zn doses have been quantified, the layer thickness is derived by assuming a proper atomic density (5.6×10^{22} Ag at./cm³ and 4.2×10^{22} Zn at./cm³, corresponding to the Zn atomic fraction of 46 at.% in the AZO, respectively): top and bottom AZO layers were to be ~20 nm, while the Ag film thickness ranges from 3 to 19 nm. By means of UV-VIS-NIR spectrophotometer, as previously described, the variation in the transmittance

spectra of the as deposited AZO/Ag/AZO multilayered structures as a function of the Ag thickness has been observed, Fig.10.

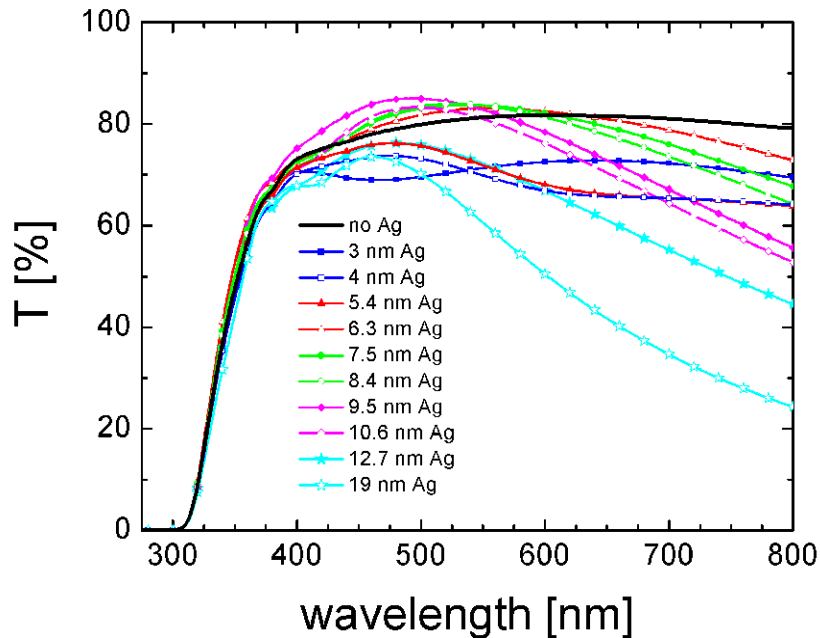


Figure 10: Optical transmittance spectra observed in AZO/Ag/AZO multilayers with various silver film thicknesses.

It can be clearly seen that as the metal layer increases from 0 to 5.4 nm, the amplitude of the transmittance curve is reduced in all the wavelength range with respect to the sample without Ag. For Ag thickness going from 6.3 to 10.6 nm there is an increase of T in the range 400–600 nm. Then, with further increase of thickness of Ag layer, transmittance decreases and the spectra with 19 nm of silver show the lowest transmittance, as expected. The average values of the transmission, $\langle T \rangle$, in the visible range (400–800 nm) of all multilayers are reported in Fig.11(a) versus the Ag film thickness. In Fig.11(b) the corresponding sheet resistances are shown. An abrupt drop of R_{sh} , as large as 4 to 5 orders of magnitude, can be observed by inserting Ag as

interlayer between the two AZO films. It is observed that sheet resistance decreases with the increase of Ag thickness, as expected. The lowest R_{sh} value of about $2.5 \Omega/sq$ is measured for the 19 nm thick Ag mid-layer

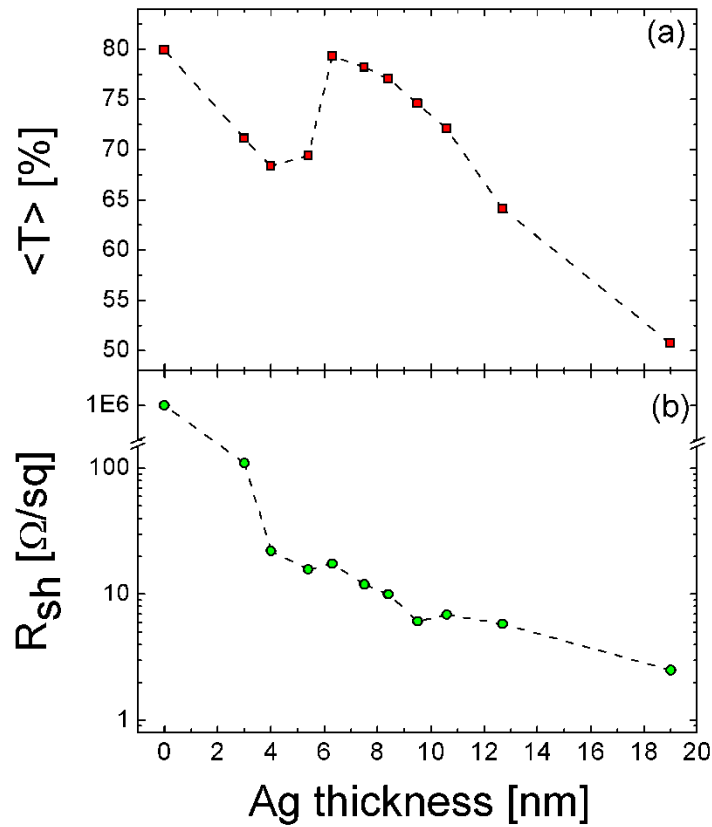


Figure 11: (a) $\langle T \rangle$, the average values of the transmission in the visible range (400–800 nm), and (b) R_{sh} of AZO/Ag/AZO multilayers as a function of silver film thickness.

A simple parallel model can be used to explain the improvement of the electrical properties due to the addition of Ag as interlayer [38]. The measured resistance of the whole structure, R_{sh} , can be expressed as a function of the resistance of the single layers coupled in parallel, as:

$$\frac{1}{R_{Sh}} = \frac{1}{R_{AZO\ top}} + \frac{1}{R_{Ag}} + \frac{1}{R_{AZO\ bottom}} \quad 1$$

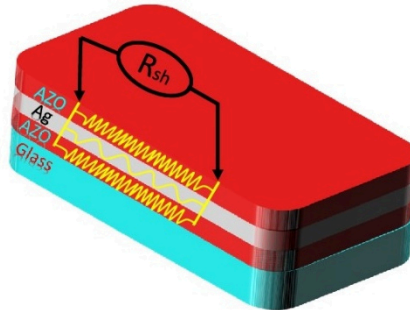


Figure 12: Scketch of the electrical behaviour of AZO/Ag/AZO transparent electrode

Since the Ag resistivity is much lower than AZO, the total resistance mainly depends on R_{Ag} and the AZO/Ag/AZO film has a lower resistance than AZO film of the same dimensions. In our samples, the presence of Ag leads to an electrical resistivity going from $5.5 \times 10^{-4} \Omega\text{cm}$ to a value as low as $1.8 \times 10^{-5} \Omega\text{cm}$. The optical and electrical features can be attributed to the evolution of the metallic film with the deposition time. Scanning electron microscope images show that at the beginning of sputtering, Ag was deposited as islands with various sizes and randomly distributed on the AZO substrate. As the sputtering time was carried on further, the gap between separated clusters was decreased, and the silver islands coalesced having properties closer to those of a continuous film [39]. From Fig.10, we found that the presence of Ag, with thickness going from 6.3 to 10.6 nm, improves the transmittance in the 400–600 nm range. For a better understanding of such behavior, reflectance spectra have also been analyzed. Fig.13 compares the spectral data acquired on two samples, one with 9.5 nm of silver, one without.

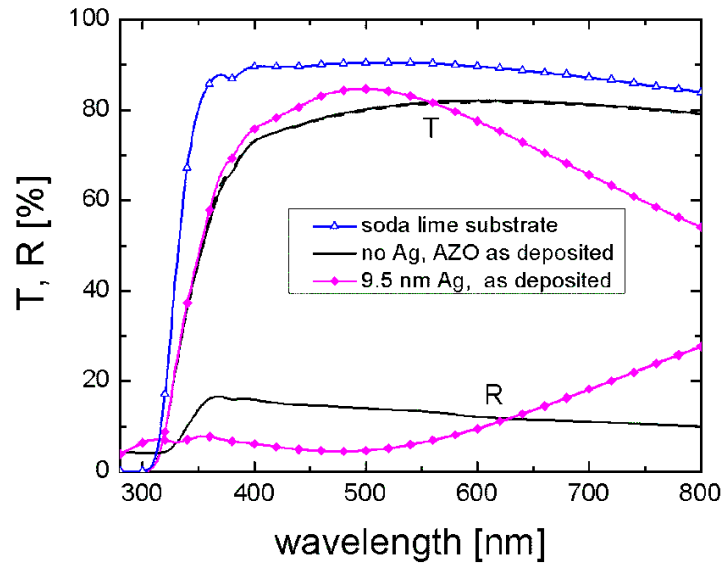


Figure 13: Optical transmittance and reflectance spectra of two samples: one with 9.5 nm of silver, one without. Transmittance of the uncoated soda lime substrate is also reported.

It can be seen that the transmittance enhancement observed in presence of silver is associated to a significant reduction in the reflectance. For the sake of clarity, transmittance spectrum of the uncoated soda lime substrate, which exhibits a value around 90%, is also reported. The insertion of 9.5 nm thick Ag midlayer leads to an increase of about 7% in the AZO transmittance at 480 nm. This result is related to the occurrence of interference effects due to the variations of refractive index and thickness of films in the multilayer structure.

For any transparent electrode and their relative utility for an application, both optical transmittance and electrical conductivity should be as large as possible. Unfortunately, their correlation keeps out the simultaneous achievement of the maximum for both properties, therefore a few figures of merit [40, 41] are used in the literature in order to compare and select the transparent electrode with the best electro-optical quality. Here we considered the Haacke's figure of merit (F_{TC}) defined as:

$$F_{TC} = \frac{\langle T \rangle^{10}}{R_{Sh}} \quad (2)$$

selecting as $\langle T \rangle$ the mean value measured in the visible range. Fig.14(c) shows the variation of this quality factor as a function of Ag layer thickness.

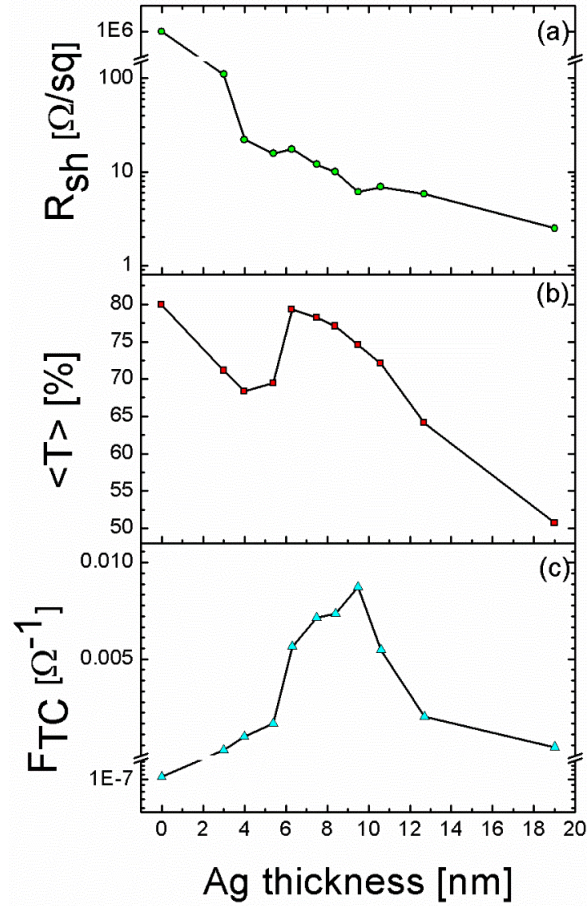


Figure 14: (a) Sheet resistance, R_{sh} , (b) the average values of the transmission in the visible range (400–800 nm), $\langle T \rangle$, and (c) Haacke's figure of merit defined in eq. (2) of AZO/Ag/AZO multilayers as a function of silver film thickness.

We observe a narrow window, related to the deposition process conditions, to the choice of AZO thicknesses as well as to material properties with a

highest F_{TC} of $\sim 9 \text{ m}\Omega^{-1}$ for the Ag layer of 9.5 nm. Thus, we can conclude that our AZO/Ag/AZO electrodes have reached high values for the figure of merit, competitive with the ones reported in literature. Sutthana et al. measured a maximum F_{TC} of $\sim 0.5 \text{ m}\Omega^{-1}$ for AZO/Ag/AZO multilayer, deposited by DC magnetron sputtering, with 8 nm of Ag [6]; Sahu e coworkers reported a maximum value of $\sim 25 \text{ m}\Omega^{-1}$ for AZO/Ag/AZO multilayer, synthesized by e-beam evaporation, with 12 nm of Ag [7].

3.2.2 Temperature effect

Effect of post deposition annealing, under the temperature conditions normally used for manufacturing a thin film solar cell, has also been investigated. The annealing was performed in N_2 ambient for a number of selected samples at 240°C, and 400°C, for 30 min. Transmittance spectra before and after annealing, are shown in Fig.15.

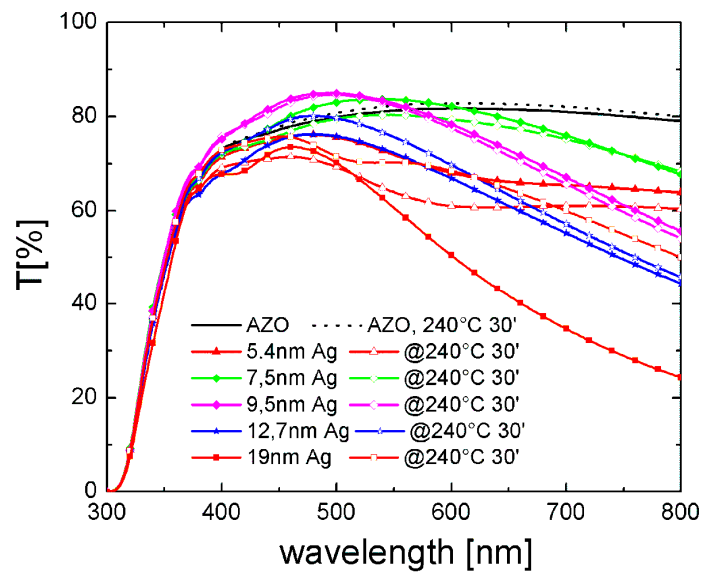


Figure 15: Transmittance spectra of AZO/Ag/AZO multilayered films before and after annealing at 240 °C, 30 min.

By means of Haacke's figure of merit we compared the data measured before and after the annealing at 240 °C for 30 min, Fig.16. It can be seen that a peaked curve still exists and gets the maximum for the 9.5 nm Ag mid-layer. Nonetheless, a reduction in performance has been measured for Ag thickness below 12 nm, probably due to agglomeration of Ag film which reduces the electrical conductivity. As the silver layer becomes thicker, a slight increase in F_{TC} is clearly observed, still the low transmittance value for this thickness hinders their application.

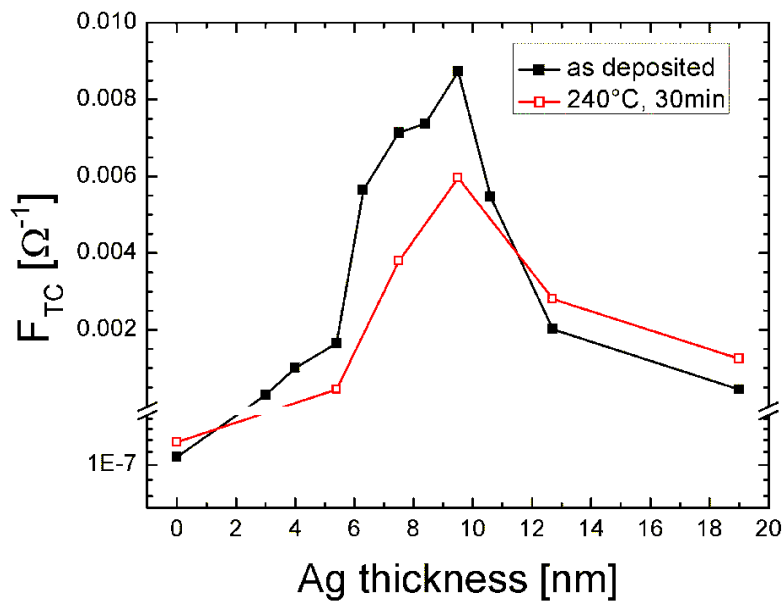


Figure 16: F_{TC} , defined in Eq. (3.2), of AZO/Ag/AZO multilayered films, as deposited and after annealing at 240 °C, 30 min, as a function of silver layer thickness.

3.2.3 Thermal stability

Fig.17 displays a sketch of a typical structure of α -Si:H thin film solar cell using an AZO/Ag/AZO transparent electrode as front contact. It is straightforward to consider that if the AZO/Ag/AZO is deposited on top of

the Si absorbing layer, even a small diffusion of Ag towards the Si layer would be detrimental for the overall performance of the solar cell. Therefore, the final step of the analysis on the multilayer is to perform a check on its thermal stability: is AZO thin film an efficient barrier against Ag diffusion toward silicon?

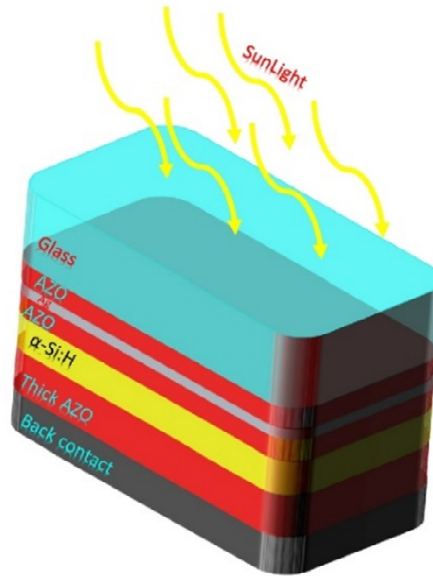


Figure 17: sketch of α -Si:H solar cell using an AZO/Ag/AZO transparent electrode.

By means of RBS technique we investigated the thermal stability of the AZO/Ag/AZO structure at temperature as high as 400 °C, well above the thermal budget seen during the typical solar cell fabrication.

The energy spectra of He⁺ backscattered by best sample AZO_20nm/Ag_9.5nm/AZO_20nm before and after annealing at 400°C, 30 min are reported in Fig.18. The peak centered at 1780 keV is relative to He backscattered from Ag atoms, while the two peaks at 1700 and 1650 keV are due to backscattering from the Zn atoms in the top or bottom AZO layers,

respectively. It should be noted that the experimental configuration permits to resolve the top and bottom AZO layers and that the full width at half maximum of all the peaks (30 keV, at least) are well larger than the energy resolution, allowing to determine any broadening of the Ag or Zn profiles. The overlapping between the as-deposited and annealed spectra shows that no modification of the AZO/Ag/AZO structure occurs during thermal treatment up to 400°C and thus no diffusion of Ag is measured through the AZO layers.

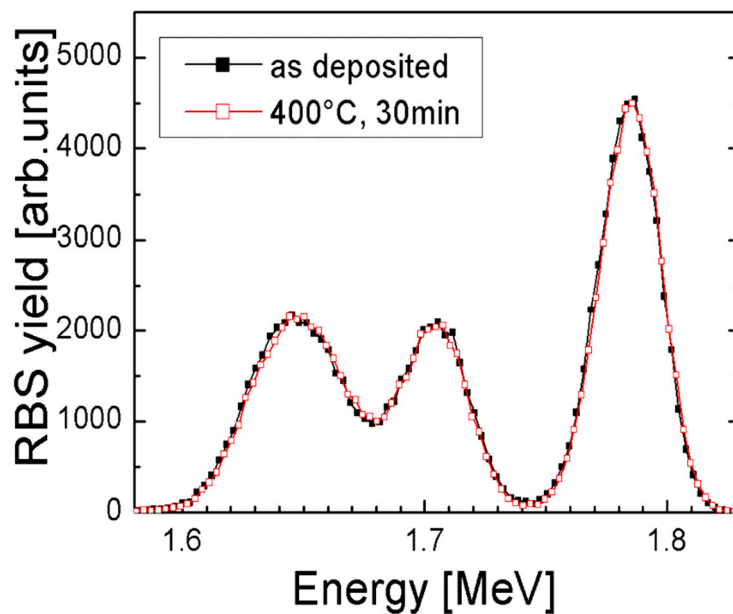


Figure 18: Energy spectra of He backscattered by AZO/Ag/AZO samples as deposited and after annealing at 400 °C, 30 min. A scheme of the RBS experimental set-up is reported in the inset.

This evidence points out that an AZO film as thin as 20 nm is an excellent barrier to Ag diffusion, while a thin Ag film deposited onto α -Si:H, after annealing at 180 °C, 1 h, was measured to diffuse more than 50 nm in the Si substrate. As demonstrated by the the RBS signals in Fig.19 before and after the thermal process.

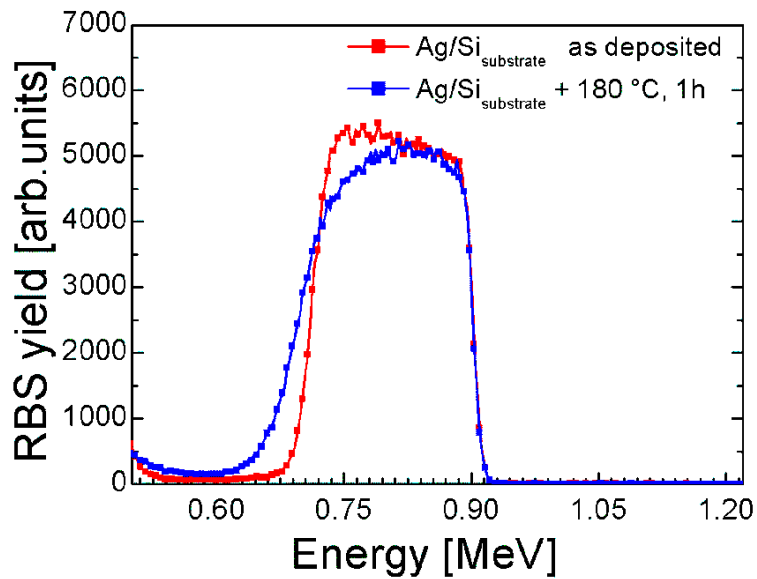


Figure 19: RBS spectra of Ag deposited on α -Si:H before and after annealing at 180°C, 1h.

3.3 TCO/Ag/TCO

Multilayers with different kinds of TCO and metals have been reported in the literature, mostly with a single type of TCO encapsulating a very thin metallic film. Although to date TCO/metal/TCO multilayer has been deeply investigated, there is still a lack of knowledge to transfer these materials in a real fabrication process for thin film solar cells. For this reason, in this paragraph we have investigated and compared the structural, electrical and optical properties of several sequences of TCO/Ag/TCO multilayers. In particular, TCO/Ag/TCO structures were deposited with all combinations of AZO and ITO as top and bottom layers in order to investigate the role, if any, of the sequence of the top and bottom TCO layers on the whole properties of the transparent electrodes.

3.3.1 ITO and AZO: a comparative investigation

AZO/Ag/AZO, ITO/Ag/ITO, AZO/Ag/ITO and ITO/Ag/AZO multilayers were deposited on soda lime glass substrates by RF magnetron sputtering at room temperature. A bottom/Ag/top notation is used, so that AZO/Ag/ITO indicates that AZO is the bottom layer while ITO is the top one. AZO and Ag thin film were deposited as previously described, while ITO thin films were deposited at 175 W and 0.18 nm/s. For comparison, samples with 100 nm of AZO and ITO were also prepared.

Figure 20 shows the RBS spectra of our TCO/Ag/TCO samples. The peak at about 1.70 MeV is related to He^+ backscattered by the Ag layers, the two peaks at 1.57 and 1.51 MeV are related to He^+ backscattered by Zn in the AZO top and bottom layers, respectively, while the peak at 1.73 MeV is related to He^+ backscattered by In in the ITO top layer. Due to their close atomic numbers, it is not possible to distinguish between In and Sn signals, as well as between In from bottom ITO layer and Ag signals. RBS measurements and spectra simulation allowed to determine the thickness of the films in the multilayer. The top and bottom TCO layers were 50 ± 5 nm, while the embedded Ag layer was estimated to be 10 ± 1 nm.

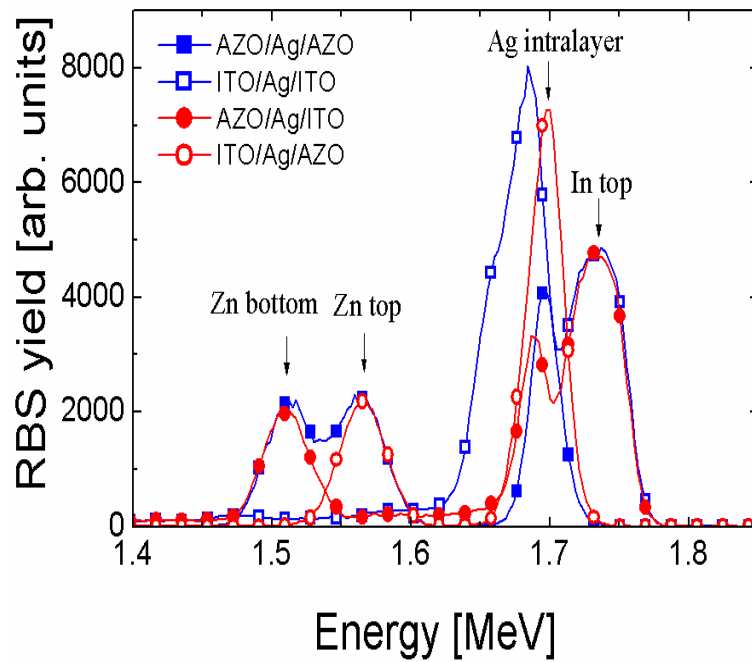


Figure 20: Rutherford backscattering spectra of TCO/Ag/TCO multilayers grown on glass substrate.

Figure 21 shows the cross-section SEM image of the AZO/Ag/AZO sample, where the typical polycrystalline columnar structure of the AZO can be clearly observed. The thicknesses calculated by the RBS data were confirmed by the SEM analyses. Figure 21 shows a continuous Ag layer with a homogeneous thickness of ~ 10 nm as given by the FWHM of the peak obtained using the image analysis software (inset of the figure). The sharp boundary among the layers also reveals no diffusion of Ag into TCO films during the deposition, which is in agreement with our previous data showing that the AZO acts as an excellent barrier against the diffusion of Ag, even at temperatures as high as 400 °C.

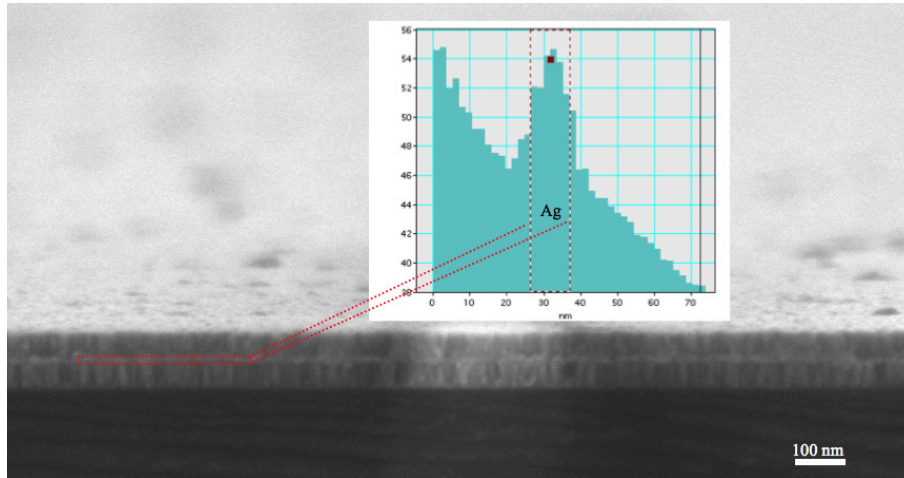


Figure 21: Cross sectional SEM image of the AZO/Ag/AZO multilayer. The inset is the output of the software used to estimate the thickness of the Ag intralayer. The FWHM of the peak is 10.5 nm

Table 4 reports the thickness, resistivity, average value of the optical transmittance $\langle T \rangle$ in the 400–800 nm range, and that measured at 550 nm wavelength, T_{550} , for all samples. These data will be now compared and discussed. As far as the electrical characterization is concerned, AZO and ITO single layers of thicknesses in the range of 50–100 nm exhibit a resistivity of about $10^{-2} \Omega\text{cm}$ or higher, depending on the nature of TCO (see Table 4) and deposition process parameters. Moreover, the conduction through the thin TCO or metal layer depends on the Ag morphology. Previously, we found, in agreement with the literature [10], that a thickness of about 10 nm for the Ag layer is the best compromise in between optical transparency and electrical conductivity. For lower thickness, in fact, it has been reported a discontinuous, clustered Ag layer [42]. Therefore, the insertion of 10 nm of Ag between the top and bottom TCO layers leads, for all samples, to a sheet resistance, suitable for solar cell application, of about $10 \Omega/\text{sq}$.

Sample	Thickness s [nm]	Resistivity [Ωcm]	$\langle T \rangle$ [%]	T_{550} [%]
AZO	100	3×10^{-1}	79	79
ITO	100	3×10^{-2}	79	83
AZO/Ag/AZO	50/10/50	$\sim 1 \times 10^{-5}$	75	79
AZO/Ag/ITO	50/10/50	$\sim 1 \times 10^{-5}$	76	78
ITO/Ag/AZO	50/10/50	$\sim 1 \times 10^{-5}$	80	86
ITO/Ag/ITO	50/10/50	$\sim 1 \times 10^{-5}$	68	74

Table 4: Thickness, resistivity, visible average transmittance and transmittance at 550 nm wavelength of all samples.

In the case of TCO/Ag/TCO, the sheet resistance of the whole structure, R_{sh} , can be expressed by equation 1, confirming that the Ag film controls the whole conduction of these three-layer electrodes, with a resistivity of about $10^{-5} \Omega\text{cm}$, lower than a conventional and thicker ITO single layer, $1\text{--}2 \times 10^{-4} \Omega\text{cm}$ [13]. Our data indicate a resistivity of the Ag layer seven times higher than the bulk value, which can be explained by the very low thickness of our Ag films of the same order of magnitude of the mean free path of conduction electrons in good metals (10^{-8}m).

Despite of the very similar electrical properties, the optical behavior of our multilayer electrodes depends on the TCO nature and, in particular, on the sequence of the TCO films. The low absorption of the silver thin film in the visible-NIR range [43] is essential to increase the light transmission of the multilayer structure. To maximize the transmittance in the visible range, TCOs' thickness was set at 50 nm (TCO thicknesses in the range of 30–60 nm are commonly used). Figures 22 (a) and (b) report the optical transmittance and reflectance of our samples along with AZO and ITO single layers for comparison. The transmittance of the glass substrate is also reported. All the

optical data include the substrate contribution. The absorbance, calculated as $A = 100 \% - (T + R)$, is displayed in Fig.22 (c).

As far as the transmittance is concerned, the wavelength region around 650 nm shows very similar T values for all samples. The symmetric ITO/Ag/ITO structure exhibits the worst performance all over the wavelength range, followed by the AZO/Ag/AZO structure. Concerning the asymmetric structures, we observe a higher T with respect to the symmetric ones, at least in one of the regions below or above the 650 nm reference point. The best transmittance below 650 nm is observed for the ITO/Ag/AZO sequence which, above this wavelength value, reproduces the same transmittance of AZO/Ag/AZO. On the other hand, the best T above 650 nm is obtained by the AZO/Ag/ITO structure which, below this wavelength value, has the same T of the AZO/Ag/AZO sample. When compared to the single TCO (AZO or ITO) films, the multilayer structure exhibits a more structured behavior of the T curves. Single TCO samples have a higher T in between 350 and 450 nm, and above 900 nm wavelengths. Reflectance curves are reported in Fig.22(b), showing that most of the variations observed in the T spectra are related to the R behavior rather than to a different light absorption. All multilayer structures have a clear minimum around 650 nm wavelength, in some cases extended to a wide region of the visible range (450–750 nm). On the contrary, TCO single layer has an almost constant R value of about 20 %.

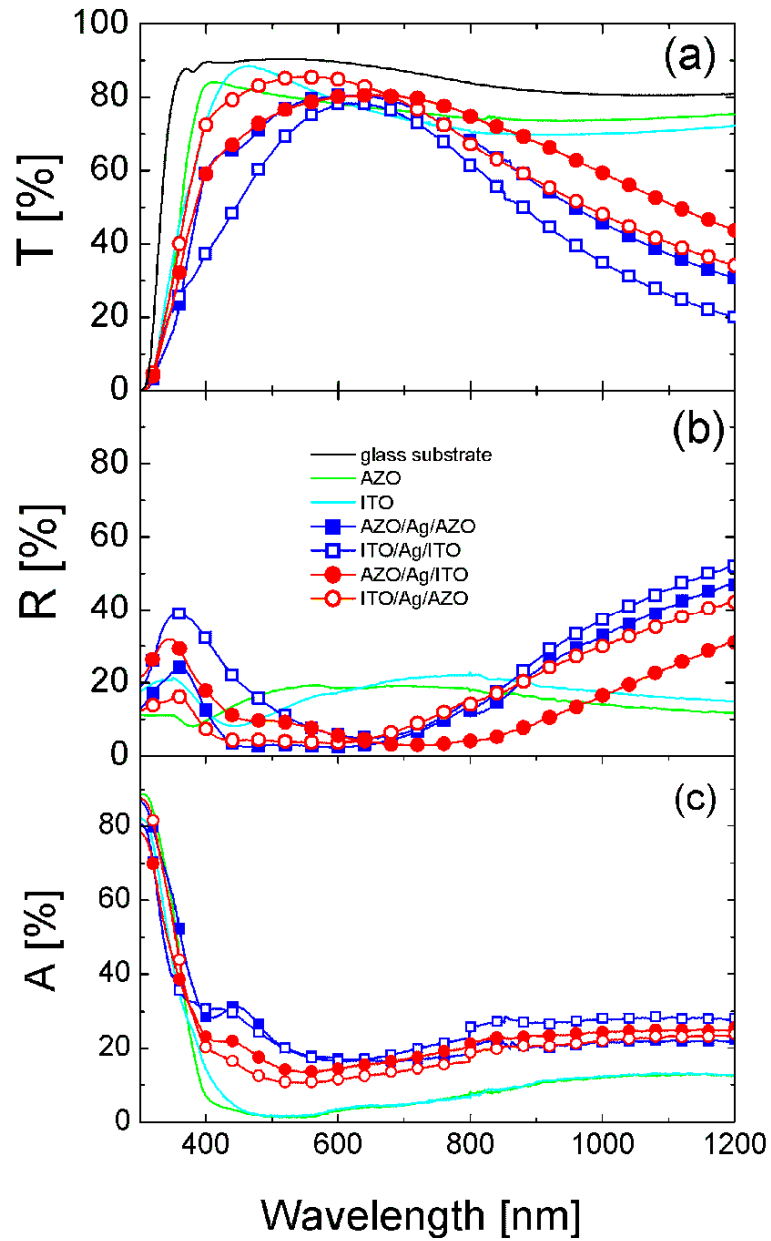


Figure 22: Optical transmittance (a), reflectance (b) and absorbance (c) spectra of TCO single layers and TCO/Ag/TCO multilayers, expressed in percentage.

However, if we look at the absorbance of Fig.22(c), all multilayer samples show an almost constant trend above 450 nm, with higher values with respect to single TCOs. An overlook of the transmittance, reflectance and absorbance spectra of Fig.22 allows to highlight some important points. It is clear that the TCO single layers have a much lower absorbance with respect to the structure containing the Ag film in the whole spectral range, but the very low reflectance of the TCO/Ag/TCO samples in the 450–750 nm wavelength window produces similar, or even higher, transmittance values. Moreover, the presence of ITO or AZO as top and bottom TCO in the asymmetric multilayer samples has strong consequences on the transmittance of the whole structure, allowing a selective tailoring of this parameter in different wavelength ranges (in our case, below and above 650 nm). The observed behavior is clearly related to the variation of the reflectivity (Fig.22(b)). Depending on the sequence of the TCO top and bottom layers in our samples, we changed the R values in the different wavelength regions and, as a consequence, the T values. In a multilayer thin film structure, this effect can be ascribed to small differences in the thickness and/or in the refractive indices “n” of each single layer. In our case, although the thickness of TCO and Ag films calculated by RBS is affected by an error of about 5 and 1 nm, respectively, the systematic difference between symmetric and asymmetric structures suggests that the refractive indices of ITO and AZO thin films [44,45] play a major role. In particular, the “n” curves of ITO and AZO have an intersection at around 570 nm [46], almost in correspondence with the observed crossing of reflectance (and transmittance) in our samples. Moreover, further data in the literature show a similar behavior for ITO/ZnO combination [47]. This peculiarity of the multilayered samples could be employed to decrease or increase the reflectivity of the front and back transparent electrodes, respectively, in a proper range of the solar spectrum, with possible advantages in the case of semi-transparent photovoltaic solar cells.

To compare the electrical and optical performances for different transparent electrodes, we again considered the Haacke’s figure of merit defined previously (Eq.2). Using the value of T at 550 nm, we found F_{TC} values

in between $4.9 \times 10^{-3} \Omega^{-1}$ (for ITO/Ag/ITO) and $4.9 \times 10^{-3} \Omega^{-1}$ (for ITO/Ag/AZO), depending on the sequence of the TCOs. These values, except for the lowest one, are comparable to those reported in the literature [9, 10,13]. From the previous results, the asymmetric multilayer structures seem to have the best performances as transparent electrodes and, moreover, they offer the possibility of tuning the optical transmittance in selected wavelength ranges.

3.4 Conclusions

In this chapter we presented a detailed experimental investigation on the synthesis, structural analysis and electro-optical properties of TCO/Ag/TCO. In particular, we studied the role of silver thickness on the electrical and optical properties of AZO/Ag/AZO as well as the effect of a thermal annealing up to 400 °C on these properties. Moreover, we have studied structural, optical and electrical behaviors of thin TCO/Ag/TCO transparent electrodes with all possible combinations of AZO and ITO as external TCO layers, in order to investigate the role, if any, of the sequence of the top and bottom TCO layers.

From the data reported and discussed along this chapter, the following conclusion can be drawn: AZO/Ag/AZO structures have been studied and optimized in terms of high electrical conductivity and transmittance. The inclusion of a thin Ag film within the AZO layer is highly beneficial, allowing to strongly reduce the TCO thickness from the typically used 1 μm to about 50 nm, and, at the same time, to maintain a low electrical conductivity and high transmittance. The best structure was shown to have a 9.5 nm Ag film as the mid-layer. Thermal stability of the AZO/Ag/AZO structures was investigated, demonstrating an excellent behavior of the AZO film as a barrier to Ag diffusion. Finally, the ultra-thin AZO/Ag/AZO structures investigated are shown to have electro/optical properties competitive with the thicker TCO layer currently used in thin film solar cells.

Our data demonstrate that a single TCO layer of 100 nm has good optical properties but a very high electrical resistivity, not suitable for practical applications. On the other hand, the TCO/Ag_10nm/TCO samples, with the same total thickness, have shown good optical properties coupled with an excellent electrical conductivity. In particular, the multilayered structures have shown better performances when the top and bottom TCOs are of different types and the possibility of tuning the reflectivity in a proper range of wavelengths, which is very attractive for applications in devices requiring transparent electrodes such as, for example, front and back contacts in semitransparent solar cells.

Finally, these results clearly demonstrate that electrical-optical properties of TCO/Ag/TCO are strongly influenced by Ag thickness, TCO thickness and the sequence of the top and bottom TCO layers. However, by a careful control of these parameters it is possible to tune the optical response and to achieve an appropriate sheet resistance for their application as transparent electrodes. Moreover, the samples have been deposited at room temperature, while standard thick TCO layers often require a thermal process to improve final electro-optical performances. The absence of a thermal budget and the very low thickness of our samples are very promising also for applications on flexible devices fabricated on plastic substrates.

References

- [1] G. Leftheriotis, S. Papaefthimiou, P. Yianoulis, *Solid State Ionics* **655**, 136–137 (2000).
- [2] A. Kloppel, B. Meyer, J. Trube, *Thin Solid Films* **392**, 311-314 (2001).
- [3] M. Fahland, P. Karlsson, and C. Charton, *Thin Solid Films* **392**, 334-337 (2001).
- [4] K. J. Choi, J. Y. Kim, Y. S. Lee, and H. J. Kim, *Thin Solid Films* **341**, 152-155 (1999).
- [5] Y. S. Jung, Y. W. Choi, H. C. Lee, and D. W. Lee, *Thin Solid Films* **440**, 278-284 (2003).
- [6] S. Sutthana, N. Hongsith, S. Choopun, *Current Applied Physics* **10**, 813-816 (2010).
- [7] D. R. Sahu, S. Y. Lin, J. L. Huang, *Sol. Energy Mater. Sol. Cells* **91**, 851-855 (2007).
- [8] D. R. Sahu, J. L. Huang, *Sol. Energy Mater. Sol. Cells* **93**, 1923-1927 (2009).
- [9] M. Girtan, *Sol. Energy Mater. Sol. Cells* **100**, 153-161 (2012).
- [10] C. Guillén, J. Herrero, *Thin Solid Films* **520**, 1-17 (2011).
- [11] Ho-Kyun Park, Jae-Wook Kang, Seok-In Na, Don-Yu Kim, Han-Ki Kim, *Sol. Energy Mater. Sol. Cells* **93**, 1994-2002 (2009).
- [12] Hyun-Jin Cho, Kyung-Woo Park, Jun-Ku Ahn, Nak-Jin Seong, Soon-Gil Yoon, won-Ho Park, Sung-Min Yoon, Dong-Jun Park, Jeong-Yong Lee, *Journal of the Electrochemical Society* **156**, J215-J220 (2009).
- [13] K. Ellmer, *Nature Photonics* **6**, 809-817 (2012).
- [14] D.R. Sahu, J.L. Huang, *Thin Solid Films* **516**, 208-211 (2007)
- [15] K. Sivaramakrishnan, T.L. Alford, *Appl. Phys. Lett.* **94**, 052104 3 pp. (2009).
- [16] S. Song, T. Yang, M. Lv, Y. Li, Y. Xin, L. Jiang, Z. Wu, S. Han, *Vacuum* **85**, 39-44 (2010).
- [17] T. Dimopoulos, G.Z. Radnoczi, B. Pécz, H. Brückl, *Thin Solid Films* **519**, 1470-1474 (2010).

- [18] D. Kim, *Appl. Surf. Sci.* **256**, 1774-1777 (2010).
- [19] D.R. Lide (Ed.), *Handbook of Chemistry and Physics*, CRC Press, Boca Raton, FL, 1997.
- [20] J.C. Kim, C.H. Shin, C.W. Jeong, Y.J. Kwon, J.H. Park, D. Kim, *Nucl. Instrum. Meth. Phys. Res. B* **268**, 131-134 (2010).
- [21] C.H. Cheng, J.M. Ting, *Thin Solid Films* **516**, 203-207 (2007).
- [22] M.F. Al-Kuhaili, M.A. Al-Maghrabi, S.M.A. Durrani, I.A. Bakhtiari, *J. Phys. D: Appl. Phys.* **41**, 215302 8 pp. (2008).
- [23] M.A. Al-Maghrabi, M.F. Al-Kuhaili, S.M.A. Durrani, I.A. Bakhtiari, *J. Vac. Sci. Technol. A* **27**, 276-281 (2009).
- [24] K. Koike, S. Fukuda, *J. Vac. Sci. Technol. A* **26**, 44-47 (2008).
- [25] M. Bender, W. Seelig, C. Daube, H. Frankenberger, B. Ocker, J. Stollenwerk, *Thin Solid Films* **326**, 67-71 (1998).
- [26] Smith G.B., Niklasson G.A., Svensson J.S.E.M., and Granqvist C.G., *J. Appl. Phys.* **59**, 571-581 (1986).
- [27] Kaiser N., *Appl. Opt.* **41**, 3053-3060 (2002).
- [28] I. Crupi, S. Boscarino, V. Strano, S. Mirabella, F. Simone, A. Terrasi, *Thin Solid Films* **520**, 4432-4435 (2012).
- [29] S. Boscarino, I. Crupi, S. Mirabella, F. Simone, A. Terrasi, *Appl. Phys. A* **116**, 1287-1291 (2014).
- [30] S.H. Mohamed, *J. Phys. Chem. Solids* **69**, 2378-2384 (2008).
- [31] H.K. Park, J.W. Kang, S.I. Na, D.Y. Kim, H.K. Kim, *Sol. Energy Mater. Sol. Cells* **93**, 1994-2002 (2009).
- [32] J.A. Jeong, Y.S. Park, H.K. Kim, *J. Appl. Phys.* **107**, 023111-023119 (2010).
- [33] Y. Abe, T. Nakayama, *Mater. Lett.* **61**, 3897-3900 (2007).
- [34] K.L. Chopra, M.R. Randlett, *J. Appl. Phys.* **37**, 3405-3407 (1968).
- [35] C. Guillén, J. Herrero, *Sol. Energy Mater. Sol. Cells* **92**, 938-941 (2008).
- [36] K.L. Chopra, M.R. Randlett, *J. Appl. Phys.* **39**, 1874-1881 (1968).
- [37] K. Sarakinos, J. Wördenweber, F. Uslu, P. Schulz, J. Alami, M. Wuttig, *Surf. Coat. Technol.* **202**, 2323-2327 (2008).
- [38] E.J.J. Martin, M. Yan, M. Lane, J. Ireland, C.R. Kannewurf, R.P.H. Chang, *Thin Solid Films* **461**, 309-315 (2004).

- [39] D. Zhang, H. Yabe, E. Akita, P. Wang, R. Murakami, X. Song, *J. Appl. Phys.* **109**, 104318-104322 (2011).
- [40] G. Haacke, *J. Appl. Phys.* **47**, 4086-4089 (1976).
- [41] S. De, J.N. Coleman, *ACS Nano* **4**, 2713- 2720(2010).
- [42] D.S. Ginley, H. Hosono, D.C. Paine, *Handbook of transparent Conductors* (Springer-Verlag, 2010).
- [43] J. Szczyrbowski, A. Dietrich, K. Hartig, *Sol. Energy Mater. Sol. Cells* **19**, 43–53 (1989).
- [44] O. Fukuoka, N. Matsunami, M. Tazawa, T. Shimura, T. Sataka, H. Sugai, S. Okayasu, *Nucl. Instr. Meth. B* **250**, 295–299 (2006).
- [45] 17. S.H. Mohamed, F.M. El-Hossary, G.A. Gamal, M.M. Kahlid, *Acta Phys. Pol., A* **115**, 704–708 (2009).
- [46] E. Centurioni, *Appl. Opt.* **44**, 7532–7539 (2005).
- [47] Y. Yang, X.W. Sun, B.J. Chen, C.X. Xu, T.P. Chen, C.Q. Sun, B.K. Tay, Z. Sun, *Thin Solid Films* **510**, 95–101 (2006).

Chapter 4

Laser scribing processes on AZO/Ag/AZO

In this chapter, we will investigate the laser irradiation of AZO/Ag/AZO transparent contacts for segmentation purpose. In particular, we will demonstrate how the energy density threshold for the ablation of transparent contacts can be significantly reduced, eight order of magnitude, by replacing the standard thick AZO single layer with a ten times thinner AZO/Ag/AZO multilayer structure.

The quality of the irradiated area has been experimentally checked by electrical resistance measurements, and the results are discussed on a thermal based model used for a numerical simulation of the laser process. The experimental results and the numerical simulation provide clear evidence that the presence of Ag intralayer plays two important roles on the laser scribing process: the increasing of the maximum temperature reached in the structure during the process and the fastening of the cooling after the laser irradiation. These results clearly demonstrate the great opportunities for the implementation of thin AZO/Ag/AZO transparent electrodes as a suitable candidate for use in large-area modules, liable for segmentation, such as α -Si:H solar cells.

4.1 Laser application in thin film solar cells

The realization of high-efficiency solar cells modules with lower process cost is currently one of the most important technical issue for solar cell producers [1]. A key role along this road can be played by the laser technology [2,3], which, involved in the monolithic interconnection process of modules, delivers many benefits, like lower fabrication costs, high throughput and higher performances compared to mechanical scribing methods in terms of quality, speed and reliability.

Varieties of thin film solar cells include a-Si, CdTe (cadmium telluride), CIGS (copper indium gallium selenide), multijunction a-Si variants such as the tandem micromorph structure, organics solar cells and also new cell designs (quantum dot, dye-sensitized, and perovskite solar cells) [3,4].

It is important to understand that, in the thin film technology, the materials are arranged in a layered structure on a large panels of glass, usually 1,1 m x 1,3 m, which is typically divided by laser scribing processes into an array of narrow solar cells (between 100 and 200) electrically connected in series; so these scribing processes create a more practical and efficient low-current/high voltage module. Moreover, in order to maximize one key advantage of thin-film device, namely low-cost and high-volume production, the next-generation of thin film technology will move to 2,2 m x 2,6 m. The first USA patent for the monolithic series connection of Si thin film solar cells modules performed by laser scribing process dates from 1981 and it belongs to Joseph J. Hanak [5]. Have been made innovations both solar cell engineering and laser technology ever since, nevertheless the standard method holds steady: each material deposition step is followed by a scribing step to create the suitable interconnects between cells.

Each panel is built in superstrate configuration, see the schematic cross-section in Fig.1, it means that sunlight will pass through the glass substrate, starting off as a bare glass. The first step is to deposit a continuous and uniform layer of TCO with, a typical thickness of a few hundred nanometers, which will form the front transparent electrode. This is followed

by a scribe process called P1 whose purpose is to completely cut through the TCO, defining the edges of each individual cell and insulating each other. The next step is the deposition of a semiconductor layer that form the active region (sunlight absorber), again followed by a scribing step, called P2, which must cut through the absorber layer leaving the TCO intact and creating the pathway for the series interconnection between adjacent cells. The final step is the metal deposition, that forms the back contact, followed by the last laser scribing called P3. This final patterning step must cut through both the absorber (active) layer and the overlying metal electrode, leaving again the TCO intact and defining the edge of each cell. For a whole electrical insulation and corrosion protection the panel, then, has to be laminated with a second sheet of glass.

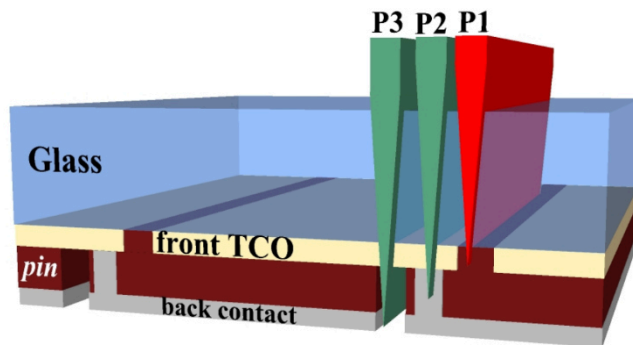


Figure 23: Typical interconnect scheme of a module in superstrate configuration. P1, P2 and P3 indicates the different patterning steps. P1 is performed using an infrared laser to remove the front TCO. P2 and P3 use green laser to cut the Si solar absorber layer and the rear electrode, respectively.

The photovoltaic cell is a composite of multilayer thin films made out of TCO, sunlight absorber semiconductor and metal on a glass substrate, so the different thermal-optical properties, which characterize each one, require different process condition to achieve the complete selectivity removal of each film. The use of mid-infrared or deep UV laser wavelength is

excluded because they are absorbed by the glass. The three used laser scribing processes are detailed below.

The removal of TCO, characterized by low absorption coefficient in the visible range, is based on the absorption of the laser pulse by the free electrons created by degenerate doping, as shown in the previously chapters. This strong absorption increases the temperature of the film, which in turn produces extra free electron (thermal generation) and therefore an increase of the absorption causing, ultimately, the thermal lift-off of the material. The P1 near-infrared wavelength at 1.064 nm is perfect for this purpose because it passes through the glass substrate without damaging it, up to several watts of laser power, and it is strongly absorbed by the transparent electrode layer.

The selective scribing process of the semiconductor, P2, is based on the absorption of green laser wavelength at 532 nm, because both glass substrate and TCO are transparent to this wavelength which, viceversa, is strongly absorbed by the semiconductor. This leads to a temperature increasing which will result in a selective removal of the Si film from the underlying TCO. The removal of metal film (back contact), obtained with P3, is based on the same process of P2, but in practice it removes in a single step both the semiconductor and the metal film from the TCO layer. It is important to highlight that the laser processes previously described are applicable to all thin film photovoltaic technology.

In order to realize high-efficiency solar cells with low process costs while maximizing the conversion efficiency, whole laser process must have specific requirement. First of all, each scribing should not damage the underlying film, with the exception of P3 who has not to ruin only the front transparent electrode (TCO). Since the area between P1 and P3 is a wasted area, it does not contribute to the photo-current, and given that each cell has a total width of less than 10 mm, it is crucial to minimize this wasted area and also the series resistance. Therefore, scribe lines very straight, of 30-100 μm in width, are required, well aligned, placed as close to each other as possible (about hundreds of microns between P1 and P3). We must also consider the cut quality in terms of edge roughness, no recast debris, microcracks and Heat Affected Zone (HAZ – i.e. the change in the a-Si:H

structure at the edge of laser spot); factors that can lead to impoverishment of the electrical-conversion efficiency of the final module [6-9].

Finally, although laser technology is already used for several processes in the photovoltaic industry and it continues to expand, great challenges to improve some key scribing requirements and to process new material combinations still remain. For this reason, a fundamental step in this direction is to study the effects of near infrared laser process on AZO/Ag/AZO multilayer structure and to compare it to thicker AZO currently used in thin film solar cells.

4.2 P1 on AZO/Ag/AZO

In the previous chapter we dealt about the electro-optical properties of TCO/Ag/TCO and on the role played by silver thin film thickness, AZO and/or ITO TCOs, and the effects of the temperature on these multilayer system. Compared to standard TCOs, such electrodes show enhanced conductivity, higher transmission of visible light, lower temperature process, reduced thickness and, consequently, significant cost reduction and improved mechanical flexibility. At present, AZO/Ag/AZO multilayer structures are still far from being implemented on thin film photovoltaic device technology. A crucial aspect is the film patterning process, therefore, this work moves toward the possibility to substitute these multilayer structures for thicker single-layer TCO as frontal transparent electrode in solar cells.

We fabricated “ad-hoc” sample, as illustrated in the insert of figure 2, in superstrate configuration with the AZO/Ag/AZO structure acting as front contact. AZO/Ag/AZO multilayer was sequentially deposited on conventional soda lime glass substrates by RF magnetron sputtering at room temperature in argon atmosphere, as detailed previously [10].

Top and bottom AZO films were deposited under identical conditions with a thickness of about 40 nm, while for the Ag interlayer an optimum

thickness of 10 nm was selected to fabricate a multilayer structure that have high optical transparency ($\langle T \rangle_{400-800\text{nm}}$: 80%; $\langle T \rangle_{800-1200\text{nm}}$: 45%) and good electrical conductivity (R_{sh} : 7.07 ohm/sq; n : $7,58 \times 10^{21}\text{cm}^{-3}$; μ : $12,9 \text{ cm}^2/\text{Vs}$), Fig.2.

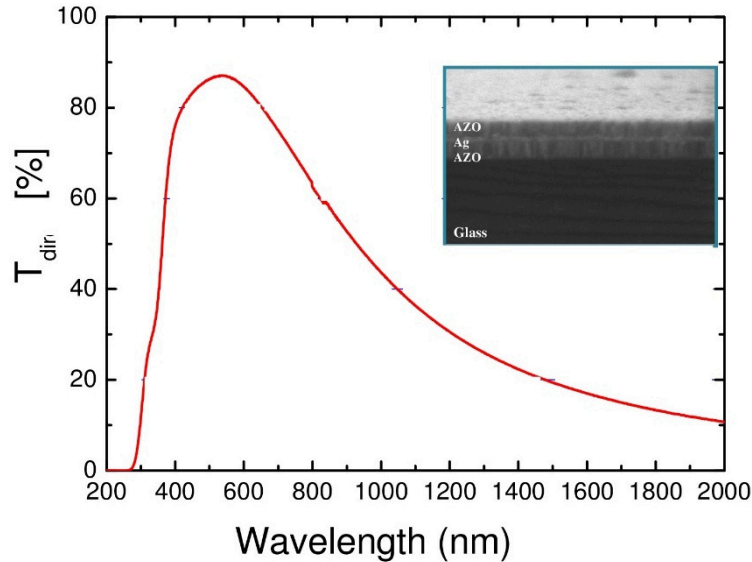


Figure 2: Optical transmittance of AZO/Ag/AZO structure, of 40/10/40 nm thickness.

The thicknesses of the films were verified by Rutherford Backscattering Spectrometry (RBS, 2.0 MeV He⁺ beam) measurements in normal detection mode.

Cut tests of the multilayer structure have been carried out by laser treatments performed in air, by a single pulsed (12 ns) Nd:YAG laser operating with an infrared ($\lambda = 1064 \text{ nm}$), Gaussian shaped (FWHM=1 mm) beam (Quanta-ray PRO-Series pulsed Nd:YAG laser). The laser power was varied to obtain fluences in the range from 1.15 to 4.6 J/cm², with an evaluated error of 25 mJ/cm².

AZO films are extensively used in thin film photovoltaic industry, therefore P1 laser processes on AZO are also carried out in order to compare

the ability to remove the entire film with a single pulse, the energy density threshold for laser damage, electrical isolation and potential benefits using either an AZO single layer or AZO/Ag/AZO structure.

4.2.1 Laser induced structural modifications

We are interested to determine the energy density threshold for the scribing process of the transparent contacts, which leads to an effective material removal with the minimum side effects. To this aim, the morphology of the AZO/Ag/AZO multilayer after the laser irradiation process, as a function of the laser fluence, was investigated by Scanning Electron Microscopy (SEM), which allowed the evaluation of the selective removal of transparent electrodes, additionally to the assessment of the damage of the glass substrate. The challenge is to remove the whole structure without damaging the glass. At high power densities (4.6 J/cm^2) of the ultra-short-pulse laser, although a complete removal of the transparent electrode has been assessed, the glass substrate starts to be damaged and dark area in the center of laser spot were observed. By decreasing the energy density to 1.7 J/cm^2 , we can clearly observe an irradiated region in Fig.3(a) with no damage in the surroundings or cracking in the glass substrate. Figure 3(b) illustrates the well defined cutting edges that leave the bare substrate uncovered with a flat and clean surface. It should be noticed that both edges present undulated profiles, such as obtained by a laceration. This quite large rip ($\sim 200 \mu\text{m}$ wide) ensures an excellent insulation between the not irradiated AZO/Ag/AZO structure and the central area of the laser spot, see Fig.3(c). Such an insulation is further guaranteed by the lift off from the substrate at the line border, as evident from the cross section SEM reported in Fig.3(d).

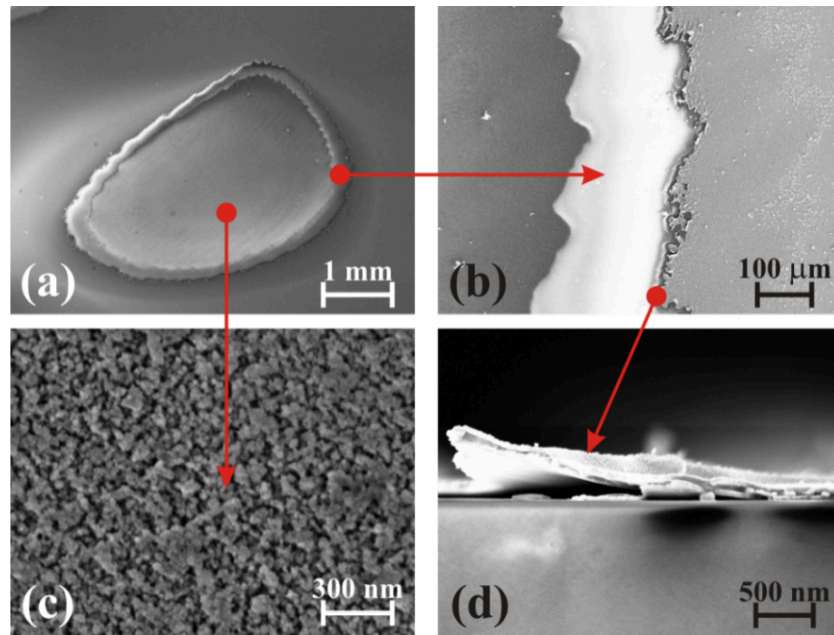


Figure 3: SEM micrographs of the irradiated AZO/Ag/AZO electrode. The laser irradiation is a single pulse, at wavelength of 1064 nm, with duration of 12 ns and energy fluence of 1.7 J/cm². (a) overview of the spot; (b) fracture of the multilayer structure at the periphery of the irradiated area; (c) central region and (d) AZO/Ag/AZO lift off from the substrate at the edge.

For comparison, cut tests on ~900 nm AZO film have been carried out under the same conditions. The obtained results clearly point out the need of an energy density higher than 4.6 J/cm² to perform the scribe in this case, and also very different surface morphology (just superficial crack) as shown in Fig.4.

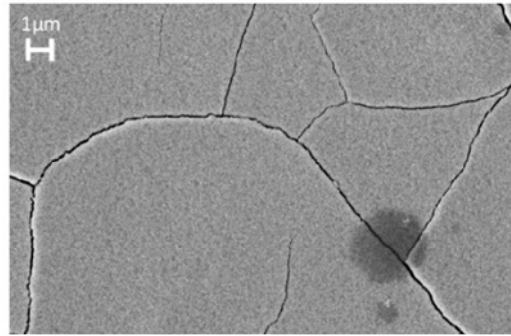


Figure 4: SEM images of ~900nm AZO layer irradiated at wavelength of 1064 nm, with a fluence of 4.6. J/cm². Fracture of AZO layer in the central region of the irradiated area are well visible.

The structural modification of the central area of the laser spot, on AZO/Ag/AZO structure, was confirmed by means of RBS technique. Figure 5 compares the energy spectra of He⁺ backscattered by AZO/Ag/AZO samples outside and inside the irradiated region shown in Fig.3(a). Three peaks are well distinguished in the as deposited multilayer structure. The one centered at 1.7 MeV is relative to He⁺ backscattered from Ag atoms, while the two peaks at 1.56 and 1.51 MeV are due to backscattering from the Zn atoms in the top and bottom AZO layers, respectively. Such a well-defined multilayer structure, present in the as deposited AZO/Ag/AZO, disappears after laser irradiation, showing that both Ag and Zn atoms are now located at the surface (Ag signal shifted towards higher energy). The smaller area of Ag and Zn peaks after laser irradiation also indicates that a partial removing of these materials has occurred, while the broader shape of the signals are related to the lost of the sharp multilayer structure. This will have a noticeable effect on the electrical properties, as discussed in the following paragraph.

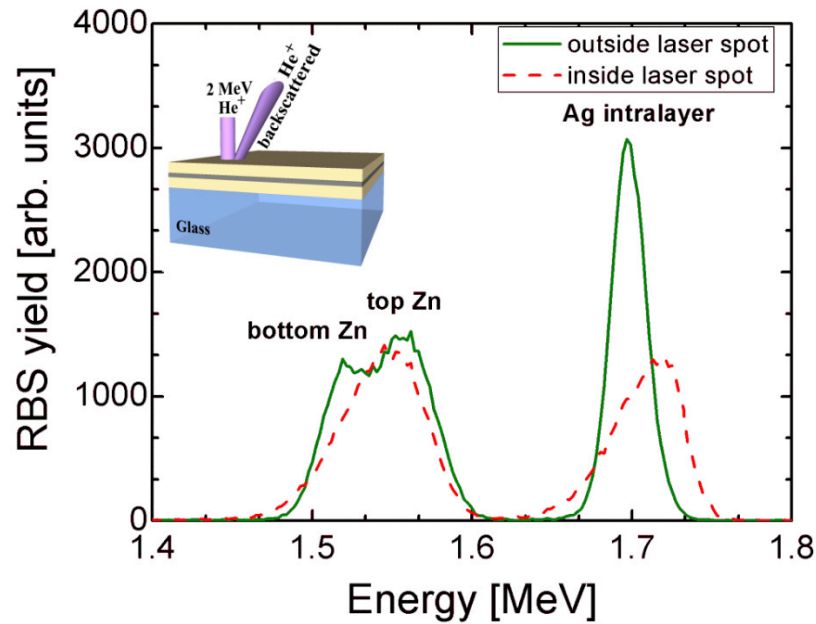


Figure 5: Energy spectra of He^+ backscattered by AZO/Ag/AZO sample outside and inside the irradiated area. A scheme of the RBS experimental set-up is reported in the inset.

4.2.2 Electrical insulation

The best monolithic series connection of solar cell module must exhibit a low series resistance and high shunt resistance in order not to jeopardize the conversion efficiency of the final module. Consequently, the P1 process, defining and isolating each cell of the module, to assure an electrical insulation must give an effective resistance of tens of megaohms [11]. The change of the conductivity due to laser ablation process has been mapped, using a Keithley 4200 semiconductor characterization system, by lateral current-voltage characteristics.

Figure 6 shows the separation resistance measured between two points, at a distance of 1.2 mm from each other, inside and across the laser spot, on our thin AZO/Ag/AZO sample irradiated with various laser fluences.

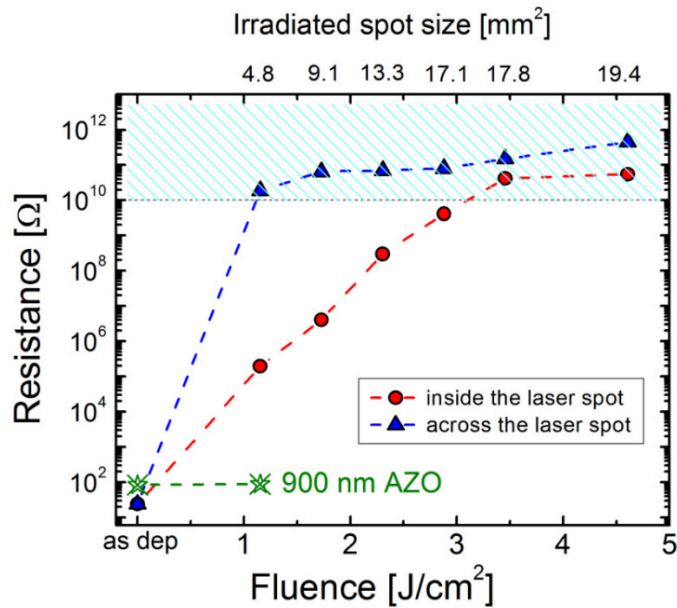


Figure 6: Dependence of the separation resistance on laser fluences. The irradiated spot size enlargement, evaluated through SEM imaging, is reported on the top x-axis. The cyan dashed area corresponds to the situation of excellent separation resistances (≥ 10 M Ω).

By increasing the pulse energy, the resistance measured inside the laser spot continuously increases up to saturation above 10 M Ω reached for fluence values higher than 3 J/cm² ensuring a complete electrical insulation. This is due to the more efficient ablation and damage of the film with the laser power, as also indicated by the spot area reported in the top x-axis scale. Most interestingly, the measured resistance values across the edge of the laser spot show an excellent insulation even at the lowest used beam fluence with an increase, respect to the as deposited multilayers, of more than eight orders of magnitude. Such high separation resistance is maintained also for higher laser fluences and can be attributed to the occurrence of the AZO/Ag/AZO laceration, as showed in Fig.3(b). Similar separation resistance was not observed in the case of a reference thick AZO layer, irradiated under

the same condition and included in Fig.6 for comparison. To understand how the separation resistance can be related to the laceration a further description of the AZO/Ag/AZO irradiation process is needed.

4.2.3 Heat transfer: model and analysis

The AZO/Ag/AZO removal process with ns pulse irradiation occurs in three consecutive steps: absorption of the laser energy at the transparent electrode/glass interface, temperature increasing of the irradiated area, fracture and damage of the continuous conductive multilayers. To better clarify the role of AZO and Ag thin film in the removal mechanism and accurately describe the P1 scribe, a thermal model was applied [12]. Although thermal modelling was earlier performed for various thin films on different substrates [8, 13-16] such a space-temporal model has not yet applied to the case of this multilayer structure. The basic sketch of the investigated structure is illustrated in the drawing of figure 2

The time-dependent temperature distribution, in the various layer of the irradiated multilayer structure is calculated according to the heat conduction equation:

$$\rho C_p \left(\frac{\delta T}{\delta t} + v_{rec} \nabla T \right) = \nabla \cdot (\kappa \nabla T) + \Sigma, \quad (1)$$

where ρ , C_p and κ are the mass density, the thermal capacity and the thermal conductivity of the material, respectively. The recession velocity, v_{rec} , is neglected in view of the relatively low laser fluences which are insufficient to heat the considered materials above the melting threshold and, thus, to initiate thermal vaporization [10]. The laser source term is given:

$$\Sigma = Q(x, y)(1 - R)\alpha e^{-\alpha z} f(t), \quad (2)$$

where α and R are the absorption and reflection coefficients of the materials, respectively. $Q(x,y)$ is the incident laser pulse intensity with a Gaussian spatial profile in xy -plane:

$$Q(x, y) = \frac{Q_0}{\pi\sigma_x\sigma_y} e^{-\left[\frac{-(x-x_0)^2}{2\left(\frac{\sigma_x}{3}\right)^2} - \frac{-(y-y_0)^2}{2\left(\frac{\sigma_y}{3}\right)^2} \right]} \quad (3)$$

where Q_0 is the maximum laser intensity centered in $P_0 = (x_0, y_0)$ at $t=0$, and $\sigma_x = \sigma_y$ the standard deviation of the spatial profile. $f(t)$, in Eq. (2), is the square-shaped pulse in the time domain:

$$f(t) = \begin{cases} 1 & 0 < t < 12\text{ns} \\ 0 & \text{otherwise} \end{cases} \quad (4)$$

Equation 1 is calculated for each layer of the structure using the material properties summarized in the following table 1. Therefore, taking into account that each material of the multilayer structure has different physical properties, the laser energy source absorbed in each layer will be different. The incident laser energy source enters through the glass, so the laser energy in the AZO layer is written as:

$$\Sigma = (1 - R_{\text{glass}})Q(x, y)(1 - R_{\text{b_AZO}})\alpha_{\text{b_AZO}}e^{-\alpha_{\text{glass}}\Delta z_{\text{glass}}}e^{-\alpha_{\text{b_AZO}}z}f(t), \quad (5)$$

where $\alpha_{\text{b_AZO}}$ and $R_{\text{b_AZO}}$ are the absorption and the reflection coefficient of bottom AZO, R_{glass} the reflection coefficient of the glass substrate, z is the

Parameters	Material	Value
Specific heat, C_p [J kg ⁻¹ K ⁻¹]	Glass	703
	Ag	240
	AZO	494
Density, ρ [g cm ⁻³]	Glass	2.2
	Ag	10.49
	AZO	5.7
Thermal conductivity, κ [W m ⁻¹ K ⁻¹]	Glass	0.80
	Ag	429
	AZO	20
Absorption coefficient, α [cm ⁻¹] (at 1064 nm)	Glass	0.5
	Ag	1.03x10 ⁵
	AZO	4x10 ³
Reflection coefficient, R (at 1064 nm)	Glass	0.04
	Ag	0.64
	AZO	0.01

Table 7: Material properties used in Eq. (1-7).

distance from the bottom of the glass and Δz_{glass} is the thickness of the glass substrate. The laser energy source, for the absorbing Ag thin film, is given by:

$$\Sigma = (1 - R_{\text{glass}})Q(x, y)(1 - R_{b_AZO})(1 - R_{Ag})\alpha_{Ag} e^{-\alpha_{Ag}(z - \Delta z_{\text{glass}} - \Delta z_{b_AZO})} * e^{-\alpha_{b_AZO}\Delta z_{b_AZO}} e^{-\alpha_{\text{glass}}\Delta z_{\text{glass}}} f(t) \quad (6)$$

Here α_{Ag} and R_{Ag} are the absorption and the reflection coefficient of silver, respectively, and ΔZ_{b_AZO} is the thickness of the bottom AZO layer hits by laser source. Similarly for the upper AZO layer, the energy source is:

$$\Sigma = (1 - R_{glass})Q(x, y)(1 - R_{b_AZO})(1 - R_{Ag})(1 - R_{u_AZO}) * \alpha_{u_AZO} e^{-\alpha_{u_AZO}(z - \Delta z_{glass} - \Delta z_{b_AZO} - \Delta z_{Ag})} e^{-\alpha_{b_AZO} \Delta z_{b_AZO}} e^{-\alpha_{Ag} \Delta z_{Ag}} e^{-\alpha_{glass} \Delta z_{glass}} f(t) \quad (7)$$

Here α_{u_AZO} and R_{u_AZO} are the absorption and the reflection coefficients of upper AZO layer and ΔZ_{Ag} is the thickness of Ag intralayer. Finally, the used model was a surface to surface model, integrating a free heat flow at the interfaces between the layers; moreover the overall stack made of the multilayer structure on glass substrate, is assumed to be at room temperature (293,15 K) and the energy density to be that which determines the lift-off process of the AZO/Ag/AZO structure.

Figure 7 shows the results of the simulations of the thermal process (in XZ-plane) on two samples irradiated with single pulse, at a wavelength of 1.064 nm, duration of 12 ns and the lowest fluence of 1,15 J/cm². The samples (both 90 nm thick on glass substrates) differ only for the presence of a 10-nm Ag mid-layer and are initially at room temperature. Interestingly, immediately after laser pulse, the maximum temperature reached in the multilayer structure is 150 K higher than that in the single AZO film, likely due to the higher absorption coefficient of the Ag at this wavelength. This is also indicated by the temperature distribution centered at the Ag depth in fig. 7(a) with respect to Fig.7(b), where the highest value is located at the surface of the AZO film. The same can be claimed by observing the space-temporal curves, reported in figures 7(c) and 7(d). Here, the green lines indicate the temperature values after 10 ns from the beginning of the laser pulse, and it is clear as the temperature is higher for the AZO/Ag/AZO sample and how the maximum value coincides with the Ag position, whereas this is not the case for the single AZO film.

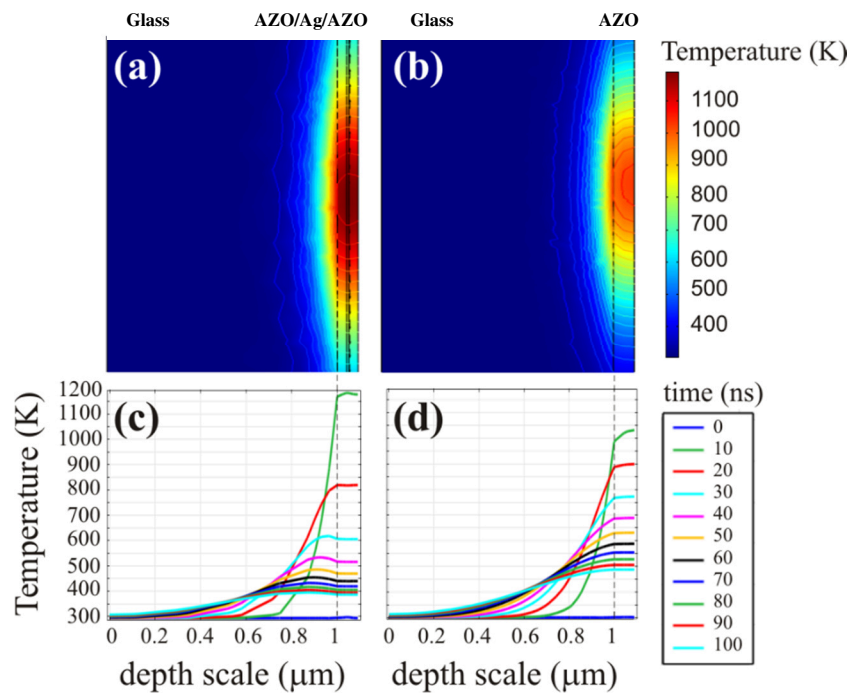


Figure 7: Simulations of the thermal process. Temperature distribution on 40 nm AZO/10 nm Ag/40 nm AZO on glass (a, and c); and on 90 nm AZO on glass (b, and d). The laser irradiation is a single pulse, at wavelength of 1064 nm, with duration of 12 ns and energy fluence of 1,15 J/cm².

In addition, the evolution of the temperatures with time is quite different for the two samples, with a faster cooling after the laser process for the multilayer sample. Such a behavior can be related to the higher thermal conductivity of Ag with respect to AZO. In addition, the simulations performed on a 10 times thicker AZO film show that the maximum temperature reached after the laser pulse is similar to the ultra thin AZO/Ag/AZO structure, but the cool down process is even slower. These observations indicate that a 10-nm thin Ag mid-layer affects greatly the heat flow during and after the laser irradiation, with noticeable effects on film removal thresholds. In fact, we experimentally observed that for

AZO/Ag/AZO thin film, a much lower laser energy fluence is required to induce the film cracking.

4.3 Conclusions

In this chapter we investigated the scribing process of ultra-thin AZO/Ag/AZO transparent electrode by a single nanosecond laser pulse.

We demonstrated that given a reduced pulse energy of $1,15 \text{ J/cm}^2$, the separation resistance of AZO/Ag/AZO is enhanced by 8 orders of magnitude compared to thicker AZO, currently used in thin film solar cell. In particular, the thermal behavior, simulated using a finite element approach, shows that the silver intralayer plays two key roles on the scribing process, by increasing the maximum temperature reached in the structure and fastening the cool down process. It is worth noting that, although only a partial ablation of the multilayer structure occurs at low laser fluence, the presence of the rip at the edge of the spot ensures an excellent electrical insulation, while such a morphology in standard TCO upon laser processing has never been reported to our knowledge. The presence of Ag has two main effects on the laser process: (1) higher temperature gradients and (2) different expansion and contraction of each layer during and after the irradiation, respectively. The latter point is a consequence not only of the first one (high thermal gradient between glass and film) but also of the difference in the thermal expansion coefficients of the materials: $18,9 \times 10^{-6}$, $4,75 \times 10^{-6}$ and $8,9 \times 10^{-6} \text{ K}^{-1}$ for Ag, AZO and soda lime, respectively. The substrate and coatings will expand differently upon the temperature change during the laser irradiation. As a result, thermally induced stresses are expected to arise. Because of the lower thermal expansion coefficient, AZO layers will suffer a reduced expansion with respect to the inner Ag film, and a compressive stress is then exerted by the inner layer on the outer layers which, after the thermal quenching, gives birth to the observed laceration.

Such results, in combination with its good electro-optical properties, clearly demonstrate that AZO/Ag/AZO transparent electrode is a suitable candidate for use in large-area modules, liable to segmentation, such as for a-Si:H solar panels, giving also large room for improvements for future high-efficiency-low cost thin solar cells.

References

- [1] Saga T., *NPG Asia Mater.* **2**, 96–102 (2010)
- [2] C. Dunsky. Laser processes in PV manufacturing: An update. *Industrial Laser Solutions for Manufacturing*, 2011.
- [3] C. Dunsky and F. Colleville, *Proc. SPIE* **6871**, 687129 (2008)
- [4] S. Lauzurica, J.J. García-Ballesteros, M. Colina, I. Sánchez-Aniorte, C. Molpeceres, *Appl. Surf. Sc.*, **257**, 5230–5236 (2011).
- [5] J. Hanak, US Patent US4292092, 29 Sept. 1981.
- [6] Compaan AD, Matulionis I, Nakade S, *Opt Laser Eng*, **34**, 15-45 (2000).
- [7] Bovatsek J, Tamhankar A, Patel RS, Bulgakova NM, Bonse, *Thin Solid Films*, **518**, 2897-2904 (2010).
- [8] Nakano S, Matsuoka T, Kiyama S, Kawata H, Nakamura N, Nakashima Y, Tsuda S, Nishiwaki H, Ohnishi M, Nagaoka I, Kuwano Y, *Jpn J Appl Phys*, **25**, 1936-1943 (1986).
- [9] Haas S, Gordijn A, Stiebig H, *Prog Photovolt Res Appl*, **16**, 195-203 (2008).
- [10] Crupi I, Boscarino S, Strano V, Mirabella S, Simone F, Terrasi A, *Thin Solid Films*, **520**, 4432-4435 (2012).
- [11] Hiroya Yamarin, Hidetada Tokioka, Mikio Yamamuka, US paten 20110108118 A1, 12 may. 2011.
- [12] Bulgakova NM, Bulgakov AV, Babich LP, *Appl Phys A*, **79**, 1323-1326 (2004).
- [13] A. Melnikov, H. Prima-Garcia, M. Lisowski, T. Giessel, R. Weber, R. Schmidt, C. Gahl, N.M. Bulgakova, M. Weinelt, *Phys. Rev. Lett.*, **100**, 107202 (2008).
- [14] Y.P. Meshcheryakov, N.M. Bulgakova, *Appl. Phys. A*, **82**, 363 (2006)
- [15] J. Hermann, M. Benfarah, S. Bruneau, E. Axente, G. Coustillier, T. Itina, J.F. Guillemoles, P. Alloncle, *J. Phys. D* **39**, 453 (2006)
- [16] R. Fardel, M. Nagel, T. Lippert, F. Nuesch, A. Wokaun, B.S. Lukyanchuk, *Appl. Phys. A* **90**, 661 (2008)

Appendix

In this last part of the thesis, the experimental methods for the growth, processing and characterization of our transparent electrodes are described.

The first paragraph of this appendix is devoted to the physical vapor deposition (PVD) technique, i.e. radio-frequency magnetron sputtering, and the experimental setup employed to make AZO, ITO, Ag thin films and also the multilayer structure TCO/metal/TCO. Additionally, the thermal treatment (post deposition) and laser system used to process transparent electrodes are described in paragraph 2.

The last part of the appendix covers the experimental characterization techniques used in my work to assess the quality of the transparent electrodes. Measurements can be roughly divided into two categories: structural and electro-optical characterization.

1. Radio-Frequency Magnetron Sputtering

Many techniques are used to deposit TCO thin-films, including metal-organic chemical vapor deposition (MOCVD), sol-gel processing, evaporation, pulsed laser deposition (PLD), molecular beam epitaxy, chemical spray technique, DC and RF magnetron sputtering [1]. The latter presents some advantages in comparison to the other methods. The RF magnetron sputtering is a quite simple technique and it is considered the most available deposition method to obtain highly uniform films with a reasonable quality and strong adhesion at a high deposition rate. In addition, sputtering process is well suited to industrial-scale and large-area deposition for application in photovoltaic devices [1]. The sputtering is a physical vapor deposition (PVD) process used to deposit thin films, by ejecting atoms from the surface of a material (the target) by bombardment with energetic ions. The sputtered atoms travel until they deposit onto the substrate, in high vacuum environment, to form the desired thin film layer. Figure 1 shows a schematic diagram of the RF magnetron sputtering system used in this work.

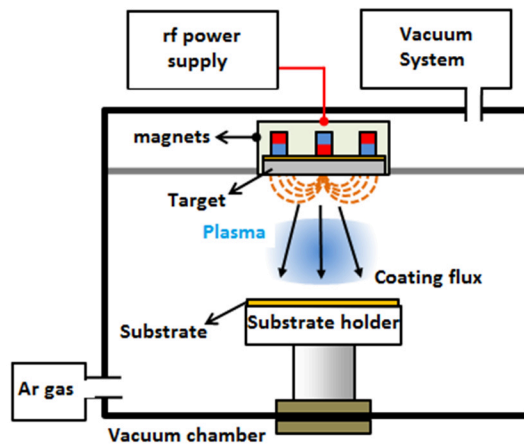


Figure 41: Schematic diagram of a magnetron sputtering system.

The simplest source of ions for sputtering is provided by the well-known phenomenon of the glow discharge. The glow discharge is initiated by applying a power between the target (cathode) and substrate (anode) in a controlled gas atmosphere, and it is formed of a partially ionized gas (known as plasma) of ions, electrons, and neutral species. Ions of the plasma are accelerated at the target by a large electric field and when their energy is greater than the surface binding energy, atoms (or molecules) are ejected from the surface of the target into the plasma, where they are carried away and then deposited on the substrate. This type of sputtering is called direct current (DC) sputtering. In order to avoid any chemical reaction between the sputtered atoms and the sputtering gas, this one is usually an inert gas such as argon (Ar).

If the target is an insulator, the use of a radio frequency (*RF*) generator is essential to maintain the discharge and to avoid charge build-up that can repel the ionic bombardment and stop the sputtering process. This type of sputtering is known as “*RF sputtering*”. The *RF* excitation mode is much more effective compared to the DC mode, and is suitable for both conducting and insulating targets.

Magnets are used to enhance ejected atoms from the target, by increasing the ionizing effect of electrons magnetically trapped in the vicinity of the target. Their use provides the advantage of trapping not only electrons, but also charged species at the target, so that they do not hit the substrate, with an improvement of the film quality. This type of sputtering is called “*magnetron sputtering*” and it can be used with DC or *RF* sputtering.

In this thesis, AZO, ITO, Ag and TCO/Ag/TCO thin films have been synthesized on glass and plastic substrate by *RF* magnetron sputtering technique using the experimental setup, placed at the Department of Physics and Astronomy of Catania, shown in Fig.2

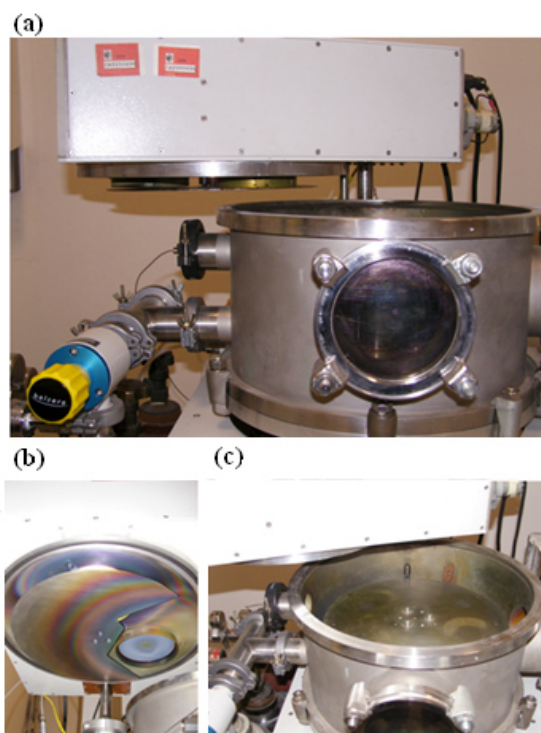


Figure 42: RF magnetron sputtering experimental set up. (a) overview of the chamber and head of the sputtering system, (b) a target and shutter window mounted in the head, (c) Spinning substrate holder.

The used system consists of a sputter chamber where, by means of a vacuum pumping system composed of a rotary pump and a turbomolecular pump, high vacuum is established. A minimum of 8×10^{-6} mbar pressure is reached prior to the deposition. High purity (99.99 %) gases, such as Ar, O₂, and N₂, are delivered from the high-pressure gas lines via rotameters, control system and mass flow meters into the chamber. The manual control of the mass flow meter, of each gas, allows to reach a total working pressure of 1×10^{-2} mbar. The sputtering system is set up with the configuration of substrates under the target, where the distance from target to substrate is 7 cm.

In the sputter chamber, three targets (4-inch in size) of ITO (purity 99,99%, composition 10 wt% SnO₂-90 wt% In₂O₃), AZO (purity 99,99 %, composition 2 wt% Al₂O₃ -98 wt% ZnO) and Ag (purity 99,99 %) are installed on the cathodes, which house permanent magnets for directing charged particles of the plasma, while the samples are put on the water-cooled substrate holder (anode). The power is supplied by a RF generator, with an available power in the range of 0-550 Watt and operating at a frequency of 13.56 MHz, which is connected to the cathode through an impedance matching network with variable capacitors. The manual controls allow the operator to tune the capacitive coupling to reduce the RF reverse power to almost zero. TCO/Ag/TCO multilayers, were sequentially deposited on the substrates by a rotating substrate holder and without vacuum break.

The substrates were first cleaned in acetone, rinsed in deionised water and in absolute ethanol, then placed onto the substrate holder. The sputtering system is also set up with a heater system composed of a high melting point metallic (tungsten, molybdenum or tantalum) crucible molds in order to contain the sample. The latter can warm up to 700 °C by Joule effect. The extremities of the crucible are connected to a high current DC power supply. The substrate temperatures were calibrated by pressing a thermocouple against the surface of the holder (crucible). In this case the distance between target and substrate is 4 cm.

2. Post deposition processes

In this section we illustrate the equipments employed to modify the structural, optical and electrical properties of transparent electrodes after their deposition: (ion implantation, thermal annealing and laser ablation).

2.1 Thermal treatment

Transparent electrodes have been thermally treated at temperatures ranging from 200 to 500 °C, for different annealing times and in N₂ atmosphere by using a conventional horizontal furnace.

The Carbolite horizontal furnace, shown in Fig. 3, is equipped with an Al₂O₃ tube (75mm internal diameter, 150 cm long) and a pre-chamber for the introduction of one or more samples loaded into a floating quartz boat (4 cm x 9 cm). The pre-chamber is separated from the heated zone by a high vacuum valve so that the furnace tube is kept always under vacuum during the sample loading. Once the pre-chamber has been pumped down to a few

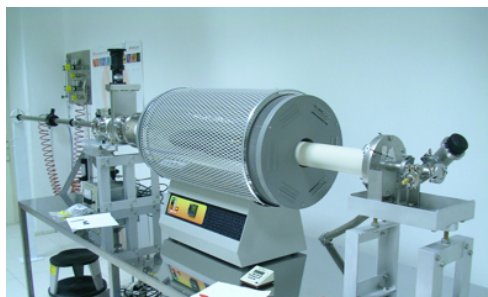


Figure 43: Carbolite horizontal furnace STF 15/75/450.

mbar pressure, the separation valve is open and the quartz boat with the samples can be moved into the central region of the furnace where the temperature is uniform. The floating boat allows a rapid introduction of the samples even when the furnace temperature is as high as 1200°C, preventing the damage which usually occurs when the boat sample holder drags the Al₂O₃ tube. The furnace can reach a max temperature of 1500°C and it is equipped with 3 independent gas lines: N₂, O₂ and Ar or forming gas. The furnace tube is sealed with O-ring viton gaskets which can hold a vacuum of at least 10⁻⁵ mbar. Our thermal processes are performed in N₂ gas flow at nearly atmospheric pressure, with the over pressure controlled by a one-way exhaust valve. Gas flow is controlled by manual flow meter in the range 0-20 lpm, with an accuracy of about 0.25 lpm. Thermal treatment parameters such as thermal treatment time, final temperature and rate of the temperature can be set by a control panel.

2.2 Laser ablation

The laser mainly used in this study is a Newport Quanta-Ray Pro-Series pulsed Nd:YAG laser. The single pulse width is ~10ns and the maximum energy ($\lambda=1064\text{nm}$) is 1.25 J/p. The energy is tunable by a continuously variable beamsplitter and the laser irradiation is performed in atmosphere. The spatial profile is Gaussian with a FWHM of 3mm. The laser head comprises both a Beam-loc and a D-loc system to control accurately the position ($<25\mu\text{rad}$) and the divergence ($<1\text{mrad}$) of the beam. The highest repetition rate is 10Hz but is possible to increase the time lapse between the pulses. The energy stability is always higher than 5% between different pulses. The system is also equipped with a harmonic generator and then we can operate with different wavelengths: 1064 nm, 532 nm, 355 nm.

2.3 Ion implantation

Ion beam based techniques are a powerful tool to introduce ions in a designated local area of the thin films with an excellent controllability and, so, to modify their structural, optical and electrical properties [2, 3].

Ion implantation processes have been done by 400 kV HVEE Ion Implanter that has a Cockroft-Walton multiplier voltage generator and the terminal voltage is in the range 10-400 kV in order to be able to implant into the samples over a wide range of ion energies. It is possible to use two different source type (gas or solid) in order to implant the following elements:

- B, Na, Al, P, Mn, Fe, Co, Ni, Cu, Zn, Ga, Ge, As, In, Sn, Sb, Te, Er, Au, Bi by hot cathode source.
- H, He, C, N, O, Ne, Ar, Kr, Xe by cold cathode source.

In ion implantation, dopant atoms are volatilized, ionized, accelerated, separated by the mass-to-charge ratios, and directed at a target. The ion implantation system is schematically shown in Fig. 4(a).

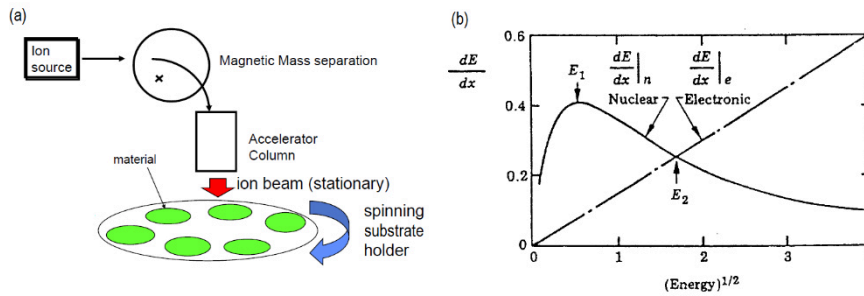


Figure 44: (a) schematic sketch of ion implantation system, (b) Rate of energy loss dE/dx versus $E^{1/2}$, showing electronic and nuclear loss contributions

The atoms enter into the crystal lattice, collide with the host atoms, lose energy and finally come to rest at some depth (projected range) within the solid. Moreover, the passage of an energetic ion through the lattice initiates a sequence of displacement events that produce defects within the crystal (vacancy, interstitial atoms, etc.). Ions within the material lose energy by two different stopping mechanisms, Fig. 4(b): electronic collisions that dominate at high energies and nuclear collisions that dominate at low energies. The average penetration depth depends on the incoming ions, substrate materials, and acceleration energy. In this study this parameter was determined for Ar^+ and O^+ ions on Al:ZnO substrate by SRIM simulation software [4]. Ion implantation energies range from 30 KeV to 350 KeV, resulting in ion distributions with average depths from between ~30 nm and ~750 nm.

The total number of ions entering in the target is called the dose or fluence. If the current in the ion beam is I , then for a beam swept over an area A (circle of 2 inches of diameter), the dose, Φ [ions/cm²], is given by:

$$\Phi = \frac{(ion\ beam\ current\ in\ amps / q) \times (implant\ time)}{ion\ beam\ scanning\ area} \quad (1)$$

For an accurate assessment of the current, it is imperative that secondary electrons emitted from the target must be recaptured. This is done by using a small positive bias around the Faraday cup cage.

3. Characterization techniques

In this section, the discussion is limited to the methods used in this thesis for characterizing structural, optical and electrical properties in single layer of transparent conductive oxides as well as TCO/Ag/TCO multilayer structures. The equipments and methods will be briefly described.

3.1 X-Ray Diffraction (XRD)

X-ray diffraction (XRD) is a powerful non-destructive diagnostic tool in analyzing the crystal structure of unknown material and determining the structural properties of this one such as the average spacings between layers or rows of atoms, the orientation of a single crystal or grain, and the size, shape and internal stress of small crystalline region [5,6].

A real three-dimensional crystal is a regular arrays of atoms, where the atoms are arranged in atomic planes spaced at a distance d from each other. An atomic plane can be distinguished by its Miller indices (hkl) , and the distance between 2 adjacent (hkl) planes is denoted by d_{hkl} . When X-rays irradiate the surface of the crystal they are scattered by these atomic planes. As a result, there will be a destructive or constructive interference from the specular reflectance of X-rays as a function of the values of d_{hkl} and the angle of incidence θ_{hkl} onto the (hkl) planes, resulting in a diffraction pattern, as depict in Fig.5.

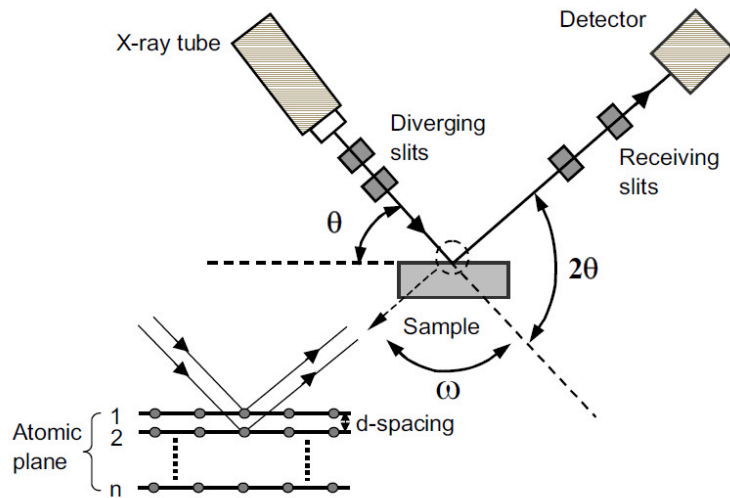


Figure 45: Schematic representation X-ray diffractometer for measurement of the crystal materials

X-rays are used to produce the diffraction pattern because their wavelength is typically the same order of magnitude (1–100 Å) of the distance between planes in the crystal. The condition for constructive interference occurs only when Bragg's Law is satisfied [7]:

$$n\lambda = 2d_{hkl} \sin \Theta_{hkl} \quad (2)$$

where the integer number n is the "order" of reflection and λ is the X-ray wavelength. For diffraction to be observed, the angle between the surface of the sample and the incident X-rays must be at the Bragg angle Θ_{hkl} , and the reflected intensity is measured by detector as a function of $2\Theta_{hkl}$. In this case, X-rays are incident on the samples over a range of angles Θ , while reflections are detected over the range of angles 2Θ . This XRD scan mode is known as the Θ - 2Θ scans. Because the positions of the peaks generated in a pattern, in a typical XRD analysis, are determined by the size, shape, and symmetry of the unit cell, and the peak intensities are determined by the arrangement of

atoms within the cell, the pattern is a unique “fingerprint” of a phase. When properly interpreted by comparison with standard reference patterns and measurements, this fingerprint allows identification of the crystalline form. Moreover, the widths, shapes and positions of the peaks in a pattern are determined by many factors, including contributions both from the diffractometer and the specimen such as internal strain and grain size domain. Once the instrumental factors are understood by measuring a sample having no size or strain broadening, the crystallite size and strain can be determined from the experimental peaks.

The full width at half maximum (FWHM) of an XRD diffraction peak in a θ - 2θ scan is related to the average crystallite size in the samples. We can then work backward, and compute the average crystallite size from the observed peak widths. In particular, the equation relating the FWHM of a diffraction peak to the average dimension D of crystallites in the direction perpendicular to the substrate surface, known as Scherrer formula [8], is given by:

$$D = k \frac{\lambda}{W \cos \theta} \quad (3)$$

where λ is the X-ray wavelength, W is the FWHM in radians, θ is the peak position in degrees and k is a dimensionless shape factor, with a value close to unity. The shape factor has a typical value of about 0.9, but varies with the shape of the crystallite. The size D is effectively an average coherence length of the crystal structure, it is not necessarily a measured size of an entire grain since defects, because dislocations in the lattice structure, may divide each grain into sub-grains, or crystallites, and result in a value of D which is far smaller than the average grain dimensions measured by structural techniques such as TEM, SEM or AFM.

As far as the strain is concerned, it is the result of small changes of the lattice parameters (a , b and c) of the structure, due to defects and impurities. In the XRD analysis the strain is related to peaks positions,

therefore a shift of the peaks positions to smaller or higher 2θ values compared to standard reference free-strain material, indicates the presence of strain. In particular, in chapter 2, XRD measurements are used to determine the structural properties of AZO thin-films, which were all polycrystalline thin-films with a hexagonal wurtzite ZnO structure and preferentially grown along the ZnO 002 axis (c-axis) of the crystal. In the hexagonal structure the plane d_{hkl} is related to Miller indices (hkl) by [9]:

$$d_{hkl}^2 = \left(\frac{4(h^2 + k^2 + hk)}{3a^2} + \frac{l^2}{c^2} \right)^{-1} \quad (4)$$

where $a=b$ and c are the lattice constants of the structure, and d_{hkl} is the crystalline plane distance for indices (hkl). According to the eq. 4, the lattice constant c is equal to $2d_{002}$ for the (002) diffraction peak. Therefore, a shift on the peak position means a change in the d_{hkl} value (compared with the standard reference) and in turn a change in the c value. It allows to measure the strain ϵ along the c -axis in the thin films by means of:

$$\epsilon = \frac{c_{film} - c_{bulk}}{c_{bulk}} \quad (5)$$

where c_{film} and c_{bulk} are the value measured and the unstrained lattice parameter value (0.5207 nm [1]).

X-ray diffraction analyses (0-2 θ scans), in this thesis, were performed by using a D8Discover Bruker-AXS diffractometer equipped with a Cu α radiation source ($\lambda=1.54056 \text{ \AA}$) and long soller slits, and used to investigate lattice structure, strain, texture and domain diameter of the AZO layers grown/treated in different conditions. The machine was typically operated at a voltage of 40 kV and current of 40 mA. A standard setting for continuous scans is at an angular speed of 1-5 sec/step and a step size of 0.02° in a 2θ range of $20-40^\circ$. Quantification of peak full width at half maximum (FWHM)

value of peak density and 2Θ peak position was performed using a Bruker EVA software.

3.2 Rutherford Back-scattering Spectrometry (RBS)

Rutherford Backscattering Spectrometry (RBS) is a widely used nuclear method for the near surface layer analysis of solids which allows the quantitative evaluation of the composition of a material and depth profiling of individual elements. RBS is based on the physical principle that an ion beam is directed to the surface of a sample, enters in the sample, scatters on atomic nuclei and travels back out to be detected, showing an energy distribution. Since ion-target atom interaction can be described by a two body elastic collision governed by Coulomb repulsion, measuring the number and energy of the backscattered ions after the collision with atoms in the near-surface region of a sample, it is possible to determine atomic mass and elemental concentrations versus depth below the surface.

If a particle of mass M_1 , Fig.6, is scattered from the electrical field of nucleus of a mass M_2 at angle Θ (laboratory system), applying the principles of conservation of energy and momentum, the resulting energy E_1 , is K-part of initial energy, E_0 :

$$E_1 = K E_0 \quad (6)$$

in this formula, K is defined as the kinematic factor. K depends only on the mass ratio M_2/M_1 and the scattering angle Θ as described in the following equation [10]:

$$K = \frac{M_1^2}{(M_1 - M_2)^2} \left\{ \cos \Theta \pm \left[\left(\frac{M_2}{M_1} \right)^2 - \sin^2 \Theta \right]^{1/2} \right\}^2 \quad (7)$$

only the positive sign is considered for $M_1 < M_2$. In case $M_1 > M_2$, eq. 7 has two solutions and the maximum possible scattering angle Θ_{\max} is given by $\Theta_{\max} = \arcsin(M_2/M_1)$.

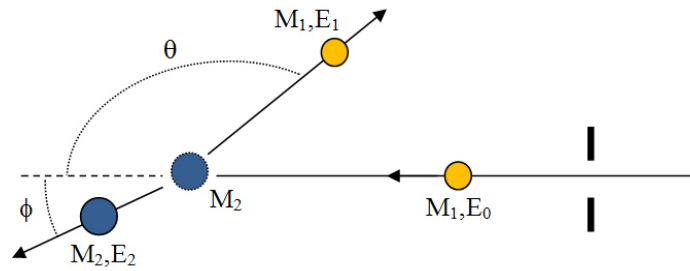


Figure 46: Schematic of an classic collision and backscattering of a projectile of mass M_1 and energy E_0 with a target particle of mass M_2 , initially at rest in the laboratory.

The mass resolution can be derived from equations (6) and (7). If two different target elements with mass difference ΔM_2 are present, the energy separation ΔE_1 of particles backscattered from the two masses is given by:

$\Delta E_1 = E_0 \frac{dK}{dM_2} \Delta M_2$. Then the mass resolution is:

$$\frac{M_2}{\Delta M_2} = \frac{E}{\Delta E} \frac{A + \sin^2 \Theta - \cos \Theta \sqrt{A^2 - \sin^2 \Theta}}{A^2 - \sin^2 \Theta + \cos \Theta \sqrt{A^2 - \sin^2 \Theta}} \quad (8)$$

where ΔE is the energy separation and $A=M_2/M_1$. From eq. 8, the mass resolution is best for large scattering angles and A about the unity. In practice, light ions (typically He^+) and scattering angles very close to 180° are preferred in RBS analysis because mass discrimination is largest when Θ is close to this angle and for solid state detectors the optimum mass resolution is obtained for ions with mass M_1 in the range 4–7 a.m.u.

When an ion is backscattered inside the material, its final energy is determined by the elastic nuclear collision at a certain depth of the sample and the additional inelastic energy loss due to electrons collision during its way in and out of the material. The deeper the probe ion is backscattered inside the material, the more remarkable is its total energy loss. Here we are interested in the energy loss per unit of length dE/dx (in $\text{eV}/\text{\AA}$), defined as the stopping power. Since the density of the thin film is systematically

uncertain, in RBS analysis we use the stopping cross-section ϵ instead of the stopping power, given by:

$$\epsilon(E) = \frac{1}{N} \frac{dE}{dx} \quad (9)$$

The stopping cross-section ϵ is generally expressed in eV/($\times 10^{15}$ at/cm²).

We consider the energy variation Δ of a sample of thickness t as $\Delta = KE_0 - E_2$, where E_0 and E_2 are the initial energy of the ion and the measured final energy, respectively, for a scattering event occurs at a depth t , K is the kinematic factor defined in eq. 7, Fig. 7. Assuming a constant energy loss for the ion during the path of entry and exit from the surface, we can find the expression:

$$\Delta = [\epsilon] \cdot N t \quad (10)$$

where t is expressed in ($\times 10^{15}$ at/cm²) and the stopping cross-section factor $[\epsilon]$ is given by:

$$[\epsilon] = \frac{K\epsilon(E_0)}{\cos \Theta_{in}} + \frac{\epsilon(E_0)}{\cos \Theta_{out}} \quad (11)$$

In Eq. 11, Θ_{in} and Θ_{out} are the incident and exit angles, respectively, with respect to the surface normal. Δ is proportional to the areal density Nt of the target traversed by the beam before backscattering and, therefore, it provides a measure of backscattering depth beneath the surface. After the elements identification are identified, the thickness of the film can be calculated by using the provided tables to look up $\epsilon(E)$ for the a specific element and from Δ . Moreover, the calculation of element concentrations and thicknesses by RBS depends from the scattering cross section of the element of interest and the stopping cross section of the sample matrix. The scattering and stopping cross sections for each element have been carefully

measured and tabulated. In general, scattering cross sections follow the Rutherford scattering model within 5% of errors.

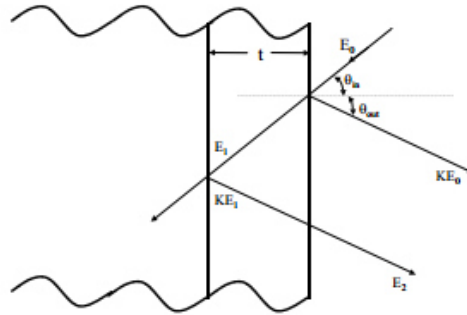


Figure 47: Components of energy loss for an ion beam that scatters from depth t .

During the last two decades several computer codes for the simulation and data evaluation of RBS spectra have been developed. These codes are spectrum simulators, i.e. they calculate a spectrum for a given target structure and allow fitting of target compositions to measured spectra.

RBS, extensively used in this work to characterize the structural properties of the transparent electrodes, have been performed using an HVEE coaxial Cockroft–Walton Singletron accelerator with maximum terminal voltage of 3.5 MV. The beam spot size is in the range of 1-3 mm², the typical current is 50 nA. In particular, standard RBS analysis with a 2 MeV ⁴He⁺ beam has been used to check the composition of the grown TCO thin films and to determine their thickness. The scattering geometry was the IBM one and it is referred to the scattering configuration where the incident beam, the surface normal, and the detected beam are all coplanar. For 2 MeV He⁺ RBS analyses the scattering angle Θ is 165°, the detector has an active area of 30 mm² and it is placed at about 10 cm from the target. RBS in high energetic resolution (glancing detection) mode was employed in TCO/Ag/TCO films to check the composition and to determine the thicknesses of the TCO layers and of the Ag film embedded within. A 2.0 MeV He⁺ ion beam hits the sample surface at normal incidence, while

backscattered He atoms are detected at an angle of 106° from the beam axis. The overall energy resolution and the glancing detection mode allowed to distinguish between the top and bottom TCO layers and to check the broadening of Ag or TCO profiles after thermal or laser annealing, if any. Once Ag, Zn and In doses have been quantified in Ag, AZO and ITO thin films, respectively, the layer thickness is derived by assuming a proper atomic density: 5.84×10^{22} Ag/cm³, 4.22×10^{22} Zn/cm³ for AZO, 2.58×10^{22} In/cm³ for ITO. Simulation and data evaluation of RBS spectra have been performed by RUMP [11, 12] or SIMNRA [4] softwares.

3.3 Scanning Electron Microscopy (SEM)

Scanning Electron Microscopy (SEM) is a very powerful technique for non-destructive high-resolution topological analysis of surfaces and cross-section of samples. In a scanning electron microscope, a tiny electron beam is scanned across the sample. Simultaneously, the generated signals are being recorded and an image is formed pixel by pixel [13]. The main SEM components, Fig. 8(a), include:

- Source of electrons
- Column down which electrons travel with electromagnetic lenses
- Electron detector
- Sample chamber
- Computer and display to view the images

Electrons are produced at the top of the column by cold field-emission cathode, accelerated down and passed through a combination of lenses and apertures to produce a focused beam of electrons which hits the surface of the sample. The sample is mounted on a moving stage in the chamber area evacuated by a pump system to vacuum value belows 10^{-5} mbar (less than 10^{-10} mbar in the gun zone). By means of a scan coils, situated above the objective lens, the position of the electron beam on the sample is controlled, allowing to the beam the scanning of the sample's surface. When the beam's

electrons hit the surface of the sample, they penetrate until to depth that depends on the accelerating voltage and the density of the sample. As a result of the electron-sample interaction, Fig. 8(b), different type of signals are produced: backscattered, secondary and Auger electrons as well as X-ray. Each of these signals are then detected by appropriate detectors and they get specific information about topography (Primary backscattered and secondary electrons), surface characteristics (Auger electrons), specimen composition (X-rays) [13].

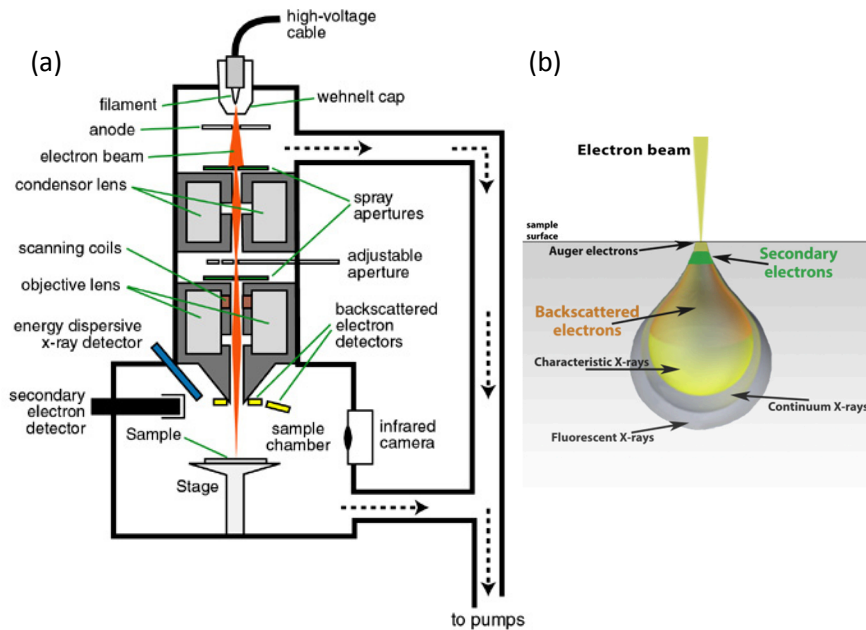


Figure 48: (a) schematic diagram of SEM, (b) the tear-drop model of the electron interaction volume and the volume/depth from which the different signals originate.

In this thesis, a Gemini Field Emission SEM (FE-SEM) Carl Zeiss SUPRA™ 25 was employed to determine the surface morphology of TCOs and TCO/metal/TCO thin-films in Chapters 3 and 4. SEM is equipped with a field-

emission gun, a secondary electron detectors, a backscatter detector and also EDAX EDX detector and a Gemini multi-mode STEM detection system. The instrument typically operates with electron beams in the 0.5-20 keV range, and magnifications from 12x to more than 500,000x are available. With this apparatus we can obtain topological information with a resolution ranging from 1.7 to 3.5 nm for surfaces analyses @ 15 keV and 1keV, respectively, and it is possible to obtain a complete compositional characterization by using the EDX detector.

3.4 Atomic Force Microscopy (AFM)

The samples structure and morphology were also investigated by atomic force microscopy (AFM) technique. AFM in surface science is used to obtain three-dimensional high-spatial resolution real-space images of the sample's surface on nanoscale, by measuring the force between a probe sharp tip and the surface of the sample [14].

Usually, to acquire the image AFM employs, Fig. 9, a probe formed by flexible reflective cantilever with a sharp integrated tip (at the end and underside) along with optical detection system formed by a diode laser and a photodetector. The laser is focused onto the back of the reflective cantilever and when the tip scans the surface of the sample, moving up and down with the contour of surface, the laser beam is deflected off the attached cantilever into the distant photodetector.

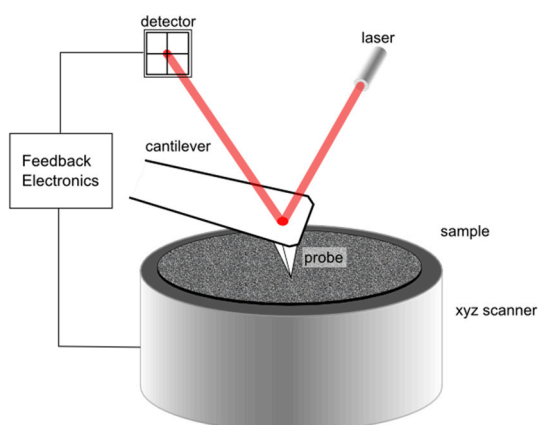


Figure 49: Schematic of AFM operation.

The movement of the laser spot on the photodetector gives measures the vertical deflection of the

cantilever, which indicates the local sample height. This set-up is known as an optical lever. The measured cantilever deflections are used to generate a map of the surface topography. The motion of the probe over the surface is controlled by using feedback loop and piezoelectronic scanners. The piezoelectronic scanners moves the probe very precisely in the x, y, and z axes, while a signal from the photodetector passes through a feedback circuit, and into the z-movement part of the scanner, in order to maintain the distance between probe and sample at a set value.

The most commonly used modes of operation of an AFM are contact mode, tapping mode and non-contact mode. In contact mode, the force on the tip is repulsive (Van der Waals interactions) and the tip “gently” touches the surface. By maintaining a constant cantilever deflection the force between the probe and the sample remains constant and an image of the surface is obtained during the tip scanning. In non-contact mode, the force on the tip is attractive (Van der Waals interactions) and tip does not contact the sample surface but oscillates above it. Topographic images can be measured by using a feedback loop to monitor changes in the amplitude due to the force. In tapping mode operates the cantilever oscillates at its resonant frequency and by maintaining a constant oscillation amplitude along with constant tip-sample interaction an image of the surface can be obtained. Once images are acquired, a wide variety of analysis functions are available in the analyzing menu of equipment such as 2D or 3D images and quantitative measurements like root-mean-square (RMS) variation of the surface height profile [14].

Atomic Force Microscopy performed by a Veeco-Innova microscope operating in high amplitude mode was used to record surface topography Al:ZnO thin films in Chapter 2. The images were taken in the contact mode with Ultra-sharpened Si tips (MSNL-10 from Veeco Instruments, with anisotropic geometry, radius of curvature ~2 nm, tip height ~2.5 μm , front angle ~15°, back angle ~25°, side angle ~22.5°) and scan frequency of 0.5 Hz. Collected data consisted of height information on square 1 μm x 1 μm . Two-dimensional (2D) and three-dimensional (3D) images were created and analyzed by SpmLab Analysis V.7.1. By this data processing software package

it was also allowed to extract detailed surface roughness. The roughness, σ , (root-mean-square (RMS) variation of the surface height profile) evaluated using the SPMLabAnalyses V7.00 software it is defined by:

$$\sigma = \left[\frac{1}{N} \sum_{i=1}^N (y_i - \bar{y})^2 \right]^{1/2} \quad (12)$$

where N is the number of data points of the profile, y_i are the data points that describe the relative vertical height of the surface, and \bar{y} is the mean height of the surface. Furthermore, the roughness value was obtained averaging the values obtained over three different images (square $5 \mu\text{m} \times 5 \mu\text{m}$, square $1 \mu\text{m} \times 1 \mu\text{m}$, square $0.5 \mu\text{m} \times 0.5 \mu\text{m}$).

3.5 UV/VIS-NIR spectroscopy

The transmission and the reflection spectra of the transparent electrodes (Chapters 2, 3 and 4) were measured from UV to near-IR region to obtain optical properties such as absorbance, absorption coefficient and optical bandgap.

When light passes through or is reflected from a sample, transmittance, T, is defined as the ratio between the intensity of transmitted radiation (I_T) and the incident radiation (I_0), while reflectance, R, is expressed as the fraction between the intensity of reflected radiation (I_R) and the incident radiation (I_0).

$$T = \frac{I_T}{I_0} \quad R = \frac{I_R}{I_0} \quad (13)$$

Transmittance and reflectance usually are given in terms of a fraction of 1 or as a percentage. A Varian Cary 500 double beam (sampling and a reference beam) UV-VIS-NIR spectrophotometer was used to measure T and R spectra. Figure 10 shows a schematic of the spectrophotometer, which is equipped

with two monochromators (1200 lines/mm and 300 lines/mm). The principal advantage coming from the presence of two monochromators is the possibility to minimize photometric noise and stray light, providing excellent resolution $\Delta T/T=1.4 \times 10^{-3}$, while the double beam not allows to avoid an effect on the measurement results, because a reference signal is constantly taken throughout the scan and the final measured value does not rely on a previously measured reference scan.

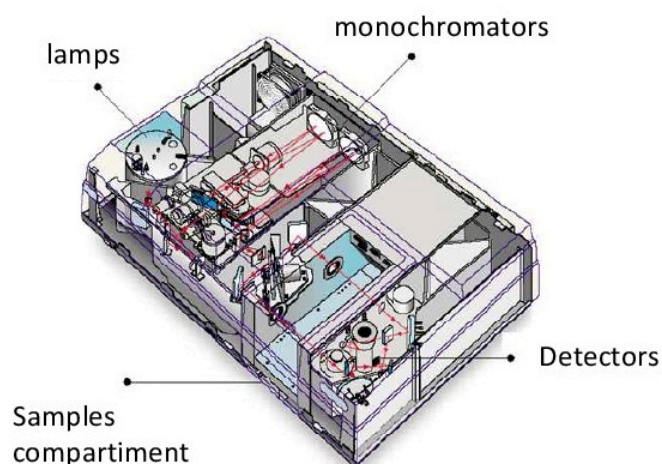


Figure 50: Schematic of Varian Cary 500 double scanning UV-VIS-NIR spectrophotometer.

The Varian spectrophotometer uses a tungsten halogen lamp in the visible and near-infrared region of the probe wavelengths while a deuterium lamp in the ultraviolet region. An automated carousel swaps the lamps at a specified wavelength of 350 nm. The light beam passing through the sample or along the reference beam path is detected by a photomultiplier tube R928 in the UV/Vis region and a lead sulphide detector in the NIR. The detectors are changed in unison with the gratings, at a wavelength which can be fixed in the range from 800 to 860 nm. A change of diffraction grating/detector at about 800 nm was used in this work. As a result, in the measured

transmission and the reflection spectra, a small discontinuity of the collected data appeared in the vicinity of this wavelength. A modular Windows-based software, makes it easy to perform powerful analysis and control a number of optional accessories.

Transmission and the reflection spectra of the transparent electrodes were measured at room temperature and in the wavelength range 300 – 2000 nm with a scan rate and wavelength interval of 600nm/min and 1 nm respectively. To ensure stabilized measurement conditions, before R and T measurement can be performed, the spectrophotometer was left half hour to warm-up, then baseline calibration was carried out. More precisely, direct transmittance (T_{direct}) spectra were collected with a 100% baseline (I_b) obtained mounting the empty sample holder, while the reflectance ($R_{spec.}$) spectra were detected in specular geometry using a calibrated standard. Specular reflectance refers to the part of the incident beam reflected at the same angle as the angle of incidence (20°) and, moreover, a polished FZ-Si wafer (R_{Si}) was used as a reference for measurements. The normalized transmittance and reflectance spectra are given by:

$$T_{direct} = \frac{I_T}{I_b} \quad ; \quad R_{spec.} = (I_R - R_V) \frac{R_{Si-th}}{(R_{Si} - R_V)} \quad (14)$$

where I_T , I_R , R_{Si-th} and R_V are the intensity of transmitted radiation and reflected radiation, the theoretical reflectance of silicon and the reflectance measured by the empty sample holder respectively. Absorption coefficient (α) and absorbance (A) can be extracted from transmittance, reflectance and film thickness (d) measurements. If the intensity of radiation falling on samples is equal to 100 %, the sum of the percentage fractions of light reflected (R), transmitted (T), and absorbed (A) is equal to 100%, consequently the Absorbance is given by:

$$A (\%) = 100 - T - R \quad (15)$$

The optical absorption coefficient, α (cm^{-1}) is related to T, R and d as follows [15]:

$$\alpha = \frac{1}{d} \ln \frac{T_Q (1 - R_{spec.})}{T_{direct}} \quad (16)$$

where T_Q is the transmittance of the bare substrate.

The experimental measurement of the absorption coefficient allows to get informations about the optical bandgap of the material. Such important quantity can be derived by using the Tauc Model [16]. In this regard, for highly degenerate and direct band-gap oxides like TCO, under the assumptions of parabolic band edges for valence and conduction bands, and direct optical transitions of the electrons from valence band toward the conduction band (usually valid for values of α larger than $1 \times 10^4 \text{ cm}^{-1}$) it is commonplace to use the the Tauc relation:

$$\alpha = \frac{B}{\hbar\omega} (\hbar\omega - E_g)^{1/2} \quad (17)$$

where E_g is the optical bandgap of the material, B the Tauc coefficient and $\hbar\omega$ is the incident photon energy. To promote an electron from the valence band to conduction band, $\hbar\omega \geq E_g$ is required. Therefore, by plotting $(\alpha \hbar\omega)^2$ vs $\hbar\omega$ it is possible to extract the values of E_g and B as the energy-axis intercept and slope of the linear fit respectively.

3.6 Electrical measurement

A fundamental parameter to assess the electrical properties of a transparent electrode is the so-called sheet resistance, R_{sh} , representing a measure of the resistance of thin films, nominally uniform in thickness, along

the plane of the films. Commonly, Fig. 11, the 3-D conductor resistance, R , is given by:

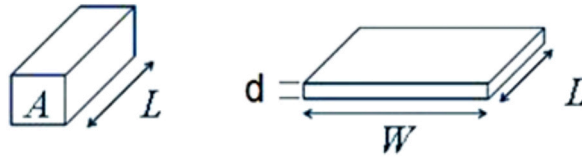


Figure 51: Geometry of the sample for defining 3-D conductor resistance (left) and sheet resistance (right).

$$R = \rho \frac{L}{A} = \rho \frac{L}{Wd} \quad (14)$$

where ρ is the resistivity (Ωcm), A is the cross-section area, and L is the length. The cross-section area can be split into the width W and the thickness d . Considering a thin film as a two-dimensional system and taking into account the previous figure, we can define the sheet resistance, R_{sh} , by:

$$R = \frac{\rho}{d} \frac{L}{W} = R_{sh} \frac{L}{W} \Rightarrow R_{sh} = \frac{\rho}{d} \quad (15)$$

A noteworthy thing is related to the shape of the sample: if sample has a square shape, then the sheet resistance corresponds to bulk resistance. This is the main reason because the unit of the sheet resistance is "ohms per square" (denoted with Ω/sq or Ω/\square); since a square thin film with sheet resistance 10 ohm/square has an bulk resistance of 10 ohm, regardless of the size of the square. The ohm per square is dimensionally equal to an ohm, but is exclusively used for the sheet resistance. Thus, by measuring the sheet resistance and if the sample thickness is known, one can deduce the resistivity ρ (or its inverse the conductivity σ (S/cm)); which is related to the electrical properties of the material by:

$$\rho = \frac{1}{\sigma} = \frac{1}{ne\mu} \quad (16)$$

where n , e and μ are electrons's density, charge and mobility respectively. A method for measuring sheet resistance is the four-point collinear probe technique, as shown in Fig. 12, used to avoid contact resistance that can often be of the same order of magnitude of the sheet resistance. Typically, if the probes are equally spaced, s , and $s \ll$ sample size, by sourcing a current flow, I , through the two outer probes and measuring the voltage, V , across the two inner probes, the sheet resistance is given by [1]:

$$R_{Sh} = \frac{\rho}{d} = K \frac{V}{I} \quad (17)$$

where $K = \pi/\ln 2 = 4.53$ is a geometric factor. In this thesis the electrical sheet resistance was measured using a four-point collinear probe method by employing a Keithley 4200-SCS (semiconductor characterization system) at room temperature.

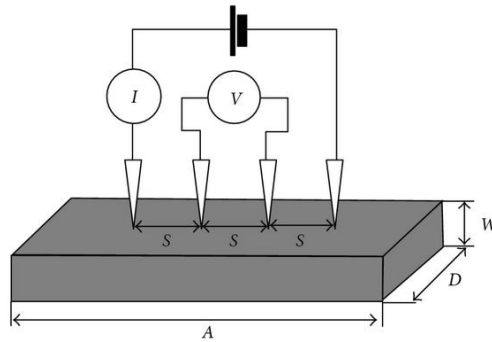


Figure 52: Schematic view of four-point probe configuration.

Another method is widely used in both sheet resistance and Hall measurements, which allows to measure electrons concentration and Hall

mobility: van der Pauw technique [17]. In a typical set-up, Fig. 13, four small contact are put at the corners of a square planar sample. To measure the sheet resistance, a current is driven through two adjacent contact (I_{1-2}), while the corresponding voltage drop is measured across the two contacts on the opposite side (V_{3-4}). This measurement is repeated twice for each set of contact pairs by switching polarity. Repeated for all four pairs of contacts, we can measure the resistance for each configuration by Ohm's law $V_{ij} = R_{ik,jl} I_{ik}$, where $R_{ik,jl}$ is the resistance of the sample for the current passed from l to k and the voltage drops between i and j .

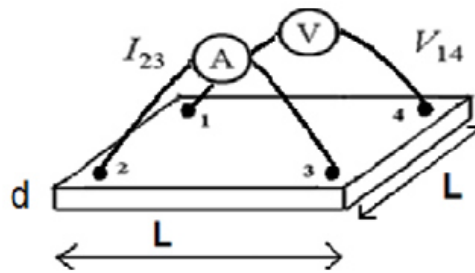


Figure 53: Schematic view of the four probe configuration in van der Pauw technique.

Known each resistance, we can solve the van der Pauw equation:

$$e^{-\frac{\pi R_A}{R_{sh}}} + e^{-\frac{\pi R_B}{R_{sh}}} = 1 \quad (18)$$

where R_{sh} is the sheet resistance of the thin film and R_A , R_B two characteristic resistances. In a squared shape sample with the contact put at each corner, can be shown that $R_A = R_B = (R_{21,34} + R_{12,43} + R_{43,12} + R_{34,21})/4$.

Therefore, solving the van der Pauw equation one can derive the sheet resistance:

$$R_{Sh} = \frac{R_A \pi}{2 \ln 2} \quad (19)$$

from which the resistivity is found via eq. 15, if the sample thickness (d) is known. Moreover, using this set-up one can determinate the carrier transport properties of a material by Hall effect. The Hall effect refers to the voltage that results from the deflection that is defined by the charged carriers by the Lorentz force that develops in the direction that is defined by the charge on the carrier, q, and the vector cross product of the drift velocity, \vec{v}_{drif} , of the carriers (direction set by the current flow) and the magnetic field, \vec{H} , [1].

$$\vec{F}_{Lorentz} = q (\vec{v}_{drif} \times \vec{H}) \quad (20)$$

If a current is driven trough two diagonally opposing contacts, I_{1-3} , by an electric field, \vec{E} , while a magnetic field is applied in the plane-normal direction, as shown in Fig. 14, it can be shown that the transverse Hall voltage, $V_{2-4}=V_H$, due to the collect of an excess of charge in the direction perpendicular to the current, can be written as:

$$V_H = \frac{IH_z}{qNd} \quad (21)$$

here I is the current, d is the sample thickness, q and N are the elementary charge and bulk density of the carriers respectively. The sign and the magnitude of the Hall voltage depends on the carrier type (mainly electrons in TCOs) and carrier density. Thus, by measuring the Hall Voltage, V_H , and from the known values of I, H_z , d and q, one can determine the carrier density N.

If the resistivity of the material is known by the sheet resistance (Eq. 15 and Eq. 19), then Hall mobility, μ_H , can be deduced using:

$$\mu_H = \frac{1}{qN\rho} \quad (22)$$

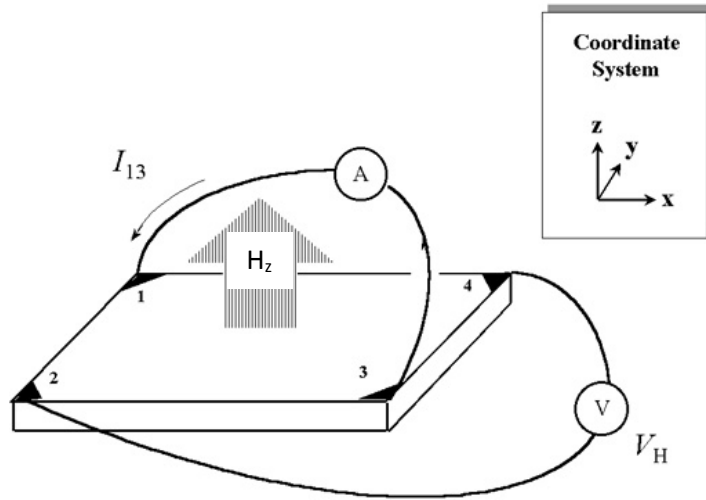


Figure 54: Schematic of the Hall Effect.

In this thesis the sheet resistance, carrier concentration and mobility in a wide range of temperature, 70-320 K, are performed by a BioRad HL5560 Hall effect system equipped with a system with both low and high temperature attachments, Fig. 15(a). Both low and high temperature measurement are fully automated, by a modular Windows-based software, with samples mounted on a cold finger of a closed cycle cryogenic refrigerator system. The temperature of the sample is varied by means of a heater attached to the cold finger, in order to achieve high temperature Fig. 15(b). This setup allows measurements on low ($0.5 \Omega/\text{sq}$) as well as high sheet resistance ($1 \times 10^5 \Omega/\text{sq}$) of the samples. In order to perform Hall measurements, the samples (1cm x 1cm) can be placed in a magnetic field

(325 mT) produced in the space between the two permanent magnets. In general, the electrical connections take place by conducting probes pressed directly to the film surface and a voltage of 20 mV is set among two probes.

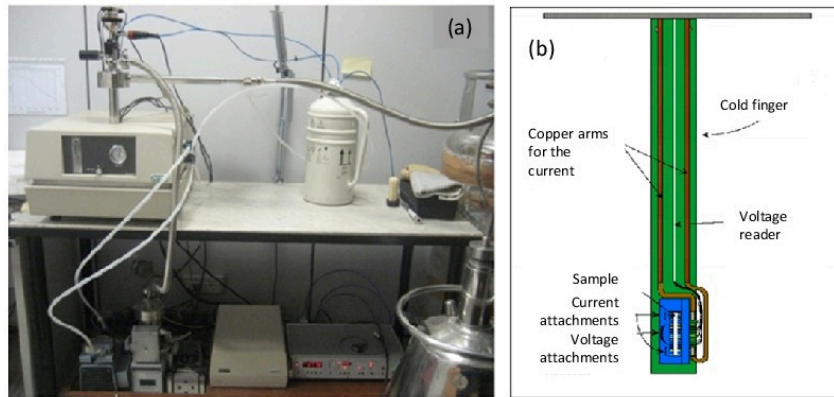


Figure 55: (a) BioRad HL5560 Hall effect system and (b) Schematic sketch of the cold finger.

References

- [1] D. S. Ginley, H. Hosono, D.C. Paine, *Handbook of transparent conductors*, Springer 2011.
- [2] T.L. Alford, L.C. Feldman, J.W. Mayer, *Fundamentals of Nanoscale Film Analysis*, Springer 2007
- [3] J. M. Mayer, L. Eriksson, J.A. Davies, *Ion implantation in semiconductor*, Academic Press, New York 1970, ch. 4
- [4] M. Mayer, *SIMNRA, a Simulation Program for the Analysis of NRA, RBS and ERDA*, Proceedings of the 15th International Conference on the Application of Accelerators in Research and Industry, J. L. Duggan and I.L. Morgan (eds.), American Institute of Physics Conference Proceedings 475, p. 541 (1999)
- [5] H.P. Klug, L.E. Alexander, *X-ray diffraction procedures for polycrystalline and amorphous materials 2nd edition*, John Wiley & Sons 1974.
- [6] D.K. Schroder, *Semiconductor material and device characterization*, John Wiley & Sons New York 1990.
- [7] Bragg, W.L., *Proceedings of the Cambridge Philosophical Society* **17**, 43 (1913).
- [8] Langgord J.I., Wilson A.J.C., *J. Appl. Crystallogr* **11**,102 (1978).
- [9] Min-Chul Jun and Jung-Hyuk Koh, *Nanoscale Res. Lett.* **7**, 294 (2012)
- [10] J. W. Mayer and E. Rimini, *Ion Beam Handbook for Material Analysis*, Academic Press, New York 1977
- [11] L. R. Doolittle, *Nucl. Inst. Meth. B* **9**, 344 (1985)
- [12] L. R. Doolittle, *Nucl. Inst. Meth. B* **15**, 227 (1986)
- [13] W. Zhou, Z. Lin Wang, *Scanning Microscopy for nanotechnology: techniques and applications*, Springer 2006

- [14] V.L. Mironov, *Fundamentals of Scanning Probe Microscopy*, Nizhniy Novgorod 2004
- [15] S. Mirabella, R. Agosta, G. Franzo, I. Crupi, M. Miritello, R. Lo Savio, M.A. Di Stefano, S. Di Marco, F. Simone, T. Terrasi, *J. Appl. Phys.* **106**, 103505 (2009)
- [16] J. Tauc, *In Amorphous and Liquid Semiconductor*, Plenum, New York 1974
- [17] L. J. Van der Pauw, *Philips Res Repts.* **13**, 1 (1958)

Curriculum Vitae

Stefano Boscarino was born on October 14th, 1981 in Siracusa (Italy). He attained his Master Degree in Physics with full marks from the University of Catania in March 2011. In November 2011 he was admitted to the three-year Ph.D. course in Science and Technology of Materials at the University of Catania. He is currently working under the supervision of Prof. Antonio Terrasi and Dr. Isodiana Crupi at the Physics and Astronomy Department of the University of Catania and at the CNR-IMM MATIS group of Catania. His research activity is focused on the fabrication and characterization of transparent conductive materials for optoelectronics and PV applications. The results of his research led him, as author and co-author, to the publication of several articles in international peer-reviewed scientific journals. He also presented them, giving both oral or poster contributions, at the following national and international conference: IEEE Nanotechnology Materials and Devices Conference 2014 (Acicastello, Italy), E-MRS spring meeting 2014, 2013 and 2012 (Lille and Strasbourg, Fr), XXI AIV Congress 2013 (Catania, Italy), 4th International Symposium on Transparent Conductive Materials 2012 (Heraklion, Crete, Gr). During his Ph.D course, he also participated to the 52th and 62nd *Course of the International School of Solid State Physics on "Materials for Renewable Energy"*, in 2012 and 2014 respectively.

List of Publications

This thesis is based on the following **Publications**:

- **S. Boscarino**, I. Crupi, G. Torrisi, A. Alberti, S. Mirabella, F. Ruffino, F. Simone, A. Terrasi, ***“Improvement of the structural, optical and electrical properties of AZO thin films upon ion beam irradiation”***, submitted for publication to *Solar Energy Materials and Solar Cells* (2014)
- **S. Boscarino**, I. Crupi, S. Mirabella, F. Simone, A. Terrasi, ***“TCO/Ag/TCO transparent electrodes for solar cells application”***, *Applied Physics A* **116**, 1287 (2014).
- I. Crupi, **S. Boscarino**, G. Torrisi, G. Scapellato, S. Mirabella, G. Piccitto, F. Simone, A. Terrasi, ***“Laser irradiation of ZnO:Al/Ag/ZnO:Al multilayers for electrical isolation in thin film photovoltaics”***, *Nanoscale Research Letters* **8**, 392 (2013)
- I. Crupi, **S. Boscarino**, V. Strano, S. Mirabella, F. Simone, A. Terrasi, ***“Optimization of AZO/Ag/AZO structures for ultra-thin high-performance transparent conductive electrodes”***, *Thin Solid Films* **520**, 4432 (2012)

AND MASTER DEGREE THESIS

- **S. Boscarino**, ***“Synthesis and characterization of AZO thin films.”***, (Academic year 2009-2010)